AXISYMMETRIC AIR JET IMPINGING ON A HEMISPHERICAL CONCAVE PLATE

BY

STEFAN JACHNA

A DISSERTATION
PRESENTED IN PARTIAL FULFILLMENT OF
THE REQUIREMENTS FOR THE DEGREE
OF
DOCTOR OF ENGINEERING SCIENCE
AT
NEW JERSEY INSTITUTE OF TECHNOLOGY

Newark, New Jersey

1978

APPROVAL OF DISSERTATION

AXISYMMETRIC AIR JET IMPINGING ON A HEMISPHERICAL CONCAVE PLATE

BY

STEFAN JACHNA

FOR

DEPARTMENT OF MECHANICAL ENGINEERING

NEW JERSEY INSTITUTE OF TECHNOLOGY

BY

FACULTY COMMITTEE

APPROVED: ______________________________ Chairman

____

____

____

____

NEWARK, NEW JERSEY
APRIL, 1978

TABLE OF CONTENTS

CHAPTER

ACKNOWLEDGEMENT

The author is grateful to Professor Peter Hrycak for his guidance, encouragement and a thorough supply of new publications in the field.

Thanks are due to The New Jersey Institute of Technology and its Department of Mechanical Engineering for providing the facilities of the Jet Research Laboratory.

The probe holder, the jet nozzles and some probes used in the present work came from Mr. D. T. Lee's experiments on the flat plate. Special probes and the hemispherical plate were originally furnished for National Aeronautics and Space Administration research project (20).

Sealmaster Bearings, a Division of Borg Warner Corp. donated the screw guide for this work.

Mr. Walter Schmiedeskamp of the Department of Mechanical Engineering Machine Shop mounted the test support structure, built additional pitot probes, loaned two indexing tables and helped with the auxiliary equipment.

Finally, thanks are due to the staff of the Deparment of Mechanical Engineering and Dr. Roman Andrushkiw from the Department of Mathematics who, in many ways, contributed to the successful completion of this work.

All this is acknowledge with sincere gratitude.

AXISYMMETRIC AIR JET IMPINGING ON A HEMISPHERICAL CONCAVE PLATE

Dissertation Abstract

This experimental study was conducted on an axisymmetric air jet impinging normally on a smooth, hemispherical, concave plate. The jet Reynolds numbers, based on bulk nozzle velocity and nozzle exit air properties, were between 14,000 and 75,000.

The impingement plate used in this work was a hemispherical surface with the radius of 94 mm.

Calibrated Pitot tubes and a micromanometer were used for pressure and velocity measurements. The Pitot tubes were mounted on precision positioning mechanisms permitting the accurate traversing of any direction in space. The test air flow rate was measured with calibrated rotometers.

The following results of this work are considered a contribution to the knowledge of the jets:

1. It was observed in the free jet zone that the minimum value of negative static pressure depends upon Reynolds number and that the location of the minimum is independent of Reynolds number. If the nozzle-to-plate distance is smaller than 20 nozzle diameters, this location is closer to nozzle exit in proportion to plate proximity. For any nozzle-to-plate distance larger than 20 nozzle diameters,

the location of minimum static pressure is constant and equal to eight nozzle diameters from the nozzle exit which is in essential agreement with other researchers.

2. Maximum velocity decay in the wall jet studied was determined to be less rapid than in the case of the flat plate wall jet.

3. A semi-empirical equation for maximum velocity decay in the wall jet was obtained. The development of this equation was based on integral momentum analysis.

4. Empirical equations for "reference boundary velocity" decay and maximum velocity decay in the wall jet were found. The results obtained from the equations are close to experimental results.

5. The developed hemispherical wall jet boundary layer was found to be much thinner than it is in the flat plate case. This fact may be significant in heat transfer.

LIST OF COMMON SYMBOLS

a	Coefficient
b	Width of jet
D	Nozzle diameter
P	Pressure
P , P_a	Ambient atmosphere pressure
P_c	Static pressure along the jet centerline
P_s	Wall surface pressure
P_{max}	Maximum pressure
S	Distance along the plate surface
Re_D	Reynolds number based on bulk velocity, nozzle diameter and air properties at nozzle exit
U	Velocity in the x and z direction
U_m	Maximum axial velocity of the jet
U_{oc}	Velocity at center of nozzle exit
V	Velocity in the "s" direction
V_m	Maximum velocity along the plate
V_{mo}	Maximum velocity along the plate at $\Theta = 10.9^\circ$
$\bar{V}_{m47^\circ} = \frac{V_m}{V_o}$	Reference maximum velocity at $\Theta = 47^\circ$
V_{RB}	Reference boundary velocity
x	Distance away from the nozzle
y	Radial distance from jet centerline
$y_{\frac{1}{2}}$	y-location where $U = \frac{1}{2} U_m$
z	Normal distance from the plate
$z_{\frac{1}{2}}$	z-location where $V = \frac{1}{2} V_m$

z_n	Normal distance between target plate and nozzle
δ	Boundary layer thickness, wall jet region
τ_w	Wall shear stress
θ	Position angle
γ	Specific weight
μ	Dynamic viscosity
ξ	$= (z - \tilde{\delta}) / b$
ρ	Density

Other symbols are as defined in the text.

Subscript "o" indicates conditions at the origin.

Barred symbols indicate dimensionless quantities.

Prime sign indicates a derivative.

CHAPTER 1

INTRODUCTION

A jet is a forceful stream of fluid emitted into the environment. Jets have wide application:

- An octopus escaping danger, a ship propelling herself at sea, an aeroplane in the air - use jet to gain velocity.
- A boiler burner uses a jet to deliver fuel.
- A jet impinging on Pelton wheel converts kinetic energy to mechanical work.
- A jet of air or steam issued through a siren sounds an alarm.
- A jet of air is used in metallurgy for surface hardening.
- Granulated material fluidization and conveying utilize jets.
- The rocket jet put man on the moon.

The application of the jet is old and common. It was first applied by trial and error.

The era of jet investigation started after Prandtl had published his mixing length theory in 1925. Tollmien used this theory the next year and this became the first theoretical research of axially symmetric jets. Further theoretical contribution to the knowledge of the jet came in 1932 with Taylor's publication of his theory of free turbulence. Ten years later Prandtl published his new theory based on viscous friction. Goertler (13)*, applying this theory obtained a solution of a free turbulent circular jet. Goertler also used this theory in his work on the problem of the mixing zone at the boundary

---

*Numbers in parentheses indicate references in bibliography of parallel jets, obtaining results which are in good agreement with the measurements by Reichardt (34).

Many other theoreticians and researchers continued the study of jet in various flow and boundary conditions. Among them were:

Schlichting (40) developed theory on two dimensional wake behind a body, applicable to jets.

Glauert (11) was one of the first researchers to work on wall jet along a flat plate.

Barat (4), then Miller and Comings (28) demonstrated the existence of negative static pressure in the jet.

Gooderum, Wood and Brevoort (12) investigated free boundary of a free supersonic jet.

Bakke (3) experimented with wall jets and contributed to the testing technique.

Poreh and Cermak (31) investigated impinging jets and added new aspects to the subject.

Hrycak et al. (19) studied mass and heat transfer in impinging jets.

Bradshaw and Gee (7) in their study took into account a stream external to the jet.

Albertson et al. (2) studied diffusion of jets.

More recently Maxwell (27) presented a study of momentum flux in developing region of jets.

Russell and Hatton (37) used both Pitot tube and hot wire measurements to study a jet impinging on a flat plate and found the first one better.

Van Der Hegge Zijnen (48) presented elaborate test data of jet velocity distribution and obtained very consistent results.

Schnurr, Williamson and Tatom (42) studied jets impinging on curved deflector. Data were applicable to transport aircraft.

Reid and Katz (35) investigated free and impinging jets with and without auxiliary flows.

Beltaos and Rajaratnam (6) presented compatible velocity distribution in their studies of a slit jet impinging on a flat plate.

Narain (29) gave an account of a swirling turbulent plume.

Krishnan and Glicksman (24) analyzed jets impinging on smooth plates.

Y. Tsuei (47) and T. S. Kim (23) in their respective dissertations analyzed jets impinging on smooth plates.

Hrycak, Nagarajan and Lee (20) studied mass and heat transfer in the hemispherical geometry.

The list of investigators, who contributed to knowledge of jets is long and growing. The acknowledgement of their accomplishments is not the intent here. Only some were cited and some will be referred to in the following chapters, as the correlation of topics develops.

For comparison purposes, an effort was made in this work to closely relate common tests to those in (20) and (25), while running reproducible tests.

Instrument set-up in spherical coordinates and securing a steady supply of test air were difficult and time consuming. It took three quarters to one hour from start-up to reach the desired steady operating conditions. The instrument calibration was very sensitive to the probe positioning. In order to obtain reproducible test data the experimental arrangement was modified three times until the final version met the requirements.

The experimental error, as evaluated in Appendix C, was about 2% of the measured velocity.

CHAPTER 2

SUBJECT OF INVESTIGATION

This investigation was of an experimental type. The subject was a turbulent, subsonic, axisymmetric free jet of air impinging normally on a smooth, hemispherical, concave plate.

Depending upon flow characteristics, the impinging jet can be divided into four regions, or zones, as shown in Figure 7:

I. Potential Core
II. Free Jet
III. Deflection
IV. Wall Jet

The primary interest of this investigation was directed to:

a) velocity profile and pressure distribution of the free jet as affected by the presence of the impingement plate.
b) velocity profile, pressure distribution and boundary layer thickness in the wall jet.

The nozzle exit local Mach number range of jets investigated was 0.1 to 0.54. The Reynolds number range of jets was 14,000 to 75,000 based on the bulk nozzle velocity and nozzle exit air properties.

Local Reynolds number based on the hemispherical test plate diameter was 7,300 and higher. Since laminar flow region exists for Re $\leq$ 1,000 (19), transition region for 1,000 $\leq$ Re $\leq$ 4,000 and fully turbulent flow above 4,000, the range of investigation was entirely in the turbulent region.

The flow may be considered incompressible (39) up to $M = 0.3$. The majority of the present tests was run below this value. The highest local Mach number in the wall jet tested was $M = 0.28$, with incurred error less than 2%, see Appendix C.

Momentum equation was applied to analyze maximum velocity decay in the wall jet and the results were compared with the tests.

CHAPTER 3

DESCRIPTION OF APPARATUS

3.1 Air Supply

The experimental part of this investigation was done in the Mechanical Engineering Laboratory of New Jersey Institute of Technology. The air supply system consisted of an electric motor driven, two stage, reciprocating compressor with jacket cooling, interstage cooling, oil separator and after-cooler with a moisture trap. The compressor drew in ambient air. The compressed air was directed to an air receiver of about 4 cu. ft. volume. Excess air was blown off from the air receiver while the main stream was supplied to the test room. After passing a regulating valve, the air entered either a "large" or "small" rotometer as directed by isolating valves. Both rotometers had scale range of 0-60 cm. The "large" or high flow unit had mass flow range of 0.004 to 0.046 lb/sec. ± 1% rate of instantaneous reading, the "small" or low flow unit had the range of 0.001 to 0.00725 lb/sec. ± 1% rate. Calibration was done by National Aeronautics and Space Administration. Calibration charts are shown on Figures 1b and 1c. The air flow was regulated by the valves downstream of the rotometers. The main purpose of measuring the air flow with the rotometers was to establish the Reynolds number.

Two calibrated Bourdon type pressure gauges were installed upstream of rotometers: one was a rough reading gauge of 0-200 ± 1 psig. The other was a fine reading, calibrated gauge of

0-30 psig ± 0.15 psig range. After passing the rotometers the air entered a 7.5 ft. long pipe in which a copper-constantan thermocouple was installed in a well to measure the test air temperature. The thermocouple was located about one foot upstream of the final elbow. A flexible connection was applied between the thermocouple and the final elbow to prevent plenum vibration.

Downstream of the flexible connection an elbow turned the air down to a plenum terminated with a tap to accept test nozzle, Figure 1. A screen type flow straightener was used in the plenum. The air supply piping was $1\frac{1}{2}$" diameter up to the rotometers. The pipe between the rotometers and a plenum was $1\frac{1}{4}$". The plenum was $2\frac{1}{2}$" diameter, 35" long. The piping was suspended from the room ceiling. It was held vertical with the aid of three anchoring wire lines with turnbuckles.

Consistent with rotometer calibrations, the test air was supplied at 25 psig measured at the flow meters. To maintain this constant pressure level at different flow requirements, a pressure regulating valve was mounted just upstream of the flow meters. The mass flow rate was corrected for temperature deviation from the calibration value.

The test room ambient air temperature was measured with a mercury thermometer while barometric pressure readings were taken from a laboratory aneroid type barometer at the compressor. The ambient temperature difference between test and compressor rooms was not greater than 1°F. Compressed air excess moisture was removed in the aftercooler. Gas velocity measured is a function of its specific gravity which in turn depends upon its humidity. This investigation was concerned with velocity and pressure ratios. In such a case specific gravity appears in the numerator and denominator. Relative humity effects were therefore omitted in the calculations.

Relative humidity has to be taken into account for "absolute" velocity measurements. The most practical way in this case was to measure the temperature of moist air leaving the aftercooler. Assuming that it is nearly saturated and then heated to the plenum temperature at constant humidity ratio, the specific volume can be determined from the psychrometric chart.

3.2 Manometers

Different manometers were used depending upon the pressure measured: a U-tube filled with mercury, a U-tube filled with water and for the smallest pressures a micro-manometer filled with a non-hygroscopic manometric liquid having specific gravity of 0.7970 at 75°F. The specific gravity of the manometric liquid was stable within the range of measurements. The manometer was capable of measuring the pressures smaller that 0.001 of an inch of water. The scale was calibrated in inches of water.

3.3 Impinging Plate

The impinging plate shown on Figure 2 had a hemispherical shape made of one piece 1.1 mm thick brass sheet. Such a sheet is flexible if flat, but when given a three dimensional shape, it is rigid like a basin or bowl. The plate had a surface finish of a cold rolled metal. Such a finish is considered smooth on Moody diagram. The plate had a 93.7 mm inside radius. Twenty-nine plexiglass "corks" were bonded from outside on plate meridionals. A 0.4 mm diameter hole was drilled through the cork and plate in each cork. The hole ridges on the jet side were made free of drilling burrs. The central hole was located at the stagnation point. The "cork" holes served as taps for measuring pressure distribution. They were also used as "stations", Figures 1 and 2. The plate was held by a support having three adjustable legs. The leg adjustment was used for plate leveling, Figure 2. All taps were plugged with masking tape, from the outside, to prevent air leaks, except when measurements were being taken. The plate used in the test was approved by N.A.S.A.

3.4 Plate Mounting

The impinging plate and the probe holder were mounted on two identical indexing tables bolted to a support table, Figure 1a. The support table was braced for rigidity. The indexing tables had linear movements along X and Y axes and rotation about Z axis. All movements were equipped with vernier scales. The support table was fastened to a vertical guide which could travel 50 cm on the vertical axis for setting nozzle-to-plate distance. The vertical guide was bolted to a structure resembling a drill press column.

The column base was anchored to the floor, the column top was clamped on the vertical axis to a sturdy wooden brace.

3.5 Probe Mounting

A traversing carriage shown on Figures 3a and 3b was used to mount the pressure measuring probes. It was fastened to an indexing table identical to that of the test plate. The two indexing tables were mounted next to each other on the support table, Figure 1a. The traversing carriage had a vertical beam 2 ft. tall equipped with a vernier. It had a stage mounted on a journal. The stage could rotate about the journal and also travel on X and Z axes. The combination of movements of the two indexing tables and the movements of the traversing carriage made it easy to adjust the probe to any required position. All movements had vernier scales. The whole probe positioning mechanism could be precisely set at any point and any angle in space. When setting and reading instruments, a two-power magnifying glass was used for reliable resolution.

3.6 Pressure Probes

Pitot type probes were used for measuring static and total pressures. The design of these probes was recommended by NASA and used by Lee (25). The probes are shown in Figure 4. The static pressure probe was made of 0.8 mm (1/32 inch) diameter stainless steel tubing. It had four 0.4 mm (1/64 inch) drill holes for sensing static pressure. The total pressure probe was made of 0.4 mm diameter stainless steel tubing.

Modified probes were used to reach the bottom of the hemispherical plate for measuring the boundary layer thickness. The probes are shown in Figure 6. The total pressure probe was made of

3.18 mm (1/8 inch) diameter stainless steel tubing with the tip of 0.8 mm diameter. The probe was bent to fit the inside of the hemisphere, as illustrated. The static pressure probe had a similar shape to the above, except for the tip which had four pressure sensing holes of 0.4 mm diameter.

3.7 Jet Nozzles

Two nozzles were used in this investigation. They were brass, made of the same bar stock. Their outside dimensions were identical, except for outlet diameters which were 9.5 mm (3/8 inch) and 6.35 mm (1/4 inch). The nozzle design is shown in Figure 5.

CHAPTER 4

EXPERIMENTAL PROCEDURE

The test apparatus set up for taking measurements was done in the following way:

The test plate was mounted on one indexing table and lined up vertically with the aid of a level gauge. The traversing carriage was mounted on the other indexing table and locked in vertical position with the aid of a stiffening bracket. The vertical axis of the jet was set with the aid of turnbuckles on plenum anchoring lines, Figures 1 and 1a.

The coaxiality of the vertical guide and the jet axis were checked prior to system operation in the following manner.

A. The plate was brought close to the jet nozzle.

B. The stagnation point was found, as described further below.

C. The plate was moved away from the nozzle by lowering the guide to minimum elevation.

D. Location of the stagnation point was rechecked at the low guide elevation.

It was suggested by Snedeker (43) to use a dark grease drop for visual location of the stagnation point. The grease is put on the surface on the expected location of the stagnation point. The impinging jet forces the grease to "creep" away from the stagnation point, except at the stagnation point, where it remains motionless. This method is very accurate and easy, but messy. It cloggs up the pressure taps in the plate, and for that reason was not used in this experiment. Since there was a drill hole located at station "1", at the bottom center of the hemisphere, it was much neater and equally accurate to locate the stagnation point by observing maximum pressure reading under the impinging jet. A pressure probe connected to a manometer showed the maximum reading easily located by X and Y traversing of the indexing table. Rotation of the indexing table with respect to the Z axis was the final check, at which the maximum pressure reading remained constant at the stagnation point.

The following preparations were made prior to testing:

I. A desired size of issuing nozzle was installed in the plenum exit with a neoprene "o" ring to prevent air leaks.

II. The impingement plate was positioned at the required nozzle-to-plate distance.

III. The flow rate and the rotometer setting were predetermined with the aid of rotometer calibration plot for the required Reynolds number.

IV. The compressor was started. The flow and pressure were then adjusted as test conditions required.

V. The coaxiality of jet and the impingement plate was checked and eventually corrected.

VI. Some adjustments were necessary to reach equilibrium conditions at the desired flow. The adjustments were to be made on the throttling globe valve, the blow-off valve, the pressure regulating valve and also on intercooler and aftercooler water flow.

When the above preparations were completed, the system was ready for measurements.

To take the measurements either the probes shown on Figures 4 or 6 were used, depending upon which jet zone was investigated.

The instrument setting in the free jet zone, marked II on Figure 7, was simple. It required placing the probe in the jet on the proper coordinate.

In the wall jet zone, marked IV on Figure 7, the probe positioning was time consuming. For any of the 15 stations in the rows A and B on the hemisphere the directional angle of the probe holder had to be predetermined and the traversing carriage stage aligned at this angle. Subsequently the probe was made tangent to the hemispherical plate surface and "zero" reading position set taking into account the probe diameter. In this setup the probe was being moved perpendicular to the surface of the plate at a given station.

CHAPTER 5

POTENTIAL CORE

The potential core is zone I as shown on Figure 7. It extends conically down and is characterized by maintaining nozzle exit velocity. The length of the core depends upon the mass flux, i.e. Reynolds number, at $Re_D \leqslant 10{,}000$. For Re_D between 10,000 and 20,000 this dependence is weak, according to (25). Above that, the length of the potential core becomes independent of Re_D, (1).

The length of the potential core is determined by plotting on a log-log graph paper the centerline jet velocity U_c/U_{oc} vs. the distance from the nozzle exit, x/D. The intersection of the tangent to the curve and $U_c/U_{oc} = 1$ is defined as the nominal core length.

The range of potential core lengths, expressed dimensionlessly as given in (19) were:

$x/D = 4.8$ at $Re_D = 3500$ for $D = 9.52$ mm
$x/D = 5.3$ at $Re_D = 4000$ for $D = 6.35$ mm
$x/D = 5.5$ at $Re_D = 5500$ for $D = 3.17$ mm

Max $x/D = 6.8$ was at $Re_D = 10{,}000$ for the above nozzle diameters.

The Reynolds numbers in the present study were all above 13,000. To establish the jet centerline velocity decay and to find the potential core length, a series of tests were run. The results are summarized on the plots, Figures 8 through 15.

Plotting U_c/U_{oc} versus x/D on log-log paper as indicated above gave the potential core lengths.

The plots are clearer for larger distances of the plate from the nozzle, i.e. for large z_n/D values.

Figure 8 presents three curves for Re_D = 15,4000; 27,000 and 46,100 at $z_n/D = 20$ and D = 6.35 mm.

Figure 9 presents three curves for Reynolds numbers comparable to the above numbers and the same nozzle diameter with $z_n/D = 13$.

From Figures 8 and 9, it appears that as Re_D increases independently of z_n/D, the experimental results approach equation 6.14.

All six of the above mentioned curves produce the potential core length of about x/D = 6.0.

Figures 8, 9, 10, and 11 were developed from data run for the same nozzle diameter, D = 6.35 mm. Figure 10 presents the curves for similar Reynolds numbers but for $z_n/D = 9$. Figure 11 depicts the same, adding one more Reynolds number = 72,700 for $z_n/D = 7$. These two plots do not provide useful information concerning potential core length. This is due to the proximity of the nozzle exit to the impinging plate. There was no space to take measurements beyond the range shown due to the physical size of the probes.

For another reason these two plots reveal this very important result: At only two nozzle diameters from the plate the centerline velocity is still about 97% of the exit velocity. The proximity of the plate resulted in an unexpectedly small velocity retarding effect.

Figures 12, 13, 14 and 15 have the same purpose as Figures 8, 9, 10 and 11, but they show the results for nozzle diameter = 9.52 mm. Figure 12 presents the centerline velocity decay for Re_D = 15,8000; 28,800 and 57,800 at $z_n/D = 20$. Here the experimental results approach equation 6.14 starting with higher Re_D. Figure 13 shows similar Reynolds numbers as Figure 12 but at $z_n/D = 13$. From all six curves on the above two plots the potential core length obtained is again $x/D = 6$. Figure 14 shows the centerline velocity decay for Re_D = 15,800; 30,800 and 56,500 at $z_n/D = 9$. Figure 15 exhibits the results for Re_D = 16,100; 29,700; 53,500 and 69,000 at $z_n/D = 7$. In this case the two last figures also provide no information to determine the potential core length due to the physical size limitations, but they indicate that the nozzle exit velocity is little affected by plate presence down to the distance of 2D.

The following important facts were established in the study of the potential core:

1. The potential core length was found to be independent of the nozzle diameter for nozzle diameters of 6.35 and 9.5 mm and Reynolds number between 10,000 and 70,000.

2. The potential core length for the condition in the study was essentially constant and equal to about 6D. A space limitation between the nozzle and the plate prevented taking longer range

measurements. A mean value of 6.0 is then accepted.

The core length discussed is the "nominal" length, shown on Figure 8 as dimension C. It is determined by intersection of the line representing the centerline velocity decay in the jet with the horizontal line representing the dimensionless centerline velocity $U_c/U_{oc} = 1$. The real or "true" length shown on Figure 8 as the dimension L^* is the distance from the nozzle exit to the furthest point on the jet centerline where the velocity is still equal to U_{oc}.

3. Even at distances of as close as two nozzle diameters from the impinging plate, the exit velocity is retarded no more than 3%.

CHAPTER 6

FREE JET

6.1 Centerline Velocity Decay and Jet Spread

The free jet, zone II on Fig. 7, in this experiment was turbulent, axisymmetric and incompressible. It was studied analytically and experimentally and at present the analytical results are fairly well proven by measurements.

In the impinging plate experiments the free jet is 4/5 of the distance from the nozzle exit to the impinging plate, z_n. This zone of the jet is not affected by the presence of the plate. This fact was established by Poreh and Cermak (31), Tani and Komatsu (45), Lee (25) and was confirmed by this study. For reference purposes it is useful to present some historical background of the free jet analysis.

The first theoretical study of the circular turbulent jet is due to Tollmien, who based his work on Prandtl's mixing length theory, i.e.

$$\tau = \rho l^2 \left| \frac{\partial u}{\partial y} \right| \frac{\partial u}{\partial y} \qquad (6.1)$$

where τ is the shear stress

u is the velocity in axial direction

y is the radial direction

l is a length to be derived from experimental measurements.

$\left| \frac{\partial u}{\partial y} \right|$ is a statistical mean of the slope $\frac{\partial u}{\partial y}$

Since the local mean can be written as

$$\sqrt{\left(\frac{\partial u}{\partial y}\right)^2 + l_1\left(\frac{\partial^2 u}{\partial y^2}\right)^2}$$

When put into 6.1 becomes:

$$\tau = \rho\, l_1^2 \frac{\partial u}{\partial y} \sqrt{\left(\frac{\partial u}{\partial y}\right)^2 + l_1\left(\frac{\partial^2 u}{\partial y^2}\right)^2} \qquad (6.2)$$

Where

l_1 is a new length to be determined for the particular experiment.

Furthermore introducing Prandtl's "new hypothesis" (41) with the virtual kinematic viscosity

$$\tau = \rho\, \varepsilon \frac{\partial u}{\partial y} = k_1\, b\, (U_{max} - U_{min}) \frac{\partial u}{\partial y} \qquad (6.3)$$

Where

k_1 is an experimental coefficient, b is the width of mixing zone

It is assumed that ε is constant over the width of jet and independent of the distance from the virtual origin x, as first discussed by Reichardt (34).

Using Prandtl's assumption that the mixing length l is proportional to the width of the jet, b

$$\frac{l}{b} = \text{const} \qquad (6.4)$$

Schlichting estimated the increase in width and decrease in velocity as follows:

From experimental investigation it could be stated that the increase of mixing zone width time is proportional to the transfer velocity, v'

$$u \frac{\partial b}{\partial x} + v \frac{\partial b}{\partial y} \sim v'$$

Comparing this to the expression obtained by Prandtl for mixing length theory

$$v' \sim l \frac{\partial u}{\partial y}$$

Schlichting obtained

$$u \frac{\partial b}{\partial x} + v \frac{\partial b}{\partial y} \sim l \frac{\partial u}{\partial y}$$

Taking further approximation that the mean value of $\frac{\partial u}{\partial y}$ is to be taken for the half width of the jet and is proportional to u_{max}/b, therefore

$$u \frac{\partial b}{\partial x} + v \frac{\partial b}{\partial y} \sim l \frac{u_{max}}{b}$$

or

$$u \frac{\partial b}{\partial x} + v \frac{\partial b}{\partial y} = \text{const} \ \frac{l}{b} u_{max} \qquad (6.5)$$

Taking for the jet boundary

$$u \frac{\partial b}{\partial x} + v \frac{\partial b}{\partial y} \sim u_{max} \frac{db}{dx} \qquad (6.6)$$

Comparing 6.5 and 6.6

$$\frac{db}{dx} = \text{const} \ \frac{l}{b} = C_1 \qquad (6.7)$$

And after integration

$$\frac{b}{x} = C_2 \qquad (6.8)$$

The last equation is valid for circular and two dimensional jets. To relate u_{max} and x, the momentum equation is used with the assumption that the pressure is constant in the jet:

$$J = \rho \int_A u^2 \, dA = 2\pi \rho \int_0^\infty u^2 \, y \, dy =$$

$$= \text{const} \; \rho \; u_m^2 b^2 = \text{constant} \qquad (6.9)$$

from which

$$u_m = \text{const} \; \frac{1}{b} \sqrt{\frac{J}{\rho}} \qquad (6.10)$$

Substituting equation 6.8

$$u_m = \text{const} \; \frac{1}{x} \sqrt{\frac{J}{\rho}} \qquad (6.11)$$

Since both J and ρ are constant,

$$u_m = \frac{\text{const}}{x} \qquad (6.12)$$

According to equ. 6.12 the jet centerline velocity is inversely proportional to the distance from the jet origin. For plotting purposes it is more convenient to put 6.12 into dimensionless form

$$\frac{u_m}{u_{oc}} = \frac{C}{x/D} \qquad (6.13)$$

This equation holds for fully developed flow in the free jet zone. The coefficient in equation 6.13 is the dimensionless potential core length as defined by Abramovich (1) who studied the results of experiments previously conducted by German researchers. Lee (25), running the tests with the flat plate, obtained the value of $C = x_c/D$ up to 6.8. Other researchers obtained C in the range of 5.2 to 7.7.

For Reynolds numbers between 14,000 and 75,000, according to this study, the value of C was a constant and equal to about 6.0, as indicated in the previous chapter. Therefore for the hemispherical concave plate the last equation becomes

$$\frac{u_m}{u_{oc}} = \frac{6}{x/D} \qquad (6.14)$$

The line representing this equation is drawn on Figs. 8, 9, 12 and 13. It makes sense for $x/D \geq 6$, since u_m/u_{oc} is never greater than one. As seen in the figures, relation 6.14 gives faster velocity decay. Equation 6.14 could be viewed as a limiting line for these experiments. It could be used for the prediction of lower limit centerline velocity. The largest discrepancy appeared on Fig. 8, where $x/D = 17$, the actual velocity as measured is $\frac{u_m}{u_{oc}} = 0.4$ while equation 6.14 gives the value of $\frac{u_m}{u_{oc}} = 0.35$.

The actual velocity is larger than that predicted theoretically.

According to Reichardt (34) the half width of the developed jet is given by:

$$b_{\frac{1}{2}} = 0.0848\ x \qquad (6.15)$$

Making it dimensionless

$$\frac{b_{\frac{1}{2}}}{D} = 0.0848\,\frac{x}{D} \tag{6.16}$$

This relation is shown on Figure 17. It does not provide accurate information for the jet impinging on a hemispherical concave plate. Inspection of the two plots presented on Figure 17 shows that the discrepancy between equation 6.16 and the measurement are smaller for smaller nozzle diameter (6.35 mm) and larger for larger nozzle (9.52 mm). According to this investigation, the following equation represents experimental results better:

$$\frac{b_{\frac{1}{2}}}{D} = 0.092\,\frac{x}{D} \tag{6.16a}$$

Apparently the half width growth depends upon nozzle construction. Figure 5 shows that the nozzles used in this investigation had the "approach diameter", $D_1 > 2D$.

Many researchers use $D_1 = D$, i.e. the nozzle looks like a piece of pipe. A constant half width growth cannot be expected to be the same for all nozzles, regardless of their construction.

6.2 Static Pressure Variation Along Jet Centerline

In all previous theoretical considerations of the free, turbulent, incompressible jet it was always assumed that the static pressure is constant and equal to ambient. Barat (4) and later Miller and Comings (28) proved existence of negative static pressure in the air jet. Lee (25) measured it also. There were many tests run in the present series to investigate the subject and the test results confirm existence of the negative static pressure in the jet stream.

Since Pitot tubes were considered to give more conclusive results than hot wire method for velocity measurements, they were used exclusively in these tests. Static pressure measurements were done with Pitot tube shown in Figure 4. According to Prandtl (33), the Pitot tube pressure reading depends upon probe hole size and should be increased by a small fraction of the flow velocity head to obtain a true value. No such correction was applied in this investigation.

Numerous tests were run in this investigation to establish static pressure distribution in the free jet zone. The results are presented in Figures 18 through 26 showing the pressure distribution along the jet centerline.

Figures 27a through 27f show the plots of static pressure across the jet. The tests demonstrate that the static pressure is negative in the unrestricted regions.

Figure 18a symbolizes a typical trend of curves, except at x/D close to zero. At low x/D, the nozzle exit dimensionless pressure is close to ambient, downstream it reaches minimum (inverted scale is shown on the plots) and then it rises again. Figure 18b compares the test results obtained for a free jet with similar test by Barat (4) and Lee (25). The curves are compatible. Static pressure remains negative, asymptotically approaching zero, consistent with the experimental results (16). Extensive tests which were run for (16) reveal another important fact: the minimum static pressure on the jet centerline always falls at $x/D = 8$. The location of this minimum was independent of Re_D and appeared at $x/D = 8$ for the different nozzle diameters used in the experiments. The results were obtained for eight different Reynolds numbers ranging from 10,000 to 54,000 and at three different nozzle diameters, $D = 3.2$, 6.35 and 9.5 mm.

The results of the present study are in agreement with the above mentioned results. For any nozzle-to-plate distance equal to or larger than 20 D, the location of minimum static pressure is a constant = 8 D, at any Reynolds number in the range tested. When the distance z_n/D becomes smaller, the minimum (inverted on plot) is closer to the issuing nozzle. As expected, for larger Reynolds number the static pressure contour is more pronounced, but the location of the minimum is the same for the same z_n/D, at any Re.

All the static pressure measurements along the jet centerline were consistent, except for the points in the vicinity of the nozzle exit. In that region, for 6.35 mm diameter nozzle, the pressure curves were inverted and the same trend was observed for 9.5 mm nozzle at larger Re_D. In this region, for 9.5 mm nozzle at at smaller Re_D, the curves were not inverted and a positive pressure was measured.

A possible explanation of this phenomenon can be that, for the smaller nozzle at all Re_D, and for the larger nozzle at larger Re_D, the issuing jet was too much disturbed by the presence of the pressure probe inside the issuing nozzle. When measuring these points, the static pressure probe tip had to be inserted into the nozzle exit, in order to have static pressure sensing holes close to it. The ratio of the pressure probe diameter to the smaller nozzle diameter was 1/8.

6.3 Static Pressure Distribution Across the Jet

Identical nozzle diameters were used to study the static pressure distribution across the jet in this work. The plate-to-nozzle distance was set at $z_n/D = 20$, Reynolds numbers run were 14,000; 15,500; 27,600; 29,700; 48,000 and 59,300. There were three measurement cross sections, at $x/D = 4$, 8 and 12. The test results are shown on Figures 27a through 27f. A pattern for the curves is established. It looks like an inverted mountain chain lined up along the jet centerline. The curves have minimum (reversed on plots) at the centerline for $x/D = 8$ and 12, then approach ambient pressure further away. Consistent with the pressure distribution along the centerline, the minima fall with increasing Reynolds numbers, but for each Re_D the extremum occurs at $x/D = 8$.

The plot for $x/D = 4$ behaving in the same way further away from the centerline, has a dip at the centerline itself. From the previous consideration this is the region of potential core. As mentioned in the preceding paragraph this region may not produce stable pressure readings, and the presence of the pressure probe disturbs the flow too much in the proximity of the nozzle exit.

The curves obtained in this work for 6.35 and 9.5 mm nozzles resembles the curves obtained by M. Barat (4), who used 150 mm nozzle diameter. Since the nozzle size and construction were different, a complete similarity of curves could not be expected. The nozzle used by Barat was a piece of round pipe, while the nozzles used in this work had an exit contraction, as shown in Figure 5.

6.4 Velocity Distribution in the Free Jet

Velocity profile equations for the free jet were developed by Schlichting from the Navier-Stokes and continuity differential equations.

In solving them, some simplifying assumptions were used and semiempirical coefficients introduced.

One of these assumptions was that the static pressure is constant and equal to ambient pressure, which is contrary to the data presented in the preceding two paragraphs.

Another important assumption was that a jet can be considered to have a point source and have geometrical similarity of velocity profiles. The best known velocity equations are those due to Schlichting's theory for the turbulent jet, based on virtual kinematic viscosity which is constant here.

$$u = \frac{3}{8\pi} \frac{k}{\varepsilon_o x} \frac{1}{(1 + \frac{1}{4}\eta^2)^2} \tag{6.17}$$

$$v = \frac{1}{4} \sqrt{\frac{3}{\pi}} \frac{\sqrt{k}}{x} \frac{\eta - \frac{1}{4}\eta^2}{(1 + \frac{1}{4}\eta^2)^2} \tag{6.18}$$

Where

$\eta = \frac{1}{4} \sqrt{\frac{3}{\pi}} \frac{\sqrt{k}}{\varepsilon_o} \frac{y}{x}$ = similarity variable

$k = 2\pi \int_0^\infty u^2 \, y \, dy$ = kinematic momentum

ε_o = virtual kinematic viscosity

There are also solutions due to Tollmien, not given here. The two equations differ in such a way that according to Reichardt's (34) measurements, equation 6.17 is better at higher velocity, i.e. closer to the jet centerline while Tollmien's equation is better beyond the jets half width.

The test results are presented in Figures 16a through 16f. The plots are shown in dimensionless velocity vs. dimensionless width. For comparison the Schlichting and Tollmien curves are drawn and test points are indicated. To have the most coverage the longest nozzle-to-plate distance, $z_n/D = 20$, was selected for plotting. Six plots were made, one for each test station distance from the exit nozzle: x/D = 6, 8, 10, 12, 14 and 16. Each plot represents two nozzle diameters, D = 6.35 mm and D = 9.5 mm and there are three different Reynolds number tests ranging from 14,000 to 60,000 for each nozzle diameter.

The present test results indicate that in this experiment the velocity profile is closer to the Schlichting curve, as defined by equation 6.17, rather than to the Tollmien curve and Reichardt test points. Up to $y/y_{\frac{1}{2}} = 1$ the test points obtained in this experiment are located above the Schlichting curve, then they follow this curve to about $y/y_{\frac{1}{2}} = 1.4$. For still larger $y/y_{\frac{1}{2}}$, the test results have different tendencies: the test stations closer to the nozzle are nearer to the Tollmien curve. With increased distance, e.g. $x/D = 10$, the test points obtained in these experiments fall close and above the the Schlichting curve. It was observed that at these points the readings were unsteady and the points were scattered. It is attributed to small nozzle-to-plate distance case, when the fully developed flow was not yet established.

The velocity profile reveals no dependence upon nozzle diameter and Reynolds number.

This behavior is consistent and well established (41, 46, 34, 48, 25).

Scatter in velocity measurements in the free jet was mainly due to fluctuations caused by vortices washed away from the target plate boundary layer and entering the free jet region.

CHAPTER 7

DEFLECTION ZONE

In this investigation the jet axis was normal to the impingement plate. The common point of the jet axis and the impingement plate locates the stagnation point. Using a cylindrical coordinate system with the origin at the stagnation point, Frössling found an exact solution of the Navier-Stokes equations. It is quoted here for future reference.

For the non viscous case of the axisymmetric jet impinging normally on the boundary he obtained:

Velocities

$$U = ar \qquad (7.1)$$

$$W = -2az \qquad (7.2)$$

Pressure

$$p = p_o - \tfrac{1}{2} \rho \; a^2 \, (r^2 + 4z^2) \qquad (7.3)$$

Where:

U is the radial velocity

W is the axial velocity

a is a constant

p_o is the stagnation pressure

Based on the above, the following form of solution was assumed for viscous flow:

$$U = r \, f' \, (z) \qquad (7.4)$$

$$W = -2 \, f \, (z) \qquad (7.5)$$

$$p = p_o - \tfrac{1}{2} \rho \; a^2 \left[r^2 + F \, (z) \right] \qquad (7.6)$$

Where f (z) and F (z) are new functions to be determined. By substituting into Navier-Stokes equations, two equations are obtained:

$$f'^2 - 2\,ff'' = a^2 + \nu\, f''' \qquad (7.7)$$

$$2\,ff' = a^2\, F' - \nu\, f'' \qquad (7.8)$$

Eliminating constant and introducing similarity transformation

$$\xi = \sqrt{\frac{a}{\nu}}\, z \qquad\qquad f\,(x) = \sqrt{a\nu}\;\phi\,(\xi)$$

The equations 7.7 and 7.8 reduce to

$$\phi''' + 2\,\phi\,\phi'' - \phi'^2 + 1 = 0 \qquad (7.9)$$

with applicable new boundary conditions. The solution of 7.9 was given in power series by F, Homann (14). N. Frossling (10) presented $\phi = u/U$ relations for ξ in the tabular form, to simplify calculations. There were also newer contributions to this problem like Strand (44), Tani and Komatsu (45).

Since velocities close to the stagnation point are small and the plate surface was smooth, the viscosity effects can be neglected. Schlichting's equations are therefore satisfactory in the vicinity of the stagnation point.

Inspection of equation 7.1 reveals that the radial velocity increases with increasing radius. This can only be true within close vicinity to the stagnation point, depending upon the source strength. The pressure distribution is parabolic, by equation 7.3. After reaching a maximum value, the velocity is decelerated and the equation 7.1 does not hold any more. In that region the viscous equations, 7.4, 7.5 and 7.6, are applicable.

According to measurements by Lee (25), the maximum velocity is reached at about $r/D = 1$ for nozzle-to-plate distances, $z_n/D < 20$. Having a plate curvature in this work much larger than the nozzle diameter, little error is made by considering the plate flat at the stagnation point. For nozzle diameters larger with respect to the plate curvature this error could be significant.

Deflection zone region is small. It seems to have no immediate practical application and was not considered a major part of the investigation.

Physically it was located at the bottom of the hemisphere and therefore accessibility of this region was limited.

CHAPTER 8

WALL JET ZONE

8.1 Pressure Distribution Along Impingement Plate

Pressure distribution along the impingement plate is shown on Figs. 28a, b and c. All the plots are for a nozzle diameter of 9.5 mm, at various nozzle-to-plate distances: $z_n/D = 13$, 9 and 7 and various Reynolds numbers. The curves have their maxima at the stagnation point, $s/D = 0$, from which they rapidly decrease with increased distance s/D and then asymptotically approach ambient pressure. From about $s/D = 3$, the pressure is insignificantly different from the ambient. The curves are practically independent of Reynolds number. Fig. 29 shows the mean shape of the curves. As anticipated, they become steeper as the impingement plate is brought closer to the nozzle.

It was observed that at the distance about $s/D = 10$ the static pressure measured on the surface of the plate was negative. Boundary shape and Coanda effect made the flow follow the plate contour.

8.2 Measurement of Boundary Layer Thickness

The boundary layer thickness on the concave surface of the hemispherical plate was measured with the Pitot tubes. The tubes were bent downstream of the probe to follow the shape of the hemisphere.

After the conditions of equilibrium at the required Reynolds number were reached, the probe was brought in contact with the plate surface under an angle perpendicular to the surface at the given station. This was accomplished with the aid of the positioning mechanism described in paragraph 3.5. Taking into account the probe tip diameter, a series of static or total pressure readings were recorded at various distances, z, on the normal to the station. The same procedure was repeated with the second (total or static) pressure measurements at the station, to complete the series. The results of these measurements gave velocity distributions at the stations located on the plate meridionals.

The boundary layer thickness is by definition the distance from the boundary to a point at which $V = V_{max}$. The location of this point on the velocity plot is usually questionable due to asymptotic growth of velocity. It is more distinct to base this definition on the point where $V = 0.99\ V_{max}$. This approach was used in the present analysis.

Figure 30 shows several of these points as typical. The boundary layer thickness was plotted on Figs. 31a, 31b and 31c, and the mean trend is shown on Fig. 32.

The test results do not indicate any regular, uniform pattern. A mean line approximates the boundary layer growth. It had been observed that the rapid pressure fluctuation reveals very unstable flow condition. The pressure fluctuated in a random manner, although the air supply system operation was steady. The boundary layer growth showed a strong time dependence.

To test the nature of this instability, a whisker of thread was attached to the tip of a thin, stiff wire and introduced into the boundary layer. The thread fluttered, as expected, but it also swirled randomly in the boundary layer region. The thread motion reveals the existence of intense vorticity in the boundary layer. The eddy axes were perpendicular to the direction of flow and parallel to the boundary.

It seems that the boundary layer growth occurring in the meridional direction is too rapid. The boundary layer thickness grows into the onrushing stream of higher velocity. There are two streams close together, the inner one having higher momentum than the outer. Since the geometry of the hemisphere is directing these two flows on a collision course, the two streams with different momentum collide. Since this takes place in a viscous continuum, the result is the vortex formation. The vortices roll away from the plate surface and are being carried away by the stream in a continuous fashion.

As observed, there was no definite time pattern. The instability of the pressure readings was not cyclic.

8.3 Velocity Decay Along the Plate

When analyzing the wall jet velocity, region IV on Figure 7, Glauert (11), following Prandtl's boundary layer concept, divided the flows into two categories:

1. The wall layer, where the boundary and viscous effects of the wall govern.

2. The outer layer, away from the wall, which has characteristics of a free, turbulent flow.

Maximum velocity in the velocity profile separates the two flow layers.

To represent the velocity profile in the outer layer of a flat plate, Poreh and Cermak (31) introduced a reference boundary velocity, V_{RB}, obtained by extrapolation of the outer layer velocity profile to the boundary as if no boundary existed. It is shown dotted on Fig. 7. This reference velocity can be considered a centerline velocity at a given distance from the stagnation point of a hypothetical free jet. This reference boundary velocity would be like a plane point flow spreading radially:

$$V_{RB} = \frac{\text{const}}{r} \tag{8.1}$$

In this case the velocity distribution for the outer layer can be represented by Goertler's (13) free jet equation:

$$\frac{V}{V_{RB}} = 1 - \tanh^2 k \frac{z}{r} \tag{8.2}$$

where k is the integration constant.

Von Karman (22) used the principle of integrated momentum equation in analyzing a steady flow. Applying this method and the concept of V_{RB} in two dimensional wall jet analysis, Abramovich (1) obtained results which were in good agreement with the measurements.

Lee (25) applied the same method for the investigation of a circular jet impinging on a flat plate and his results are also in good agreement with the measurements.

In this investigation the distance "r" has to be superseded by "s", which is a curvilinear distance measured on the hemispherical surface. Fig. 33 presents a summary of nine series of tests showing V_{RB}, the reference boundary velocity. The plots were taken at the following nozzle-to-plate dimensionless distances: $z/D = 13$, 9 and 7. At each distance three flows were investigated: Reynolds number 25,000; 50,000 and 75,000.

Intuitively, one expects that equation 8.1 would not hold for the case of the hemispherical plate. For a flat plate case the flow is spreading radially from the stagnation point

In the case of a hemispherical plate, concave side, the flow is spreading meridionally. Initially, in the proximity of the stagnation point, it is similar to the flat plate case. Further away, the direction of flow is gradually changing along the solid boundary of the hemisphere. In the final stage it is similar to a two directional flow in a pipe, where there is a high velocity, small cross section, central flow in one direction and a slow velocity, annular flow in the opposite direction.

The boundary geometries are different for the jets impinging on a flat plate and on a hemispherical plate. The boundaries shape the flow pattern, and for that reason the velocity distributions are different.

Considering that the width of the jet is proportional to r for the flat plate impinging jet, the flow area at any r is proportional to r squared, where r is unbounded.

For the hemispherical concave plate, the wall jet is confined to an annulus, whose outer radius is finite. It is therefore anticipated that the reference boundary velocity V_{RB} will be larger for the henispherical, concave plate jet than the corresponding velocity in the case of the flat plate jet. Maximum velocity decay measurements divided by nozzle exit velocity are shown on Figures 33a, 33b and 33c. The summary of these tests are shown on Figure 33d. The test results are consistent and reveal no dependence upon Reynolds number and plate-to-nozzle distance.

To have a general application, the formulae have to be dimensionless. For that purpose the distance from the stagnation point located at the bottom of the hemisphere to any given point on the hemisphere has to be measured not by the curvilinear distance, "s", but by the angle, $\theta = s/R$, where R is the radius of the hemisphere. Position angle θ is the enclosed angle between the sphere radii to the stagnation point and the station. At the stagnation point $\theta = 0$, while at the hemisphere rim it is $\pi/2$.

From the continuity equation one can deduce that the difference between V_{RB} for the hemispherical case and the flat plate jets will grow with the angle θ.

The chart on Fig. 33 was "normalized" with respect to the V_{RB}

velocities measured at $\theta = \pi/6 = 30^\circ$ which corresponds to station 8. The data points are indicated and the curve represents the purely empirical formula developed:

$$\frac{V_{RB}}{V_{RB8}} = \frac{\text{const}}{\theta \cos (3/5)\theta} = \frac{1}{2\,\theta \cos (3/5)\theta} \qquad (8.3)$$

or

$$V_{RB} \doteq V_{RB8} \frac{\text{const}}{2\theta \cos (3/5)\theta} = \frac{C_1}{\theta \cos (3/5)\theta} \qquad (8.3a)$$

The points for $z/D = 13$ at station 5 deviate from the curve but the velocity measurements for these points were taken within the region of the free jet. The Pitot tube measuring the velocity at station 5 was situated parallel to the plate while still in the region of the free jet impinging on it. These points should not be considered representative.

The Outer Layer

In a theoretical consideration of the hemispherical wall jet, the momentum equation will be applied as developed by von Karman in 1921. This approach was used by Abramovich for the two dimensional jet and by Lee for an axisymmetric jet impinging on a flat infinite plate.

Figure 7a represents the axial plane cross section of the control volume. The equation of conservation of momentum in segment ABCD is:

$$\Sigma \text{ momentum in} - \Sigma \text{ momentum out} = \Delta \text{ momentum in segment} \qquad (8.4)$$

Written out:

Momentum in thru AB + Momentum in thru BC +

- Momentum out thru CD - Momentum out thru DA =

= Momentum accumulation in the segment (8.5)

This equation holds under the following assumption:

Steady flow, $\frac{\partial}{\partial t}$ ( ) = 0

Constant density, ρ = const

Stationary ambient fluid, no external velocity disturbance

$$\tau = \frac{dv}{dz} = 0 \text{ at } V = V_m$$

This last assumption by Prandtl was satisfactory and was successfully used in many solutions, although more recent measurements by Poreh, Tsuei and Cermak (32) indicate that $\tau \neq 0$ at $V = V_{max}$ for the flat plate wall jet.

With these assumptions introduced, there is no accumulation of momentum in the control volume. In this case the right hand side of the equation vanishes. The condition of stationary ambient fluid justifies to disregard momentum influx thru the surface BC. The equation is therefore reduced to:

Momentum in thru AB - Momentum out thru CD +

- Momentum out thru DA = 0 (8.6)

The equation component in the plane normal to the jet axis of this vectorial quantity is applied.

The whole control volume has to be considered. Integration over the control volume gives:

$$\int_0^{2\pi} \rho V_o^2 b_o s_o \, d\varphi - \int_{s_o}^{s} \rho V_m \cos\theta \frac{\partial}{\partial l} \left[\int_0^{\delta} 2\pi V (R-z) \sin\theta \, dz \right] dl +$$

$$- \int_{\delta}^{b+\delta} \rho V^2 \, 2\pi \, (R-z) \sin\theta \cos\theta \, dz = 0 \qquad (8.7)$$

where:

R is the radius of hemisphere

θ is the position angle in vertical plane

φ is the angle in the horizontal plane

l is the curvilinear distance along the surface of integration

s is the distance along the hemispherical plane

Since the first term is in the region where the surface of integration is cylindrical, it can be written:

$$\int_0^{2\pi} \rho V_o^2 b_o s_o \, d\varphi = \rho V_o^2 b_o s_o \int_0^{2\pi} d\varphi = 2\pi \rho \, V_o^2 b_o s_o$$

Moreover, since ρ is nearly constant, i.e. the flow is incompressible, then 8.7 can be divided by $2\pi\rho$:

$$b_o s_o v_o^2 - \int_{s_o}^{s} V_m \cos\theta \frac{\partial}{\partial l} \left[\int_0^{\delta} V (R-z) \sin\theta \, dz \right] dl +$$

$$- \int_{\delta}^{b+\delta} V^2 (R-z) \cos\theta \sin\theta \, dz = 0 \qquad (8.8)$$

Equation 8.8 is not exact, the following approximations are introduced;

It was assumed that $\tau = 0$ at $V = V_m$. Air density is not exactly constant, since there is a measured pressure gradient along the flow. Velocity is assumed parallel to the plate surface. This is true only for the streamlines next to the plate. Velocities on streamlines further away from the plate divert more. In the second term of equation 8.7 and 8.8 the upper limit of integration is actually a distance along the path of V_m, and not a distance "s" measured along the hemisphere. Since the boundary layer is thin, the difference between these two is small enough to permit the substitution of the "s" for "l", therefore $l \doteq s = R\,\theta$. By introduction of the last relations into equation 8.8 one obtains, using a dummy variable:

$$b_o\, s_o\, V_o^2 - \int_{\theta_o}^{\theta} V_m \cos\alpha \,\frac{\partial}{\partial\alpha}\left[\int_0^{\delta} V\,(R-z)\,\sin\alpha \;dz\right] R\,d\alpha + - \int_{\delta}^{b+\delta} V^2\,(R-z)\,\cos\alpha\;\sin\alpha\;dz = 0 \qquad (8.9)$$

Since the rate of change along the hemisphere contour is required, 8.9 is differentiated with respect to α. Noting from Figure 7 that $V = 0$ at $z = b + \delta$ and $V = V_m$ at $z = \delta$ and returning from α to θ yields:

$$- V_m \cos\theta \int_0^{\delta} (R - z)\,\frac{\partial}{\partial\theta}\,(V \sin\theta)\;dz + -(R - \delta)\,V_m^2 \cos\theta\,\sin\theta\,\frac{\partial\delta}{\partial\theta} - \int_{\delta}^{b+\delta} (R-z)\,\frac{\partial}{\partial\theta}\,(V^2\cos\theta\,\sin\theta)\;dz + + (R - \delta)\,V_m^2 \cos\theta\,\sin\theta\,\frac{\partial\delta}{\partial\theta} = 0 \qquad (8.10)$$

The second and fourth terms cancel, therefore:

$$V_m \cos\theta \int_0^{\delta} (R - z)\frac{\partial}{\partial\theta}(V \sin\theta)\,dz + \\ + \int_{\delta}^{b+\delta} (R - z)\frac{\partial}{\partial\theta}(V^2 \cos\theta \sin\theta)\,dz = 0 \qquad (8.11)$$

To generalize, dimensionless parameters are introduced:

$$\bar{V} = \frac{V}{V_o}; \qquad \bar{V}_m = \frac{V_m}{V_o}; \qquad \bar{z} = \frac{z}{\delta} \qquad \text{and} \qquad \xi = \frac{z - \delta}{b}$$

$$\text{then also } d\bar{z} = \frac{dz}{\delta} \qquad\qquad d\,\xi = \frac{dz}{b}$$

after substituted into equation 8.11, one gets

$$\frac{V_m}{V_o}\,\delta \cos\theta \int_0^{1} (R - z)\frac{\partial}{\partial\theta}\left(\frac{V}{V_o} \sin\theta\right)\frac{dz}{\delta} + \\ + b\int_0^{1} (R - z)\frac{\partial}{\partial\theta}\left(\frac{V^2}{{V_o}^2} \cos\theta \sin\theta\right)\frac{dz}{d} = 0 \qquad (8.12)$$

or as expressed in the above notation

$$\bar{V}_m\,\delta \cos\theta \int_0^{1} (R - \delta\,\bar{z})\frac{\partial}{\partial\theta}(\bar{V} \sin\theta)\,d\bar{z} + \\ + b\int_0^{1} (R - \delta - b\,\xi)\frac{\partial}{\partial\theta}(\bar{V}^2 \cos\theta \sin\theta)\,d\xi = 0 \quad (8.13)$$

Primed symbols indicate differentiation with respect to θ in subsequent notation.

On performing the differentiation there results

$$\bar{V}_m \delta \cos\theta \int_0^1 (R - \delta z)(\bar{V}' \sin\theta + \bar{V} \cos\theta)\, dz + $$
$$+ b \int_0^1 (R - \delta - b\xi)(2\bar{V}\bar{V}'\cos\theta \sin\theta + $$
$$- \bar{V}^2 \sin^2\theta + \bar{V}^2 \cos^2\theta)\, d\xi = 0 \tag{8.14}$$

and introducing trigonometric identities yields

$$\bar{V}_m \delta \cos\theta \int_0^1 (R - \delta \bar{z})(\bar{V}' \sin\theta + \bar{V} \cos\theta)\, dz + $$
$$+ b \int_0^1 \left[(R - \delta - b\xi)(\bar{V}\bar{V}' \sin 2\theta + \bar{V}^2 \cos 2\theta)\right] d\xi = 0 \tag{8.14a}$$

Now within the boundary layer, i.e. for $\bar{z} = \frac{z}{\delta}$ from 0 to 1, velocity distribution can be defined according to Schlichting by the power law (32)

$$\bar{V} = \bar{V}_m (z)^{1/n} \tag{8.15}$$

where the symbols are as above and the exponent "n" is a weak function of Reynolds number. In older references, lower values were favored for "n". Newer test data done with more advanced laboratory equipment suggest higher "n" values for the investigated range of Reynolds numbers in turbulent wall jet flow. Reference (19) recommends values for "n" from 7.5 to 15.

Beyond the boundary layer, i.e. for region from δ to $b + \delta$ or $\bar{z}$ from 0 to 1, the following relation is used:

$$\bar{\bar{V}} = \bar{\bar{V}}_m \left(1 - \xi^{3/2} \right)^2 \qquad (8.16)$$

This equation gave good agreement with measurements conducted by Poreh and Cermak (31) and Lee (25). For thickness of the wall jet, according to the present investigation summarized on Fig. 34, the following relation is accepted:

$$b = 0.226\ R\ (\theta - \theta_o) = 0.226\ R\ \Delta\theta \qquad (8.17)$$

which is very close to that used by Lee for a flat plate impinging jet:

$$b = 0.22\ (r - r_o)$$

For boundary layer thickness, the results obtained in the present investigation which are summarized on Figures 34 and 35 give

$$\frac{\delta}{b} = 0.05434 \doteq \frac{1}{18} \qquad (8.18)$$

This last relation is significantly different from the flat plate investigation in which Lee obtained:

$$\frac{\delta}{b} = \frac{1}{10}$$

Differentiation of equations 8.15, 8.16 and 8.17 with respect to θ gives:

In boundary layer region:

$$\frac{\partial \bar{V}}{\partial \theta} = \frac{\partial}{\partial \theta} (\bar{V}_m \bar{Z}^{1/n}) = \bar{Z}^{1/n} (\bar{V}_m' - 1/n \, \bar{V}_m \frac{\delta'}{\delta}) \qquad (8.19)$$

$$\text{for } 0 \leqslant \bar{Z} \leqslant 1$$

And in outer region, the formula

$$\frac{\partial \bar{V}}{\partial \theta} = \frac{\partial}{\partial \theta} \left[\bar{V}_m (1 - \xi^{3/2})^2 \right] =$$

$$= \bar{V}_m' (1 - \xi^{3/2})^2 + \frac{3 \bar{V}_m \delta'}{b} \xi^{\frac{1}{2}} (1 - \xi^{3/2}) +$$

$$+ \frac{3 \bar{V}_m b'}{b} \xi^{3/2} (1 - \xi^{3/2})$$

$$\text{for } 0 \leqslant \xi \leqslant 1 \qquad (8.20)$$

Also the rate of growth of wall jet thickness is:

$$\frac{db}{d\theta} = \frac{d}{d\theta} \left[0.226 \, R \, (\theta - \theta_0) \right] = 0.226 \, R \qquad (8.21)$$

Introduction of 8.15, 8.16, 8.19 and 8.20 into 8.14 and dividing by cos 2θ, $(0 < \theta < \pi/2)$ gives:

$$\bar{V}_m \delta \frac{\cos \theta}{\cos 2\theta} \int_0^1 (R - \delta - \bar{z}) \left[\bar{z}^{1/n} (\bar{V}' - 1/n \, \bar{V}_m \frac{\delta'}{\delta}) \sin \theta + \right.$$

$$\left. + \bar{V}_m \bar{z}^{1/n} \cos \theta \right] d\bar{z} +$$

$$+ b \int_0^1 \left\{ (R - \delta - b\xi) \left[\bar{V}_m (1 - \xi^{3/2})^2 \right] \left[\bar{V}'_m (1 - \xi^{3/2})^2 + \right.\right.$$

$$\left. + \frac{3\bar{V}_m \delta'}{b} \xi^{\frac{1}{2}} (1 - \xi^{3/2}) + \frac{3\bar{V}_m b'}{b} \xi^{3/2} (1 - \xi^{3/2}) \right] \tan 2\theta +$$

$$\left. + \bar{V}_m^2 (1 - \xi^{3/2})^4 \right\} d\xi = 0 \qquad (8.22)$$

The rest of the computation is shown in Appendix A, where the reference number is started with the subsequent equation.

The resulting equations obtained for the exponent $n = 14$ are:

<u>Solution by polynomial interpolation</u>

For $\theta \leqslant 47^\circ$

$$\bar{V}_m = \frac{V_m}{V_{mo}} = \left(\frac{1 - a\theta_o}{1 - a\theta}\right)^{.4708} \left(\frac{\theta_o}{\theta}\right)^{.5374} e^{I(\theta_o) - I(\theta)} \qquad (8.23a)$$

for $\theta > 47^\circ$

$$\bar{V}_m = \frac{V_m}{V_{mo}} = \bar{V}_{m47^\circ} \left(\frac{1 - a\theta_1}{1 - a\theta}\right)^{.4708} \left(\frac{\theta_1}{\theta}\right)^{.5374} e^{I(\theta_1) - I(\theta)} \qquad (8.23b)$$

where:

$a = 0.0561$

$\theta_o = 10.9^\circ \doteq 0.19$ in radians

$\theta_1 = 47^\circ$ expressed in radians

$\bar{V}_{m47^\circ} = \dfrac{V_m}{V_{mo}}$ evaluated at $\theta_1 = 47^\circ$

$$I(\theta_o) - I(\theta) = -\left[6.98 (\theta - \theta_o) - 16.89 (\theta^2 - \theta_o^2) + \right.$$

$$+ 25.63 (\theta^3 - \theta_o^3) - 23.54 (\theta^4 - \theta_o^4) + 11.67 (\theta^5 - \theta_o^5) +$$

$$\left. - 2.44 (\theta^6 - \theta_o^6) \right]$$

and correspondingly $I(\theta_1) - I(\theta)$ with proper symbols.

Solution by series expansion

For $\theta \leqq 64.3^\circ$

$$\bar{V}_m = \frac{V_m}{V_{mo}} = \left(\frac{\theta_o}{\theta}\right)^{1.075} e^{0.3216\,(\theta^2-\theta_o^2) + 0.04154\,(\theta^4-\theta_o^4)} \qquad (8.24a)$$

For $\theta > 64.3^\circ$

$$\bar{V}_m = \frac{V_m}{V_{mo}} = \bar{V}_{m\,64.3^\circ} \left(\frac{\theta_2}{\theta}\right)^{1.075} e^{0.3216\,(\theta_2^2-\theta^2) + 0.04154\,(\theta_2^4-\theta^4)} \qquad (8.24b)$$

where: $\theta_2 = 64.3^\circ$

In equations 8.23 and 8.24 the reference points θ_1 and θ_2 are determined by the location where the approximate integrand crosses the abscissa. In this manner the formulae for velocity becomes simpler as opposed to using θ_o at the beginning of integration.

Empirical equation

$$\bar{V}_m = \frac{V_m}{V_{mo}} = \left(5.29\,\theta \cos \frac{\theta}{2}\right)^{-1} \qquad (8.25)$$

In these equations the following values are applicable:

$\theta_o = \frac{S_o}{R} = 0.19$ is the initial position angle in radians, constant in this study, as demonstrated in Figure 34.

$V_o = V_{m5}$ is the initial velocity, which in this investigation is equal to the maximum velocity at station 5, at 10.9°.

Equations 8.23, 8.24 and 8.25 represent the maximum velocity decay of the wall jet at the concave side of the hemispherical plate for the range of $14{,}000 < Re < 75{,}000$ with the exponent $n = 14$.

It became evident from the data obtained that maximum velocity decay depends upon nozzle-to-plate distance. The reduction relation used for plotting is:

$$\frac{V_m}{V_{m5}} = \left(\frac{V_m}{V_{m5}}\right)_m \left[\left(\frac{z}{D}\right) \left(\frac{z}{D}\right)_r\right]^{\alpha} \qquad (8.26)$$

where:

$\left(\frac{V_m}{V_{m5}}\right)_m$ is measured ratio

$\left(\frac{z}{D}\right)_r$ is reference $\frac{z}{D} = 10$

α is the exponent as shown on Figure 36b

All the values are functions of the initial velocity which is maximum velocity at station 5, i.e. at $\theta = 10.9^{\circ}$.

In all three equations: 8.23, 8.24 and 8.25 the angle θ is expressed in radians. The following tabulation compares wall jet maximum velocity decay calculated from the three equations.

Table I

Comparison of Maximum Velocity Decay Calculated by Equations 8.23, 8.24 and 8.25

Velocity Ratio	Eqn. 8.23	Eqn. 8.24	Eqn. 8.25
$V_m\ 10.9^o/V_o$	1	1	1
$V_m\ 14.6/V_o$	0.736	0.739	0.751
$V_m\ 22.4^o/V_o$	0.475	0.479	0.493
$V_m\ 38^o\ /V_o$	0.299	0.300	0.301
$V_m\ 47^o/V_o$	0.261	0.260	0.252
$V_m\ 53^o/V_o$	0.243	0.245	0.228
$V_m\ 64/V_o$	0.202	0.235	0.199
$V_m\ 68.5^o/V_o$	0.185	0.204	0.191
$V_m\ 80^o/V_o$	0.124	0.136	0.177
$V_m\ 83.4^o/V_o$	0.102	0.119	0.174

Figure 36 shows the test points marked and the curves are by equations 8.23 and 8.24, equation 8.25 is shown in Figure 36a for clarity.

The agreement of the curve with test points may be considered satisfactory. Equation 8.23 is most cumbersome to use. Equation 8.24 is quite handy, in comparison to 8.23. The simplest is the empirical equation 8.25.

The curves representing equations 8.23 and 8.24 deviate from the test results close to the rim of the hemisphere. Maximum wall jet velocity decay in this region calculated by equations 8.23 and 8.24 fall below the measured values. The difference between the test results and calculated values diminishes if the reduction equation 8.26 is not used on test values in this boundary region. Empirical equation, 8.25, gives best results in the whole range.

The agreement obtained between the experimental results and the curve could indicate that the assumption of $\tau = 0$ at $V = V_m$ incurred negligible error. This assumption was used by M. B. Glauert (11) in the analysis of wall jets.

Equations 8.23, 8.24 and 8.25 being dimensionless, can be applied to any size hemispherical plate. The first and second equations express maximum velocity decay in terms of the angle θ, once the initial velocity V_o is determined. The empirical equation, 8.25, assumes the value of "1" at this point of $\theta = 10.9^o$ and references the rest to it. All the equations have the numerical coefficients for Reynolds numbers $14{,}000 < R_e < 75{,}000$, for which $n = 15$ along with jet width and boundary layer thickness as given by equation 8.17 and 8.18.

For investigation of maximum velocity decay outside of the present range of Reynolds numbers, a proper value for the exponent "n" would have to be established.

This value would be inserted into equation A.2 and the modified coefficients in equation A.6 would be found. Although with different coefficients, equations 8.23 and 8.24 would have the same form.

The deviation of the results obtained from the equations 8.23 and 8.24 and the velocities measured close to the edge of the hemisphere is explainable also by the fact that the entire boundary layer must be small with respect to the significant dimension of the system. In this case this dimension is R, the radius of the hemisphere (41). In the present investigation the ratio of $(b + \delta)$ to R for $\theta > 80^\circ$ was close to 1/3 which cannot be considered small.

The present problem is handled essentially by a modified boundary layer treatment in the integrated form. It refers to the fact that, for boundary layer flow over bodies of revolution, the governing equations are the same as for two dimensional flow. Difference exists, however, in the form of the continuity equation*) which is fully observed in the present approach. When the boundary layer treatment of the problem is physically attainable, the present method will also show it as a deviation between the experimental results and the calculated curve. A much more powerful method would be needed, requiring perhaps integration of the turbulent Navier-Stokes equation.

---

*) Schlichting (41), p. 190

CHAPTER 9

VISCOUS SHEAR FORCE AT THE WALL

For consideration of viscous shear force at the wall, a control volume ADEA is chosen, as shown on Figure 7a. The momentum equation component in this control volume adjacent to the wall is taken in the plane normal to the impinging jet axis.

The result of the calculation performed in the Appendix B, with the equation numbers preserved, is:

$$\frac{\tau_w}{\rho U_{oc}^2} = F \left(\frac{\theta}{\theta_o}\right)^{-2\alpha} \qquad (9.1)$$

In order to compare these results with those obtained for the flat wall jet, one can refer to Lee (25) and Poreh, Tsuei and Cermak (32). An equivalence to equation 9.1 was given in the form:

$$\frac{\tau_w}{\rho U_{oc}^2} = F \left(\frac{r}{Z_n}\right)^{-2\alpha + a - 1} \qquad (9.2)$$

in which Lee (25) had

$$F = \frac{n}{(n+1)\,(n+2)}\; A^2 B\,(\alpha n + a + 1) \qquad (9.$$

In the present investigation, the boundary layer thickness, expressed by equation B.15 is

$\delta = B R \theta$ which can be written: $\delta = B R \theta^a$

where $a = 1$

Based on this, the expressions for hemispherical plate and flat plate friction force are similar, as it can be seen by equations 9.1 and 9.2. In both the exponent is equal to:

$$-2\alpha + a + 1$$

The term F, represented by equation B.19 for the hemispherical plate and by equation 9.3 for the flat plate differ significantly in spite of their apparent similarity. The difference is functional. This term for the flat plate, equation 9.3 is a function of "n", which is a weak function of the Reynolds number. For the flat plate at an established α and "a" in the range of Reynolds number investigated it is just a coefficient. Intuitively, $\tau/\rho U_{oc}^2$ should be a function of the Reynolds number.

The corresponding term for the hemispherical plate is a local function with the angle variable θ. For that reason its practical application is limited.

CHAPTER 10

BOUNDARY LAYER THICKNESS NEAR STAGNATION POINT

For calculation of boundary layer thickness near the stagnation point, one can use formula given in (19) after Schlichting

$$\frac{\delta}{D} = \frac{2.788}{\sqrt{a * Re}} \qquad (10.1)$$

in which "a" is the coefficient when expressing velocity in the form:

$U = a\ s$ as in (7.1)

The symbol "s" is the distance from the stagnation point, measured along the impingement surface.

In the present investigation D = 6.35 mm

Taking as an example one of the tests for which $Z_n/D = 7$,

$U_{oc} = 402.5$ ft/s $s = 35.56$ mm $R_e = 48,000$

One obtains $a* = \frac{aD}{U_{oc}} = 0.1786$

Therefore,

$$\frac{\delta}{D} = \frac{2.788}{\sqrt{a * R_e}} = 0.0299 \qquad (10.2)$$

This value compares favorably with that calculated for the flat plate case (19), where it was

$$\frac{\delta}{D} = 0.02765 \qquad (10.3)$$

The actual measurement of the boundary layer thickness near the stagnation point was not attempted due to physical restrictions. The measurements would have to be done at the bottom of the hemispherical surface on its concave side and using relatively large probes to measure small dimensions. The smallest probe diameters available for the test was 0.4 mm, while the boundary layer thickness was of the order of 0.2 mm. The measurements taken under such conditions would not be satisfactory.

CHAPTER 11

VELOCITY PROFILE IN THE JET WALL ZONE

The mean velocity profile measurements in the wall zone are presented on the plot Fig. 37. Figures 37a to 37g show the profiles at some selected stations. The Reynolds number range investigated was 10,000 to 78,000 and dimensionless distance from the nozzle-to-plate, z/D = 7, 9 and 13. The velocity measurements were taken on normals at the station indicated. The velocity profiles measured are in good agreement with the formula 8.16:

$$\frac{V}{V_m} = (1 - \xi^{3/2})^2$$

These results therefore confirm the results obtained by Poreh and Cermak (31) and Lee (25).

The velocity profiles were identical for all points above $z/z_{\frac{1}{2}} = 0.2$ at all distances from the issuing nozzle. There were small differences closer to the wall. Figure 38 depicts the general trend in the wall jet spread.

CHAPTER 12

SUMMARY AND CONCLUSION

This study was mostly concerned with the wall jet zone in the case of hemispherical concave, smooth surface. The range of Reynolds number was from about 14,000 to 75,000, which corresponds to Mach number from about 0.1 to about 0.5. This range was selected due to the suitability of the available testing equipment.

Reynolds numbers lower than 10,000 represent small velocities in the order of 20 m/s and less. The measurement of such low velocities requires very sensitive instruments.

Reynolds numbers higher than 75,000 represent velocities in the order of 200 m/s and higher. At such velocities the probes began to vibrate violently when inserted into the jet. Pitot tubes would have to be much more rigidly built to take measurements at such velocities and the effect of compressibility would have to be included.

Eight important observations were made in this study.

1. The jet is not throttled easily. When the impingement plate is only two nozzle diameters away from the jet issuing nozzle, the flow is still practically unrestricted. This confirms previously made observations by other researchers, yet it has not found many practical applications. The use of screens and guides was suggested (17) for restricting hot streams discharged into the environment. By placing baffles close to hot stream outlets discharging into the lakes one

can localize warm spots and dissipate heat gradually. It is known that, if unrestricted, the hot streams travel long distances thermally polluting lake and river water and affecting aquatic life.

2. The results of this work, published in "Letters in Heat and Mass Transfer" (16), indicate that the minimum static pressure of the free jet is located 8 nozzle diameters from the nozzle outlet. These tests were run with three nozzle diameters: 3.2, 6.35 and 9.5 mm. When the impingement plate was moved closer to the nozzle exit, the minimum pressure point was also moved closer to the nozzle. The location of minimum pressure point was found to be independent of nozzle diameter and Reynolds number. This last phenomenon is surprising since it means that no matter what the exit velocity was, the lowest static pressure would always fall at the same point, 8 nozzle diameters away from the nozzle exit in the unrestricted jet.

While the location of minimum static pressure is fixed in space, the value of the minimum does depend upon Reynolds number. The higher the Reynolds number, the lower the depression for the range of Reynolds number in this study.

3. Compared with flat plate experiments, the maximum velocity decay of comparable jets was less rapid for the concave, hemispherical plate. Such behavior of the jet could be predicted from the plate geometrical differences forming the boundaries in the incompressible flow.

4. The strong vorticity found in this investigation seemed to intensify turbulence. The vortices were formed in such a way that their

axes were parallel longitudinally to the hemispherical plate. It indicates that heat transfer by convection in such a condition is greater. The vortices formed in the hot boundary layer carry away heat into the colder region of higher velocity.

5. The boundary layer thickness in the developed wall jet zone of the hemispherical plate was measured to be about half of that measured in (21) for the flat plate. It is significant in heat transfer, as related by Prandtl's modification of Reynolds analogy. At Prandtl number close to unity for air, the velocity profile is similar to the temperature profile hence the velocity and thermal boundary layer thicknesses are nearly the same. The thermal gradient is higher for thinner boundary layer. Since heat conducted through unit surface per unit time is by Fourier conduction law:

$$Q = - k \frac{\partial T}{\partial z}$$

where: k = conductivity in Btu/hr ft $^{\circ}$F

$\left.\frac{\partial T}{\partial z}\right|_{z = 0}$ = temperature gradient at the wall, in $^{\circ}$F/ft

Based on the above, one can conclude that the hemispherical plate conducts heat at a higher rate than a flat plate when impinged by an identical jet.

This is not a proof, since the gradient, $\frac{\partial T}{\partial z}$, is to be evaluated at $z = o$ of the temperature profile T (a), which is not exactly known.

The ultimate proof would be to measure the heat transfer of the heated hemispherical plate when blown on by an air jet. Such experiments were not in the scope of this investigation, but confirmation of this corollary is found in (8), by Dyban and Mazur, who measured heat transfer rate in concave and flat plates, when impinged upon by an air jet. According to these tests, the rate of heat transfer for a concave plate is about 35 to 40% higher than for a flat plate under identical conditions.

6. The method of measuring the boundary layer thickness with the probes available was not practical near the stagnation point. The Pitot tubes were too large for measuring small distances.

7. The empirical relations of "reference boundary velocity" decay and maximum velocity decay in the wall jet, equations 8.3 and 8.25 respectively established in this work, give useful predictions for the investigated range of Reynolds number.

8. Equation 8.23 for maximum velocity decay in the wall jet based on the theoretical consideration gives good agreement with measurements. In the Reynolds number range investigated it is a function of the local angle only. It is independent of Reynolds number, radius of curvature of the hemisphere and the nozzle diameter. Practically it means that this relation can be used for any velocity in the range investigated and for any size of the hemisphere.

Recommendation

In future research of subsonic jets, the hemispherical, convex plate draws the first attention. Normally impinging and skew axial jets provide a large field for investigation.

Parabolic and hyperbolic surfaces may also find practical application. Hyperbolic shape cooling towers have the best natural draft performance. They can be thought of as huge jet issuing nozzles in which gravity effects have a major role but were negligible in this study.

It is logical to conduct small scale, model tests and extend the information to large applications, considering scale factors.

Large scale test equipment is costly to furnish and run.

New Jersey Institute of Technology
Newark, New Jersey
April, 1978

APPENDIX A

The Continuation of Calculation of the Maximum Velocity Decay in the Wall Jet, for Chapter 8, Page 48

For simplicity the two integrals in equation 8.22 are solved separately. The solution of the first one is:

$$
\begin{aligned}
&\bar{V}_m\,\delta\,\frac{\cos\theta}{\cos 2\theta}\int_0^1 (R-\bar{z})\Big[\bar{z}^{1/n}\big(\bar{V}'_m - 1/n\bar{V}_m\frac{\delta'}{\delta}\big)\sin\theta \;+\\
&+\bar{V}_m\,(\bar{z})^{1/n}\cos\theta\Big]\,dz = \bar{V}_m\,\delta\,\frac{\cos\theta}{\cos 2\theta}\Big\{R\,\frac{n}{n+1}\,\bar{z}^{\frac{n+1}{n}}\Big[\big(\bar{V}'_m \;+\\
&-1/n\,\bar{V}_m\frac{\delta'}{\delta}\big)\sin\theta+\bar{V}_m\cos\theta\Big] - \frac{\delta\,n}{2n+1}\,\bar{z}^{\frac{2n+1}{n}}\Big[\big(\bar{V}'_m \;+\\
&-1/n\,\bar{V}_m\frac{\delta'}{\delta}\big)\sin\theta+\bar{V}_m\cos\theta\Big]\Big\}\Bigg|_{\bar{z}=0}^{\bar{z}=1} =\\
&\approx\bar{V}_m\,\delta\,\frac{\cos\theta}{\cos 2\theta}\Big\{R\,\frac{n}{n+1}\Big[\big(\bar{V}'_m - 1/n\,\bar{V}_m\frac{\delta'}{\delta}\big)\sin\theta+\bar{V}_m\cos\theta\Big] \;+\\
&-\delta\,\frac{n}{2n+1}\Big[\big(\bar{V}'_m - 1/n\,\bar{V}_m\frac{\delta'}{\delta}\big)\sin\theta+\bar{V}_m\cos\theta\Big]\Big\} =\\
&\approx\bar{V}_m\,\delta\,\frac{\cos\theta}{\cos 2\theta}\Big(\frac{Rn}{n+1}-\frac{\delta\,n}{2n+1}\Big)\Big[\big(\bar{V}'_m - 1/n\,\bar{V}_m\frac{\delta'}{\delta}\big)\sin\theta \;+\\
&+\bar{V}_m\cos\theta\Big]
\end{aligned}
$$

The second integral:

$$\overline{V}_m b (R - \delta) \int_0^1 \{ (1 - \xi^{3/2})^2 [\overline{V}_m' (1 - \xi^{3/2})^2 +$$

$$+ \frac{3\overline{V}_m \delta'}{b} \xi^{\frac{1}{2}} (1 - \xi^{3/2}) + \frac{3\overline{V}_m b'}{b} \xi^{3/2})(1 - \xi^{3/2})] \tan 2\theta +$$

$$+ \overline{V}_m (1 - \xi^{3/2})^4 \} d\xi - \overline{V}_m b^2 \int_0^1 \{ (1 - \xi^{3/2})^2 \xi [\overline{V}_m' (1 - \xi^{3/2})^2 +$$

$$+ \frac{3\overline{V}_m \delta'}{b} \xi^{\frac{1}{2}} (1 - \xi^{3/2}) + \frac{3\overline{V}_m b'}{b} \xi^{3/2} (1 - \xi^{3/2})] \tan 2\theta +$$

$$+ \overline{V}_m (1 - \xi^{3/2})^4 \xi \} d\xi = \overline{V}_m b (R - \delta) \int_0^1 \{ [\overline{V}_m' (1 - 4\xi^{3/2} +$$

$$+ 6\xi^3 - 4\xi^{9/2} + \xi^6) + \frac{3\overline{V}_m \delta'}{b} (\xi^{\frac{1}{2}} - 3\xi^2 + 3\xi^{7/2} - \xi^5) +$$

$$+ \frac{3\overline{V}_m b'}{b} (\xi^{3/2} - 3\xi^3 + 3\xi^{9/2} - \xi^6)] \tan 2\theta +$$

$$+ \overline{V}_m (1 - 4\xi^{3/2} + 6\xi^3 - 4\xi^{9/2} + \xi^6) \} d\xi +$$

$$- \bar{V}_m b^2 \int_0^1 \left\{ \left[\bar{V}_m' (\xi - 4\xi^{5/2} + 6\xi^4 - 4\xi^{11/2} + \xi^7) + \right. \right.$$

$$+ \frac{3\bar{V}_m \delta'}{b} (\xi^{3/2} - 3\xi^3 + 3\xi^{9/2} - \xi^6) +$$

$$\left. + \frac{3\bar{V}_m b'}{b} (\xi^{5/2} - 3\xi^4 + 3\xi^{11/2} - \xi^7) \right] \tan 20 +$$

$$\left. + \bar{V}_m (\xi - 4\xi^{5/2} + 6\xi^4 - 4\xi^{11/2} + \xi^7) \right\} d\xi =$$

$$\doteq \bar{V}_m b (R - \delta) \left\{ \left[\bar{V}_m' 0.31558 + \frac{\bar{V}_m \delta'}{b} 0.5 + \frac{\bar{V}_m b'}{b} 0.1578 \right] \tan 2\theta + \right.$$

$$\left. + \bar{V}_m 0.31558 \right\} - \bar{V}_m b^2 \left\{ \left[\bar{V}_m' 0.06676 + \frac{\bar{V}_m \delta'}{b} 0.1578 + \right. \right.$$

$$\left. \left. + \frac{\bar{V}_m b'}{b} 0.06676 \right] \tan 2\theta + \bar{V}_m 0.06676 \right\}$$

Substituting the components back into 8.22 yields:

$$\bar{V}_m \frac{Rn}{n+1} \delta \frac{\cos\theta}{\cos 2\theta} \left[(\bar{V}_m' - 1/n \, \bar{V}_m \frac{\delta'}{\delta}) \sin\theta + \bar{V}_m \cos\theta \right] +$$

$$- \bar{V}_m \frac{\delta^2 n}{2n+1} \frac{\cos\theta}{\cos 2\theta} \left[(\bar{V}_m' - 1/n \, \bar{V}_m \frac{\delta'}{\delta}) \sin\theta + \bar{V}_m \cos\theta \right] +$$

$$Rb \Bigg\{ \Big[\bar{V}'_m \, 0.31558 + \bar{V}_m \frac{\delta'}{b} 0.5 + \bar{V}_m \frac{b'}{b} 0.1578 \Big] \tan 2\theta +$$

$$\bar{V}_m \, 0.31558 \Bigg\} - b \, \delta \Bigg\{ \Big[\bar{V}'_m \, 0.31558 + \frac{\bar{V}_m \, \delta'}{b} \, 0.5 +$$

$$+ \frac{\bar{V}_m b'}{b} 0.1578 \Big] \tan 2\theta + \bar{V}_m \, 0.31558 \Bigg\} - \bar{V}_m b^2 \Bigg\{ \Big[\bar{V}'_m \, 0.06676 +$$

$$+ \frac{\bar{V}_m \, \delta'}{b} 0.1578 + \frac{\bar{V}_m b'}{b} 0.06676 \Big] \tan 2\theta + \bar{V}_m \, 0.06676 \Bigg\} = 0$$

(A.1)

Dividing by $\bar{V}_m$ tan 2θ:

$$R \, \delta \Bigg\{ \frac{n}{2(n+1)} \Big[\Big(\bar{V}'_m - 1/n \, \bar{V}_m \frac{\delta'}{\delta} \Big) + \bar{V}_m \cot \theta \Big] \Bigg\} +$$

$$- \delta^2 \Bigg\{ \frac{n}{2(2n+1)} \Big[\Big(\bar{V}'_m - 1/n \, \bar{V}_m \frac{\delta'}{\delta} \Big) + \bar{V}_m \cot \theta \Big] \Bigg\} +$$

$$+ b \, (R - \delta) \, 0.31558 \, \bar{V}'_m + (R - \delta) \, \bar{V}_m \, \delta' 0.5 + (R - \delta) b' \, \bar{V}_m 0.1579 +$$

$$+ b \, (R - \delta) \, \bar{V}_m 0.31558 \cot 2\theta - b^2 \, \bar{V}'_m 0.06676 - b \, \delta \, \bar{V}_m 0.1578 +$$

$$- bb' \, \bar{V}_m 0.06676 - b^2 \, \bar{V}_m 0.06676 \cot 2\theta = 0$$

(A.2)

Equations 8.17 and 8.18 in which $\theta_o = 0$ gives:

$b = 0.226 \; R \Delta \theta = 0.226 \; R \; \theta$ $\qquad$ $b' = 0.226 \; R$

$\delta = 0.01228 \; R \quad \theta = 0.01228 \; R \; \theta$ $\qquad$ $\delta' = 0.01228 \; R$

$\delta'/b = 0.05434 \; 1/\theta$

$b'/b = 1/\theta$

$\delta'/\delta = 1/\theta$

Exponent "n" used in equation 8.15 for the range of Reynolds numbers in the present investigation is n = 14 as suggested by (19). For checking purposes, the particular values are used here.

Introducing the above into equation A.2 yields:

$$0.01228\ R^2\ \theta \left[\frac{14}{30} \left(\bar{V}'_m - \frac{1}{14} \bar{V}_m \frac{1}{\theta} + \bar{V}_m \cot \theta\right) \right] \ +$$

$$-\ 0.01228^2\ R^2\ \theta^2 \left[\frac{14}{58} \left(\bar{V}'_m - \frac{1}{14} \bar{V}_m \frac{1}{\theta} + \bar{V}_m \cot \theta\right) \right] +$$

$$+\ 0.226\ R^2\ \theta\ 0.31558\ \bar{V}'_m - 0.226\ R^2\ \theta^2\ 0.01228 \times 0.31558\ \bar{V}'_m\ +$$

$$+\ \tfrac{1}{2} \times 0.01228\ R^2\ \bar{V}_m - \tfrac{1}{2} \times 0.01228^2\ R^2\ \theta^2\ \bar{V}_m + 0.226\ R^2\ 0.1578\ \bar{V}_m\ +$$

$$-\ 0.01228\ R^2\ \theta\ 0.226 \times 0.1578\ \bar{V}_m + 0.226\ R^2\ \theta\ 0.31558\ \bar{V}_m \cot 2\theta\ +$$

$$-\ 0.226\ R^2\ \theta^2\ 0.01228 \times 0.31558\ \bar{V}_m \cot 2\theta\ \ +$$

$$-\ 0.226^2\ R^2\ \theta^2\ 0.06676\ \bar{V}'_m - 0.226\ R^2\ \theta\ 0.01228 \times 0.1578\ \bar{V}_m\ +$$

$$+\ 0.226^2\ R^2\ \theta\ 0.06676\ \bar{V}_m - 0.226^2\ R^2\ \theta\ 0.06676\ \bar{V}_m \cot 2\theta = 0$$

(A.3)

Multiplying the terms and dividing by 0.01228 R^2 one obtains:

$$0.46667\ \theta\ \overline{V}'_m - 0.03333\ \overline{V}_m + 0.46667\ \theta\ \overline{V}_m \cot\theta +$$

$$- 0.002964\ \theta^2\ \overline{V}'_m + 0.0002117\ \theta\ \overline{V}_m - 0.002964\ \theta^2\ \overline{V}_m \cot\theta +$$

$$+ 5.808\ \theta\ \overline{V}'_m + 3.405\ \overline{V}_m + 5.808\ \overline{V}_m\ \theta \cot 2\theta +$$

$$- 0.2777\ \theta^2\ \overline{V}'_m - 0.3133\ \theta\ \overline{V}_m - 0.2777\ \overline{V}_m\ \theta^2 \cot 2\theta +$$

$$- 0.07132\ \theta^2\ \overline{V}'_m - 0.04181\ \theta\ \overline{V}_m - 0.07132\ \overline{V}_m\ \theta^2 \cot 2\theta = 0 \qquad (A.4)$$

Collection of similar terms yields:

$$6.275\ \theta\ \overline{V}'_m - 0.3520\ \theta^2\ \overline{V}'_m + 3.372\ \overline{V}_m - 0.3549\ \theta\ \overline{V}_m +$$

$$+ 0.4667\ \overline{V}_m\ \theta \cot\theta - 0.002964\ \overline{V}_m\ \theta^2 \cot\theta +$$

$$+ 5.808\ \overline{V}_m\ \theta \cot 2\theta - 0.3490\ \overline{V}_m \theta^2 \cot 2\theta = 0 \qquad (A.5)$$

Dividing by 6.275 and collecting:

$$\overline{V}'_m\ (1 - 0.0561\ \theta)\ \theta + 0.5374\ \overline{V}_m - 0.05656\ \theta\ \overline{V}_m +$$

$$+ 0.07437\ \theta\ \overline{V}_m \cot\theta - 0.000472\ \theta^2\ \overline{V}_m \cot\theta + 0.9256\ \theta\ \overline{V}_m \cot 2\theta +$$

$$- 0.05562\ \theta^2\ \overline{V}_m \cot 2\theta = 0 \qquad (A.6)$$

Using the symbols:

$a = 0.0561$ $A = 0.5374$ $B = 0.05656$

$C = 0.07437$ $D = 0.000472$ $E = 0.9256$

$F = 0.05562$

Introducing these symbols into the equation:

$$\overline{V}'_m (1 - a\,\theta)\,\theta + A\,\overline{V}_m - B\,\theta\,\overline{V}_m + C\,\theta\,\overline{V}_m \cot\theta +$$

$$- D\,\theta^2\,\overline{V}_m \cot\theta + E\,\theta\,\overline{V}_m \cot 2\theta - F\,\theta^2\,\overline{V}_m \cot 2\theta = 0$$

Dividing by $\overline{V}_m (1 - a\,\theta)\,\theta$, where $\theta \neq 0$, $\theta \neq 1/a$

$$\frac{\overline{V}'_m}{\overline{V}_m} + A\,\frac{1}{(1 - a\,\theta)\,\theta} - B\,\frac{1}{1 - a\,\theta} + C\,\frac{\cot\theta}{1 - a\,\theta} - D\,\frac{\theta\cot\theta}{1 - a\,\theta} +$$

$$+ E\,\frac{\cot 2\theta}{1 - a\,\theta} - F\,\frac{\theta\cot 2\theta}{1 - a\,\theta} = 0 \tag{A.7}$$

Since $\overline{V}'_m = \dfrac{d\,\overline{V}_m}{d\,\theta}$, equation A.7 can be integrated:

$$\ln \overline{V}_m + A \int \frac{d\,0}{(1 - a\,\theta)\,\theta} - B \int \frac{d\,\theta}{1 - a\,\theta} + C \int \frac{\cot\theta}{1 - a\,\theta}\,d\,\theta +$$

$$- D \int \frac{\theta\cot\theta}{1 - a\,\theta}\,d\,\theta + E \int \frac{\cot 2\theta}{1 - a\,\theta}\,d\,\theta - F \int \frac{\theta\cot 2\theta}{1 - a\,\theta}\,d\,\theta = \text{const} \tag{A.8}$$

The first and second integrals in equation A.8 can be solved exactly. The remaining four are not integrable exactly. Two solutions are used: by polynomial interpolation and by expansion in series.

Solution by polynomial interpolation

The first two integrals have exact solutions:

$$A \int \frac{d\,\theta}{(1 - a\,\theta)\,\theta} = - A \ln (1 - a\,\theta) + A \ln \theta$$

$$B \int \frac{d\,\theta}{1 - a\,\theta} = \frac{-B}{a} \ln (1 - a\,\theta)$$

The remaining four integrals are not soluble exactly. In order to integrate them, they are combined under one integral sign. The region of interest is $10^{\circ} < \theta < 80^{\circ}$, i.e. 10° away from the stagnation point and the edge of the hemisphere. Six points in this region are selected evenly spaced, the terminal ones being 10 and 80°. The values of the integrand are found for these points and a polynomial is found passing through these points thus approximating the integrand. Since a polynomial is always integrable, the solution can be found. Executing this procedure in steps one obtains:

$$C \int \frac{\cot \theta}{1 - a\,\theta}\, d\,\theta - D \int \frac{\theta \cot \theta}{1 - a\,\theta}\, d\,\theta + E \int \frac{\cot 2\theta}{1 - a\,\theta}\, d\,\theta +$$

$$- F \int \frac{\theta \cot 2\theta}{1 - a\,\theta}\, d\,\theta = \int (C \frac{\cot \theta}{1 - a\,\theta} - D \frac{\theta \cot \theta}{1 - a\,\theta} + E \frac{\cot 20}{1 - a\,\theta} +$$

$$- F \frac{\theta \cot 2\theta}{1 - a\,\theta}\Big) d\,\theta =$$

or for simplicity:

$$= \int (C\, g_1 - D\, g_2 + E\, g_3 - F\, g_4)\; d\,\theta$$

The following tabulation shows the values of the integrand at the selected six points:

θ	10	24	38	52	66	80	(degrees)
	.1745	.4189	.6632	.9076	1.152	1.396	(radians)

g_1 =	5.728	2.300	1.329	.8232	.476	.1913
g_2 =	.9995	.9635	.8814	.7471	.5484	.2671
g_3 =	2.775	.9221	.2590	-.2676	-.9626	-2.981
g_4 =	.4843	.3862	.17175	-.2384	-1.1088	-4.1622

Premultiplying and calling $f(\theta) = C\, g_1 - D\, g_2 + E\, g_3 - F\, g_4$

$C\, g_1$ =	.4260	.1710	.0989	.0612	.0354	.0142
$-D\, g_2$ =	-.0005	-.0005	-.0004	-.0004	-.0003	-.0001
$E\, g_3$ =	2.5685	.8535	.2397	-.2477	-.8910	-2.7592
$-F\, g_4$ =	-.0269	-.0215	-.0096	.0133	.0617	.2315
$f(\theta)$ =	2.9676	1.003	.329	-.1732	-.7939	-2.5135

It is obvious that the integral premultiplied by D contributes very little and therefore can be disregarded. Using Newton's interpolation method for finding the polynomial passing through these points, where, $\Delta\,\theta = 0.244346$:

2.97					
	-1.97				
1.0		1.3			
	- .67		-1.13		
.33		.17		.84	
	-.50		- .29		-1.53
- .17		-.12		-.69	
	-.62		- .98		
- .79		-1.1			
	-1.72				
-2.51					

$$f(\theta) = 2.97 - \frac{1.97}{.244346}(\theta - .1745) + \frac{1.3}{.2443^2 \times 2}(\theta - .1745)(\theta - .4189) +$$

$$- \frac{1.13}{.2443^3 \times 6}(\theta - .1745)(\theta - .4189)(\theta - .6632) +$$

$$+ \frac{.84}{.2443^4 \times 24}(\theta - .1745)(\theta - .4189)(\theta - .6632)(\theta - .9076) +$$

$$- \frac{1.53}{.2443^5 \times 120}(\theta - .1745)(\theta - .4189)(\theta - .6632)(\theta - .9076)(\theta - 1.152) =$$

$$= 6.98 - 33.79\theta + 76.90\theta^2 - 94.2\theta^3 + 58.36\theta^4 - 14.64\theta^5$$

For future use $f(\theta) = 0$ at $\theta \doteq 0.8195 = 46.95^\circ \doteq 47^\circ$

Taking the approximation

$$\int (Cg_1 + Eg_3 - Fg_4)\, d\theta \doteq \int f(\theta)\, d\theta =$$

$$\int (6.98 - 33.79\theta + 76.90\theta^2 - 94.2\theta^3 + 58.36\theta^4 - 14.64\theta^5)\, d\theta =$$

$$= 6.98\theta - 16.89\theta^2 + 25.63\theta^3 - 23.54\theta^4 + 11.67\theta^5 - 2.44\theta^6 = I(\theta)$$

Substituting the above integrals into equation A.8 yields:

$$\ln \bar{\bar{V}}_m - 0.537U \ln (1 - a\theta) + 0.5374 \ln \theta + 1.008 \ln (1 - a\theta) + {} + I(\theta) = \text{const} \tag{A.9}$$

Reducing

$$\ln \bar{\bar{V}}_m + 0.4708 \ln (1 - a\theta) + 0.5374 \ln \theta + I(\theta) = \text{const} \tag{A.10}$$

Applying boundary conditions:

$$\bar{\bar{V}}_m = 1 \text{ at } \theta = \theta_o = 10.9^\circ = 0.19$$

$$0.4708 \ln (1 - a\theta) + 0.5374 \ln \theta_o + I(\theta_o) = \text{const} \tag{A.11}$$

Substituting back into A.10:

$$\ln\left[\bar{\bar{V}}_m \left(\frac{1 - a\theta}{1 - a\theta_o}\right)^{.4708} \left(\frac{\theta}{\theta_o}\right)^{.5374}\right] + I(\theta) - I(\theta_o) = 0 \tag{A.12}$$

Finally, for $\theta \leq 47^\circ$:

$$\bar{\bar{V}}_m = \left(\frac{1 - a\theta_o}{1 - a\theta}\right)^{.4708} \left(\frac{\theta_o}{\theta}\right)^{.5374} e^{I(\theta_o) - I(\theta)} \tag{A.13a}$$

where:

$$I(\theta_o) - I(\theta) = -\Big[6.98\ (\theta-\theta_o) - 16.89\ (\theta^2-\theta_o^2) + 25.63\ (\theta^3-\theta_o^3) +$$

$$- 23.54\ (\theta^4-\theta_o^4) + 11.67\ (\theta^5-\theta_o^5) - 2.44\ (\theta^6-\theta_o^6)\Big]$$

And for $\theta > 47^\circ$:

$$\overline{V}_m = \overline{V}_{m47^\circ} \left(\frac{1 - a\theta_1}{1 - a\theta}\right)^{.4708} \left(\frac{\theta_1}{\theta}\right)^{.5374} e^{I(\theta) - I(\theta_1)} \qquad \text{(A.13b)}$$

where:

$\overline{V}_{m47^\circ} = \overline{V}_m$ at $\theta = 47^\circ \doteq .8195$ radians

In equation A.14, the symbol $\overline{V}_{m47}$ represents the value of $\overline{V}_m$ calculated at $\theta_1 = 47^\circ$, for which $f(\theta) = 0$. This equation is awkward to use. A much more manageable equation is obtained as follows:

Solution by expansion in series

The starting point is again equation A.8. The first two integrals have exact solution, but the remaining ones do not and an expansion in series will be used to solve them. Some terms in exact and series expansion will be similar. Collection of exact and rough coefficients by which integrals are multiplied produce incorrect results. In order to obtain consistent coefficients, all integrals are expanded in series.

The following series expansions will be used:

$$(1 - ax)^{-1} = 1 + ax + a^2x^2 + a^3x^3 + \ldots.$$

$$\cot x = \frac{1}{x} - \frac{x}{3} - \frac{x^3}{45} - \frac{2x^5}{945} - \ldots.$$

$$\cot 2x = \frac{1}{2x} - \frac{2x}{3} - \frac{8x^3}{45} - \frac{64x^5}{945} - \ldots$$

Using those, the component integrals become:

$$A\int \frac{d\theta}{(1 - a\theta)\theta} \doteq A\int \left(\frac{1}{\theta} + a + a^2\theta + a^3\theta^2 + \ldots\right) d\theta =$$

$$= A(\ln\theta + a\theta + \frac{a^2}{2}\theta^2 + \frac{a^3}{3}\theta^3 + \ldots)$$

Since a = 0.0561, the terms multiplied by powers of "a" larger than 2 will be disregarded, as will the integral premultiplied by D = 0.000472.

$$B\int \frac{d\theta}{1 - d\theta} \doteq B\int (1 + a\theta + a^2\theta^2 + \ldots)\, d\theta = B(\theta + \frac{a}{2}\theta^2 + \frac{a^2}{3}\theta^3)$$

$$C\int \frac{\cot\theta}{1 - a\theta}\, d\theta \doteq C\int (1 + a\theta + a^2\theta^2)\left(\frac{1}{\theta} - \frac{\theta}{3} - \frac{\theta^3}{45} \ \ldots\right) d\theta =$$

$$= C\left[\ln\theta + a\theta + \frac{1}{2}(a^2 - \frac{1}{3})\theta^2 - \frac{a}{g}\theta^3 - \frac{1}{4}(\frac{a^2}{3} + \frac{1}{45})\theta^4 - \frac{a}{5x45}\theta^5\right]$$

$$E\int \frac{\cot 2\theta}{1 - a\theta}\, d\theta \doteq E\int (1 + a\theta + a^2\theta^2)\left(\frac{1}{2\theta} - \frac{2\theta}{3} - \frac{8\theta^3}{45} \ldots\right) d\theta =$$

$$= E\left[\frac{1}{2}\ln\theta + \frac{a}{2}\theta + \frac{1}{2}\left(\frac{a^2}{2} - \frac{2}{3}\right)\theta^2 - \frac{2a}{g}\theta^3 - \frac{1}{4}\left(\frac{8}{45} + \frac{2a^2}{3}\right)\theta^4 - \frac{8a}{5\text{x}45}\theta^5\right]$$

$$F\int \frac{\theta\cot 2\theta}{1 - a\theta}\,d\theta \doteq F\int (\theta + a\theta^2 + a^2\theta^3)\left(\frac{1}{2\theta} - \frac{2\theta}{3} - \frac{8\theta^3}{45} \quad \ldots\right) d\theta =$$

$$= F\left[\frac{1}{2}\theta + \frac{a}{4}\theta^2 + \frac{1}{3}\left(\frac{a^2}{2} - \frac{2}{3}\right)\theta^3 - \frac{a}{6}\theta^4 - \frac{1}{5}\left(\frac{8}{45} + \frac{2a^2}{3}\right)0-^{5} - \frac{8a}{6\text{x}45}\theta^6\right]$$

Substituting these components back into equation A.8 one obtains:

$$\ln V_m + a\ln\theta + A\,a\theta + \frac{1}{2}a^2\theta^2 - B\theta - \frac{1}{2}a\,B\theta^2 - \frac{1}{3}a^2\,B\theta^3 + C\ln\theta +$$

$$+ a\,C\theta + \frac{1}{2}C\left(a^2 - \frac{1}{3}\right)\theta^2 - \frac{1}{9}a\,C\theta^3 - \frac{1}{4}C\left(\frac{a^2}{3} + \frac{1}{45}\right)\theta^4 +$$

$$+ \frac{1}{2}E\ln\theta + \frac{1}{2}a\,E\theta + \frac{1}{2}E\left(\frac{a^2}{2} - \frac{2}{3}\right)\theta^2 - \frac{2}{9}\,a\,E\theta^3 +$$

$$- \frac{1}{4}E\left(\frac{8}{45} + \frac{2a^2}{3}\right)\theta^4 - \frac{1}{2}F\theta - \frac{1}{4}a\,F\theta^2 - \frac{1}{3}F\left(\frac{a^2}{2} - \frac{2}{3}\right)\theta^3 +$$

$$+ \frac{1}{6}a\,F\theta^4 + \frac{1}{5}\left(\frac{8}{45} + \frac{2a^2}{3}\right)\theta^5 = \text{const} \tag{A.14}$$

collecting terms:

$$\ln\bar{V}_m + \left(A + C + \frac{1}{2}F\right)\ln\theta + \left(aA - B + aC + \frac{1}{2}aE\right)\theta +$$

$$+ \left(\frac{1}{2}a^2A - \frac{1}{2}aB + \frac{1}{2}a^2C - \frac{1}{6}C + \frac{1}{4}a^2E - \frac{1}{3}E - \frac{1}{4}a\,F\right)\theta^2 +$$

$$+ \left(- \frac{1}{3} a^2 B - \frac{1}{9} aC - \frac{2}{9} aE - \frac{1}{6} a^2 F + \frac{2}{9} F\right) \theta^3 +$$

$$+ \left(- \frac{1}{12} a^2 C - \frac{1}{180} C - \frac{2}{45} E - \frac{1}{6} a^2 E + \frac{1}{6} aF\right) \theta^4 +$$

$$+ \left(\frac{8F}{225} + \frac{2a^2 F}{15}\right) \theta^5 = \text{const} \qquad (A.15)$$

After substitution of values:

$$\ln \bar{V}_m + 1.07457 \ln\theta + 0.003723\, \theta - 0.3216\, \theta^2 + 0.0002688\, \theta^3 +$$

$$- 0.04154\, \theta^4 + 0.002001\, \theta^5 = \text{const} \qquad (A.16)$$

Disregarding the terms with negligibly small coefficients:

$$\ln \bar{V}_m + 1.075 \ln\theta - 0.3216\, \theta^2 - 0.04154\, \theta^4 \doteq \text{const} \qquad (A.17)$$

Applying boundary conditions that $V_m = 1$ at $\theta = \theta_o$ and rearranging:

$$\ln \left[\bar{V}_m \left(\frac{\theta}{\theta_o}\right)^{1.075} \right] = 0.3216\, (\theta^2 - \theta_o^2) + 0.04154\, (\theta^4 - \theta_o^4) \qquad (A.18)$$

And finally:

$$\bar{V}_m = \left(\frac{\theta_o}{\theta}\right)^{1.075} e^{0.3216\,(\theta^2-\theta_o^2) + 0.04154\,(\theta^4-\theta_o^4)} \tag{A.19}$$

The derivative of A.19 equals zero for $\theta_2 \doteq 64.3^\circ = 1.1228$ radians. Therefore, for $\theta \leq \theta_2 = 64.3^\circ$ the following relation applies:

$$\bar{V}_m = \left(\frac{\theta_o}{\theta}\right)^{1.075} e^{0.3216\,(\theta^2-\theta_o^2) + 0.04154\,(\theta^4-\theta_o^4)} \tag{A.20a}$$

And for $\theta > \theta_2$:

$$\bar{V}_m = \bar{V}_{m64.3^\circ} \left(\frac{\theta_o}{\theta}\right)^{1.075} e^{0.3216\,(\theta_2^2-\theta^2) + 0.04154\,(\theta_2^4-\theta^4)} \tag{A.20b}$$

In equation A.20b, the symbol $\bar{V}_{m64.3^\circ}$ denotes the value of $\bar{V}_m$ at $\theta = \theta_2 \doteq 64.3^\circ = 1.1228$ radians.

Finally, it would be of interest to obtain an equation similar to 8.3a. For that purpose, at $\theta_o = 10.9^\circ = 0.19$ radians that equation should equal 1, therefore

$$C_1 = 1$$

and the purely empirical equation found is:

$$V_m = \frac{1}{5.287\,\theta\cos\frac{\theta}{2}} = \left(5.287\,\theta\cos\frac{\theta}{2}\right)^{-1} \tag{A.21}$$

APPENDIX B

Calculation of Viscous Shear Force at the Wall, for Chapter 9

The momentum equation component is in the plane normal to the impinging jet. In a consideration similar to that in chapter 8, but for an angular element $d\varphi$ of the control volume ADEA, at the wall, as shown in Figure 7a, the following equation applies:

$$\int_{s_o}^{s} \rho V_m \cos\theta \frac{\partial}{\partial l}\left[\int_{0}^{\delta} V (R - z) \sin\theta \, dz\right] dl +$$

$$- \int_{0}^{\delta} \rho V^2 (R - z) \cos\theta \sin\theta \, dz =$$

$$= \int_{s_o}^{s} R \sin\theta \, \tau_w \cos\theta \, ds \qquad (B.1)$$

Where:	V_m	is the max. velocity, i.e. velocity at $z = \delta$
	V	is a velocity at z in the velocity profile
	θ	is the position angle in vertical plane
	R	is the radius of curvature of the hemispherical plate
	l	is the curvilinear distance measured along the surface of integration
	s	is the distance along rhe hemispherical surface
		is the air density
	τ_w	is the wall shear stress
	φ	is the angle in the plane normal to the free jet axis

Since the boundary layer thickness is small, one can approximate $1 \doteq s = R\,\theta$. Assuming ρ = constant and introducing a dummy variable α for θ

$$\rho \int_{\theta_o}^{\theta} V_m \cos\alpha \frac{\partial}{R\,\partial\alpha}\left[\int_0^{\delta} V\,(R - z)\sin\alpha\,dz\right] R\,d\alpha \; +$$

$$-\rho \int_0^{\delta} V^2 (R - z)\cos\alpha\,\sin\alpha\,dz = \int_{\theta_o}^{\theta} \tau_w R^2 \cos\alpha\,\sin\alpha\,d\alpha \qquad (B.2)$$

Differentiating each term in equation B.2 with respect to α, observing that $V = V_m$ at $z = \delta$ and returning back from α to θ one obtains:

$$V_m\,\rho\cos\theta \int_0^{\delta} (R - z)\,\frac{\partial}{\partial\theta}(V\sin\theta)\,dz \; +$$

$$+\rho\,(R - \delta)\,V_m^2 \cos\theta\,\sin\theta\,\frac{\partial\delta}{\partial\theta} - \rho\int_0^{\delta}(R-z)\,\frac{\partial}{\partial\theta}(V^2\cos\theta\,\sin\theta)\,dz +$$

$$-\rho\,(R - \delta)\,V_m^2\cos\theta\,\sin\theta\,\frac{\partial\delta}{\partial\theta} = \tau_w R^2 \cos\theta\,\sin\theta \qquad (B.3)$$

Since the second and fourth terms cancel, it reduces to:

$$V_m\,\rho\cos\theta\int_0^{\delta}(R - z)\,\frac{\partial}{\partial\theta}(V\sin\theta)\,dz \; +$$

$$- \rho \int_0^{\delta} (R - z) \frac{\partial}{\partial \theta} (V^2 \cos \theta \sin \theta) \, dz = \tau_w R^2 \cos \theta \sin \theta$$

(B.3a)

Introducing dimensionless parameters:

$$\bar{V} = \frac{V}{U_{oc}} \quad ; \quad \bar{V}_m = \frac{V_m}{U_{oc}} \quad ; \quad \bar{z} = \frac{z}{\delta} \quad \text{and } d\bar{z} = \frac{dz}{\delta}$$

Dividing by $U_{oc}{}^2$:

$$\frac{V_m}{U_{oc}} \rho \delta \cos \theta \int_0^{\delta} (R - z) \frac{\partial}{\partial \theta} \left(\frac{V}{U_{oc}} \sin \theta\right) \frac{dz}{\delta} +$$

$$- \rho \delta \int_0^{\delta} (R - z) \frac{\partial}{\partial \theta} \left(\frac{V^2}{U_{oc}{}^2} \cos \theta \sin \theta\right) \frac{dz}{\delta} =$$

$$= \frac{\tau_w R^2}{U_{oc}^2} \cos \theta \sin \theta$$

(B.4)

Introducing the new symbols and dividing by ρ :

$$\bar{V}_m \delta \cos \theta \int_0^1 (R - \delta \bar{z}) \frac{\partial}{\partial \theta} (\bar{V} \sin \theta) \, d\bar{z} +$$

$$- \delta \int_0^1 (R - \delta \bar{z}) \frac{\partial}{\partial \theta} (\bar{V}^2 \cos \theta \sin \theta) d\bar{z} = \frac{\tau_w R^2}{\rho U_{oc}^2} \cos \theta \sin \theta$$

(B.5)

Using the identity $\sin 2\theta = 2 \cos \theta \sin \theta$, the last equation becomes:

$$\bar{V}_m \, \delta \, \cos \theta \int_0^1 (R - \delta \, \bar{z}) \frac{\partial}{\partial \theta} (\bar{V} \sin \theta) \, d\bar{z} \, +$$

$$- \, \delta \int_0^1 (R - \delta \, \bar{z}) \frac{\partial}{\partial \theta} (\bar{V}^2 \tfrac{1}{2} \sin 2\theta) d\bar{z} = \frac{\tau_w \, R^2}{\rho \, U_{oc}^2} \, \tfrac{1}{2} \sin 2\theta \qquad \text{(B.5a)}$$

Carrying out the differentiation and multiplying by two:

$$2 \, \bar{V}_m \, \delta \, \cos \theta \int_0^1 (R - \delta \, \bar{z}) \left[\bar{V}' \sin \theta + \bar{V} \cos \theta \right] d\bar{z} \, +$$

$$-2 \, \delta \int_0^1 (R - \delta \, \bar{z}) \left[\bar{V}\bar{V}' \sin 2\theta + \bar{V}^2 \cos 2\theta \right] d\bar{z} =$$

$$= \frac{\tau_w \, R^2}{\rho \, U_{oc}^2} \sin 2\theta \qquad \text{(B.6)}$$

and multiplying out the terms, yields:

$$2 \, \bar{V}_m \, \delta \, \cos \theta \int_0^1 (R\bar{V}' \sin \theta + R\bar{V} \cos \theta - \delta \, \bar{V}' \, \bar{z} \sin \theta \, +$$

$$- \, \delta \, \bar{V} \, \bar{z} \cos \theta) d\bar{z} - 2 \, \delta \int_0^1 (R\bar{V} \, \bar{V}' \sin 2\theta + R\bar{V}^2 \cos 2\theta \, +$$

$$- \, \delta \, \bar{V} \, \bar{V}' \, \bar{z} \sin 2\theta - \delta \, \bar{V}^2 \bar{z} \cos 2\theta) \, d\bar{z} = \frac{\tau_w \, R^2}{\rho \, U_{oc}^2} \sin 2\theta \qquad \text{(B.7)}$$

Within the boundary layer region the velocity distribution may be assumed as before:

$$\bar{V} = \bar{V}_m \bar{z}^{1/n} \qquad (8.15)$$

and $$\frac{\partial \bar{V}}{\partial \theta} = \bar{z}^{1/n} \left(\bar{V}_m' - 1/n\, \bar{V}_m \frac{\delta'}{\delta}\right) \qquad (8.19)$$

Introducing 8.15 and 8.17 into B.7 yields:

$$2\bar{V}_m\, \delta \cos\theta \int_0^1 \Big[R\bar{z}^{1/n} \left(\bar{V}_m' - 1/n\, \bar{V}_m \frac{\delta'}{\delta}\right) \sin\theta + R\, \bar{V}_m\, \bar{z}^{1/n} \cos\theta +$$

$$- \delta\, \bar{z}^{\frac{n+1}{n}} \left(\bar{V}_m' - 1/n\, \bar{V}_m \frac{\delta'}{\delta}\right) \sin\theta - \delta\, \bar{V}_m\, \bar{z}^{\frac{n+1}{n}} \cos\theta \Big] d\bar{z} +$$

$$- 2\,\delta \int_0^1 \Big[R\bar{V}_m \bar{z}^{2/n} \left(\bar{V}_m' - 1/n\, \bar{V}_m \frac{\delta'}{\delta}\right) \sin 2\theta + R\bar{V}_m^2 \bar{z}^{2/n} \cos 2\theta +$$

$$- \delta\, \bar{V}_m\, \bar{z}^{\frac{n+2}{n}} \left(\bar{V}_m' - 1/n\, \bar{V}_m \frac{\delta'}{\delta}\right) \sin 2\theta - \delta\, \bar{V}_m^2 \bar{z}^{\frac{n+2}{n}} \cos 2\theta \Big] d\bar{z} =$$

$$= \frac{\tau_w R^2}{\rho\, U_{oc}^2} \sin 2\theta \qquad (B.8)$$

On carrying out the integration, there results

$$2\,\bar{V}_m\,\delta\,\cos\theta\,\Big[\,R\,(\bar{V}'_m - 1/n\,\bar{V}_m\,\frac{\delta'}{\delta})\,\sin\theta\,\frac{\bar{z}^{\frac{n+1}{n}}}{\frac{n+1}{n}}\Big|_0^1 +$$

$$+\,R\bar{V}_m\,\cos\theta\,\frac{\bar{z}^{\frac{n+1}{n}}}{\frac{n+1}{n}}\Big|_0^1 \quad -\,\delta\,(\bar{V}'_m - 1/n\,\bar{V}_m\,\frac{\delta'}{\delta})\,\sin\,\frac{\bar{z}^{\frac{2n+1}{n}}}{\frac{2n+1}{n}}\Big|_0^1 \quad +$$

$$-\,\delta\,\bar{V}_m\,\cos\theta\,\frac{\bar{z}^{\frac{2n+1}{n}}}{\frac{2n+1}{n}}\Big|_0^1\Big] - 2\,\delta\,\Big[R\bar{V}_m\,(\bar{V}'_m - 1/n\,\bar{V}_m\,\frac{\delta'}{\delta})\,\sin 2\theta\,\frac{\bar{z}^{\frac{n+2}{n}}}{\frac{n+2}{n}}\Big|_0^1 +$$

$$+\,R\bar{V}_m^{\,2}\,\cos 2\theta\,\frac{\bar{z}^{\frac{n+2}{n}}}{\frac{n+2}{n}}\Big|_0^1 \quad -\,\delta\,\bar{V}_m\,(\bar{V}_m{}' - 1/n\,\bar{V}_m\,\frac{\delta'}{\delta})\,\sin 2\theta\,\frac{\bar{z}^{\frac{2n+2}{n}}}{\frac{2n+2}{n}}\Big|_0^1 \quad +$$

$$-\,\delta\,\bar{V}_m^{\,2}\,\cos 2\theta\,\frac{\bar{z}^{\frac{2n+2}{n}}}{\frac{2n+2}{n}}\Big|_0^1\Big] \quad = \quad \frac{\tau_w\,R^2}{\rho\,U_{oc}^2}\,\sin 2\theta \qquad (B.9)$$

On substituting the limits and dividing by sin 2θ, $\theta \neq 0$, i.e. away from stagnation point, one gets

$$\frac{2\,\cos\theta}{2\,\cos\theta\,\sin\theta}\,\bar{V}_m\,\delta\,\Big[\frac{n}{n+1}\,R\,(\bar{V}'_m - 1/n\,\bar{V}_m\,\frac{\delta'}{\delta})\,\sin\theta + \frac{2n}{n+1}\,R\,\bar{V}_m\,\cos\theta\,+$$

$$-\,\frac{n}{2n+1}\,\delta\,(\bar{V}_m{}' - 1/n\,\bar{V}_m\,\frac{\delta'}{\delta})\sin\theta - \frac{2n}{2n+1}\,\delta\,\bar{V}_m\,\cos\theta\,\Big]\,+$$

$$- 2\,\delta \left[\frac{n}{n+2} R\, \bar{V}_m \left(\bar{V}_m{}' - 1/n\, \bar{V}_m \frac{\delta'}{\delta}\right) + \frac{n}{n+2} R\, \bar{V}_m{}^2 \cot 2\theta + \right.$$

$$\left. - \frac{n}{2n+2}\, \delta\, \bar{V}_m \left(\bar{V}_m{}' - 1/n\, \bar{V}_m \frac{\delta'}{\delta}\right) - \frac{n}{2n+2}\, \delta\, \bar{V}_m{}^2 \cot 2\theta \right] =$$

$$= \frac{\tau_{w} R^2}{\rho\, U_{oc}{}^2} \qquad (B.10)$$

Multiplying and reducing terms

$$\frac{n}{n+1} R\, \delta\, \bar{V}_m \bar{V}_m{}' - \frac{1}{n+1} R\, \delta'\, \bar{V}_m{}^2 + \frac{n}{n+1} R\, \delta\, \bar{V}_m{}^2 \cot \theta +$$

$$- \frac{n}{2n+1}\, \delta^2\, \bar{V}_m \bar{V}_m{}' + \frac{1}{2n+1}\, \delta\, \delta'\, \bar{V}_m{}^2 - \frac{n}{2n+1}\, \delta^2\, \bar{V}_m{}^2 \cot \theta +$$

$$- \frac{2n}{n+2} R\, \delta\, \bar{V}_m \bar{V}_m{}' + \frac{2}{n+2} R\, \delta'\, \bar{V}_m{}^2 - \frac{2n}{n+2} R\, \delta\, \bar{V}_m{}^2 \cot 2\theta +$$

$$+ \frac{n}{n+1}\, \delta^2\, \bar{V}_m \bar{V}_m{}' - \frac{1}{n+1}\, \delta\, \delta'\, \bar{V}_m{}^2 + \frac{n}{n+1}\, \delta^2\, \bar{V}_m{}^2 \cot 2\theta =$$

$$= \frac{\tau_{w} R^2}{\rho\, U_{oc}{}^2} \qquad (B.11)$$

Which, after a few transformations, becomes

$$\left(\frac{n}{n+1} - \frac{2n}{n+2}\right) R \, \delta \, \bar{V}_m \bar{V}_m{}' + \left(\frac{n}{n+1} - \frac{n}{2n+1}\right) \delta^2 \bar{V}_m \bar{V}_m{}' +$$

$$+ \left(\frac{2}{n+2} - \frac{1}{n+1}\right) R \, \delta' \, \bar{V}_m{}^2 + R \, \delta \, \bar{V}_m^2 \left(\frac{n}{n+1} \cot \theta - \frac{2n}{n+2} \cot 2\theta\right)$$

$$+ \left(\frac{1}{2n+1} - \frac{1}{n+1}\right) \delta \, \delta' \, \bar{V}_m{}^2 + \delta^2 \, \bar{V}_m^2 \left(\frac{n}{n+1} \cot 2\theta - \frac{n}{2n+1} \cot \theta\right)$$

$$= \frac{\tau_w R^2}{\rho \, U_{oc}{}^2} \qquad (\ .12)$$

Multiplication of coefficients yields:

$$\frac{-n^2}{(n+1)\,(n+2)} R \, \delta \, \bar{V}_m \bar{V}_m{}' + \frac{n^2}{(n+1)\,(2n+1)} \delta^2 \bar{V}_m \bar{V}_m{}' +$$

$$+ \frac{n}{(n+1)\,(n+2)} R \, \delta' \, \bar{V}_m{}^2 + R \, \delta \, \bar{V}_m^2 \left(\frac{n}{n+1} \cot \theta - \frac{2n}{n+2} \cot 2\theta\right) +$$

$$- \frac{n}{(n+1)\,(2n+1)} \delta \delta' \, \bar{V}_m{}^2 - \delta^2 \, \bar{V}_m^2 \left(\frac{n}{n+1} \cot 2\theta - \frac{n}{2n+1} \cot \theta\right) =$$

$$= \frac{\tau_w R^2}{\rho \, U_{oc}{}^2} \qquad (B.12a)$$

If $\overline{V}_m$ is assumed to have the following dimensionless form

$$\overline{V}_m = A \left(\frac{\theta}{\theta_o}\right)^{-\alpha} \tag{B.13}$$

where A is a velocity proportionality coefficient

$$\frac{d\,V_m}{d\,\theta} = -\alpha A \left(\frac{\theta}{\theta_o}\right)^{-(\alpha+1)} \frac{1}{\theta_o} \tag{B.14}$$

And also if it is assumed that

$$\delta = BR\theta \tag{B.15}$$

where B is a coefficient of the boundary layer growth.

$$\frac{d\,\delta}{d\,\theta} = BR \tag{B.16}$$

After substituting the last four relations into equation B.12:

$$\frac{n^2 \alpha}{(n+1)\,(n+2)} R^2 A^2 B \left(\frac{\theta}{\theta_o}\right)^{-2\alpha} - \frac{n^2 \alpha}{(n+1)\,(2n+1)} R^2 A^2 B^2 \theta \left(\frac{\theta}{\theta_o}\right)^{-2\alpha} +$$

$$+ \frac{n}{(n+1)\,(n+2)} R^2 A^2 B\left(\frac{\theta}{\theta_o}\right)^{-2\alpha} + R^2 A^2 B\,\theta \left(\frac{\theta}{\theta_o}\right)^{-2\alpha} \left(\frac{n}{n+1} \cot \theta \right. +$$

$$\left. - \frac{2n}{n+2} \cot 2\theta\right) +$$

$$- \frac{n}{(n+1)(2n+1)} R^2 A^2 B^2 \theta \left(\frac{\theta}{\theta_o}\right)^{-2\alpha} - R^2 A^2 B^2 \theta^2 \left(\frac{\theta}{\theta_o}\right)^{-2\alpha} \left(\frac{n}{n+1} \cot 2\theta + \right.$$

$$\left. - \frac{n}{2n+1} \cot \theta\right) = \frac{\tau_w R^2}{\rho U_{oc}^2} \qquad (B.17)$$

Observing that B is a small number, about 1/80 in the present investigation, one can disregard terms in which B^2 appears. Without committing large error one can write, therefore after dividing by R^2:

$$\frac{\tau_w}{\rho U_{oc}^2} \doteq \frac{n^2 \alpha}{(n+1)(n+2)} A^2 B \left(\frac{\theta}{\theta_o}\right)^{-2\alpha} + \frac{n}{(n+1)(n+2)} A^2 B \left(\frac{\theta}{\theta_o}\right)^{-2\alpha} +$$

$$+ A^2 B \theta \left(\frac{\theta}{\theta_o}\right)^{-2\alpha} \left(\frac{n}{n+1} \cot \theta - \frac{n}{n+2} 2 \cot 2\theta\right) \qquad (B.18)$$

After reducing:

$$\frac{\tau_w}{\rho U_{oc}^2} \doteq \frac{n^2 \alpha + n}{(n+1)(n+2)} A^2 B \left(\frac{\theta}{\theta_o}\right)^{-2\alpha} + \left(\frac{n}{n+1} \theta \cot \theta + \right.$$

$$\left. - \frac{n}{n+2} 2\theta \cot 2\theta\right) A^2 B \left(\frac{\theta}{\theta_o}\right)^{-2\alpha} \qquad (B.18a)$$

For simplicity let:

$$F = A^2 B \quad \frac{n^2 \alpha + n}{(n+1)(n+2)} + \frac{n}{n+1} \theta \cot \theta - \frac{n}{n+2} 2\theta \cot 2\theta$$

(B.19)

Then B.18a becomes

$$\frac{\tau_w}{\rho U_{oc}^2} = F\left(\frac{\theta}{\theta_o}\right)^{-2\alpha} \qquad (B.18b)$$

APPENDIX C

Evaluation of Experimental Error

The maximum relative error for velocity, measured with the Pitot tube at steady, incompressible flow is evaluated as follows:

The velocity formula is:

$$V = \sqrt{2gh\ (\rho w/\rho a - 1)} \qquad (C\text{-}1)$$

in which $$\rho a = \frac{144\ P}{Z\ R\ T} \qquad (C\text{-}2)$$

Where: g = gravity acceleration, ft/s^2

h = water column reading, inches of water

ρ_w = density of water, lb_m/ft^3

ρa = density of air, lb_m/ft^3

P = ambient pressure, psia

Z = compressibility factor

R = air constant = $lb_f\ ft/lb_m\ {}^oF$

T = air temperature, ^oR

On substituting C-2 into C-1, one obtains:

$$V \doteq \sqrt{\frac{2gh\ ZRT\rho w}{144\ P}} \qquad (C\text{-}3)$$

By definition, a maximum relative error is:

$$\delta = \frac{\text{Max. measurement error}}{\text{Measured value}}\ 100\% \qquad (C\text{-}4)$$

Since g, Z and R may be assumed exact, they do not contribute to the error and it is expressed by:

$$\delta_v = \tfrac{1}{2}\,(\,\delta_\rho + \delta_T + \delta_h + \delta_p) \qquad (C.5)$$

Evaluating individual relative errors:

Water density error between 75 and 90°F

$$\delta_\rho = \frac{62.27 - 62.12}{62.12} = \frac{0.15}{62.12} = 0.24\%$$

Temperature error, 2°F at an average of 75°F

$$\delta_T = \frac{2}{535} = 0.4\%$$

U-tube water column reading, 0.1"

$$\delta_h = \frac{0.1}{22.7} = 0.4\%$$

at the velocity = 320 ft/sec, measured with the U-tube

Barometric pressure, 0.03" Hg

$$\delta_p = \frac{0.03}{30} = 0.1\%$$

Combining the components yields:

$$\delta_v = \tfrac{1}{2}\,(0.2 + 0.4 + 0.4 + 0.1) = \tfrac{1}{2}\,(1.1) \doteq 0.6\% \qquad (C.6)$$

The maximum relative error at steady flow and the velocity of 320 ft/sec measured with a U-tube is 0.6%.

Compressible Flow

Air compressibility effects are most prominent at the highest velocity. The highest velocity measured in the wall jet was 320 ft/sec which corresponds to Mach number $M = 0.28$.

The Pitot tube pressure reading has to be corrected according to the relation (30):

$$\frac{p}{p_o} = \left(1 - \frac{k-1}{2} M^2\right)^{\frac{k}{k-1}} \tag{C.7}$$

Expanding C.7 by binomial theorem and rearranging yields:

$$\frac{p_o - p}{\frac{1}{2} \quad {}_o V^2} = 1 - \frac{1}{4} M^2 + \ldots\ldots \tag{C.8}$$

After disregarding smaller terms, $\frac{1}{4} M^2$ is the correction for compressibility and also the relative error incurred by assuming an incompressible flow:

$$\delta_c = \frac{1}{4} M^2 = \frac{1}{4} (0.28)^2 \doteq 0.02 = 2\% \tag{C.9}$$

The total maximum error with compressibility effects included is then:

$$\delta_{vc} = \frac{1}{2} (0.2 + 0.4 + 0.4 + 0.1 + 2) \doteq 1.6\% \tag{C.10}$$

Since compressibility error is the dominant component and it is proportional to velocity squared, the total relative error decreases rapidly with decreasing velocity.

BIBLIOGRAPHY

1. Abramovich, Genrikh, N., *The Theory of Turbulent Jets*, MIT Press, 1963.

2. Albertson, M. L., Dai, Y. B., Jensen, R. A., Rouse, H., *Diffusion of Submerged Jets*, ASCE Trans. Vol. 115, 1950, pp. 639-697.

3. Bakke, P., *An Experimental Investigation of a Wall Jet*, J. of Fluid Mech., Vol. 12, 1957.

4. Barat, M., *Variations de pression statique dans un jet libre subsonique*, Mecanique de fluides. Comptes rendus, Seance du 25 Janvier 1954, pp. 445-447.

5. Becker, H. A., Brown, A. P. G., *Response of Pitot Probes in Turbulent Streams*, J. of Fluid Mech. (1974), Vol. 62, Part 1, pp. 85-114.

6. Beltaos, S., Rajaratnam, N., *Plane Turbulent Impinging Jets*, Journal of Hydr. Res. 11 (1) pp. 29-59, 1973.

7. Bradshaw, P. and Gee, M. T., *Turbulent Wall Jets with and Without an External Stream*, Aeronaut. Res. Council R and M 3252, 1962.

8. Dyban, Y. P. and Mazur, A. I., *Heat Transfer From a Flat Air Jet Flowing Into a Concave Surface*, Heat Transfer-Soviet Research, Vol. 2, No. 3, May 1970, p. 19.

9. Era, Y., Saima, A., *An Investigation of Impinging Jet*, Bulletin of JSME, Vol. 19, No. 113, July 1976, pp. 800-807.

10. Froessling N. *Verdunstung, Warmeübertragung und Geschwindigkeitverteilung bei zweidimensionaler and rotationsymmetrischer laminarer Grenzschichtströmung, Lunds*. Univ. Arsskr. N.F. Avd. 2, 35 No. 4, 1940.

11. Glauert, M. B., *The Wall Jet*, J. of Fluid Mech., Vol. 1, 1957, pp. 625-643.

12. Gooderum, P. B., Wood, G. P. and Brevoort, M. J., *Investigation With An Interferometer of the Turbulent Mixing of a Free Supersonic Jet*, NACA Rep. 963, 1950.

13. Görtler, H., *Berechnung von Aufgaben der freien Turbulenz auf Grund eines neuen Näherungsansatzes*, ZAMM, 22, 1942, pp. 244-254.

14. Homann F. Der Einfluss grosser Zähigkeit bei der Strömung un den Zylinder und um die Kugel. ZAMM, 16 153-164 (1936) and Forschg. Ing.-Wes. 7, 1-10 (1936).

15. Hrycak, P., Heat Transfer From Impinging Jets, A Literature Review, Report under Grant NGR-31-009-004, N.C.E., August 1968.

16. Hrycak, P., Jachna, S. and Lee, D. T., A Study of Characteristics of Developing, Incompressible, Axi-symmetric Jets. Letters in Heat and Mass Transfer, Vol. I, 1974, pp. 63-72.

17. Hrycak, P., Jachna, S., Environmental Impact of Submerged Turbulent Plumes. Proceedings - Institute of Environmental Sciences, pp. 538-542, 1976.

18. Hrycak, P., Lee, D. T., Calculation of Maximum Velocity Decay in Wall Jets, Journal of Spacecraft and Rockets, Vol. 7, No. 5, May 1970, pp. 623-625.

19. Hrycak, P., Lee, D. T., Gauntner, J. W. and Livingood, J. N. B., Experimental Flow Characteristics of a Single Turbulent Jet Impinging on a Flat Plate, NASA TND-5690, March 1970.

20. Hrycak, P., Nagarajan, R., Lee, D. T., Summary Report on Hemispherical Surface Flow and Heat Transfer Tests, Unpublished Report, NASA NAS 3-11175, September 1970.

21. Jones, W. P., Launder, B. E., The Calculation of Low-Reynolds-Number Phenomena with a Two-Equation Model of Turbulence, Int. J. Heat Mass Transfer, Vol. 16, pp. 1119-1130, Pergamon Press, 1973.

22. Karman, Th. von, On Laminar and Turbulent Friction, ZAMM 1, 233-252 (1921); NACA TM 1092 (1946).

23. Kim, T. S., Analysis of Flow Characteristics in Circular, Submerged, Impinging Jets, Dissertation, Illinois Institute of Technology, 1967.

24. Krishnan, S., Glicksman, L. R., A Two Dimensional Analysis of a Heated Free Jet at Low Reynolds Numbers, ASME paper 70-WA/FE-3.

25. Lee, David T. H., Experimental Investigation of Submerged Incompressible Turbulent Impinging Jets, M. S. Thesis, N.C.E., 1969.

26. Lighthill, M. J., Contributions to the Theory of the Pitot-Tube Displacement Effect, J. of Fluid Mech. (1957) Vol. 2, pp. 493-512.

27. Maxwell, W. H. C., Flux Development Region in Submerged Jets, Journal of Eng. Mech. Div. ASCE Proc., Dec. 1970, pp. 1061-1079.

28. Miller, D. R. and Comings, E. W., Static Pressure Distribution in a Free Turbulent Jet, J. Fluid Mech., Vol. 3, Oct. 1957.

29. Narain, J. P., Swirling Shallow Submerged Turbulent Plumes, Journal of the Hydr. Division, September, 1974, pp. 1229-1243, HY 9.

30. Narain, J. P., Momentum Flux Development from Three-Dimensional Free Jets, Transactions of ASME, J. of Fluid Eng. Paper No. 76-FE-E.

31. Poreh, M. and Cermak, J. E., Flow Characteristics of a Circular Submerged Jet Impinging Normally on a Smooth Boundary, Proc. 6th Midw. Conf. on Fluid Mech. Univ. of Texas, 1959, pp. 198-212.

32. Poreh, M., Tsuei, Y. G., and Cermak, J. E., Investigation of a Turbulent Jet, ASME Paper No. 67-APM-10, 1967.

33. Prandtl, L., Tietjens, O. G., Applied Hydro- and Aeromechanics, Dover Publications, In., N.Y. 1957, p. 227.

34. Reichardt, H.,Gesetzmässigkeiten der freien Turbulenz VDI - Forschunsheft 414, 1942.

35. Reid, K. N., Katz, S., Characterization of Free and Impinging Jets With and Without Auxiliary Flows, ASME paper 70-WA/Flcs.-6.1

36. Reynolds, A. J., The Variation of Turbulent Prandtl and Schmidt Numbers in Wakes and Jets, Int. J. Heat Mass Transfer, Vol. 19, pp. 757-764, Pergamon Press, 1976.

37. Russell, P. J., Hatton, A. P., Turbulent Flow Characteristics of an Impinging Jet, Proc. Instn. Mech. Eng. 186, 52/72 pp. 635-644 (1972).

38. Sami, S., The Pitot Tube in Turbulent Shear Flow, Proceedings of the 11th Midwestern Mechanics Conference, Vol. 5, Developments in Mechanics, pp. 191-200, (1969); Published by Iowa State University Press.

39. Schapiro, A., The Dynamic and Thermodynamics of Compressible Fluid Flow, Vol. I, 1973, p. 87.

40. Schlichting, H., Über das ebene Windschatten Problem, Thesis, Gottingen, 1930, Ing. Arch. 1, pp. 533-571 (1930).

41. Schlichting, H., Boundary Layer Theory, 4th ed., McGraw-Hill Co., NY, 1960.

42. Schnurr, N. M., Williamson, J. W., Tatom, J. W., An Analytical Investigation of the Impingement of Jets on Curved Deflectors, AIAA Journal, Vol. 10, No. 11 pp. 1430-35, 1972.

43. Snedeker, R. S. and Donaldson, C. du P., Experiments on Free and Impinging Under-Expanded Jets from a Convergent Nozzle, Aeronautical Research Associates of Princeton, Inc., Princeton, NJ AD461 622, 1964.

44. Strand, T., On the Theory of Normal Ground Impingement of Axisymmetric Jets in Inviscid Incompressible Flow, AIAA paper 64-424, 1964.

45. Tani, I. and Komatsu, Y., Impingement of a Round Jet on a Flat Surface, Proc. XI Int. Cong. of Appl. Mech., pp. 672-676, 1964.

46. Tollmien W., Berechnung turbulenter Ausbreitungvorgänge, ZAMM 6, pp. 468-478 (1926) NACA TM 1085 (1945).

47. Tsuei, Y., Axisymmetric Boundary Layer of A Jet Impinging on A Smooth Plate, Dissertation, Colorado State University, 1963.

48. Van Der Hegge Zijnen, B. G. Measurements of the Velocity Distribution in a Plane Turbulent Jet of Air, Appl. Scient. Res. 7A, 1958, pp. 256-276.

49. Wilson, D. J. Goldstein, R. J., Turbulent Wall Jets with Cylindrical Streamwise Surface Curvature, Transactions of ASME J. of Fluid Eng., Paper No. 76-FE-0.

50. Yanta, W. J., Brott, D. L., Lee, R. E., An Experimental Investigation of the Preston Tube Probe Including Effects of Heat Transfer, Compressibility and Favorable Pressure Gradient, AIAA Fluid and Plasma Dynamics Conference, June 16-18 1969, AIAA Paper No. 69-648.

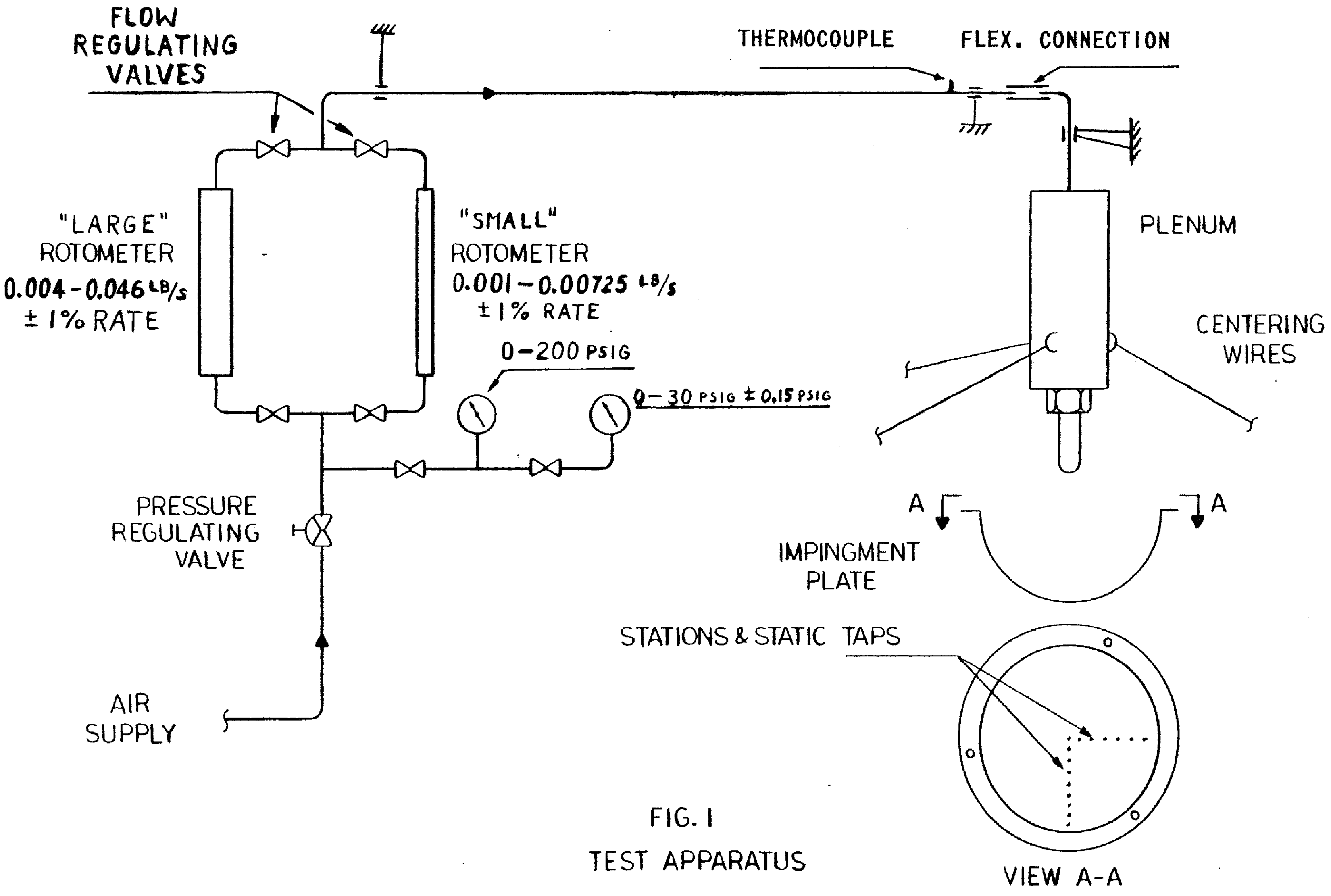

FIG. I

TEST APPARATUS

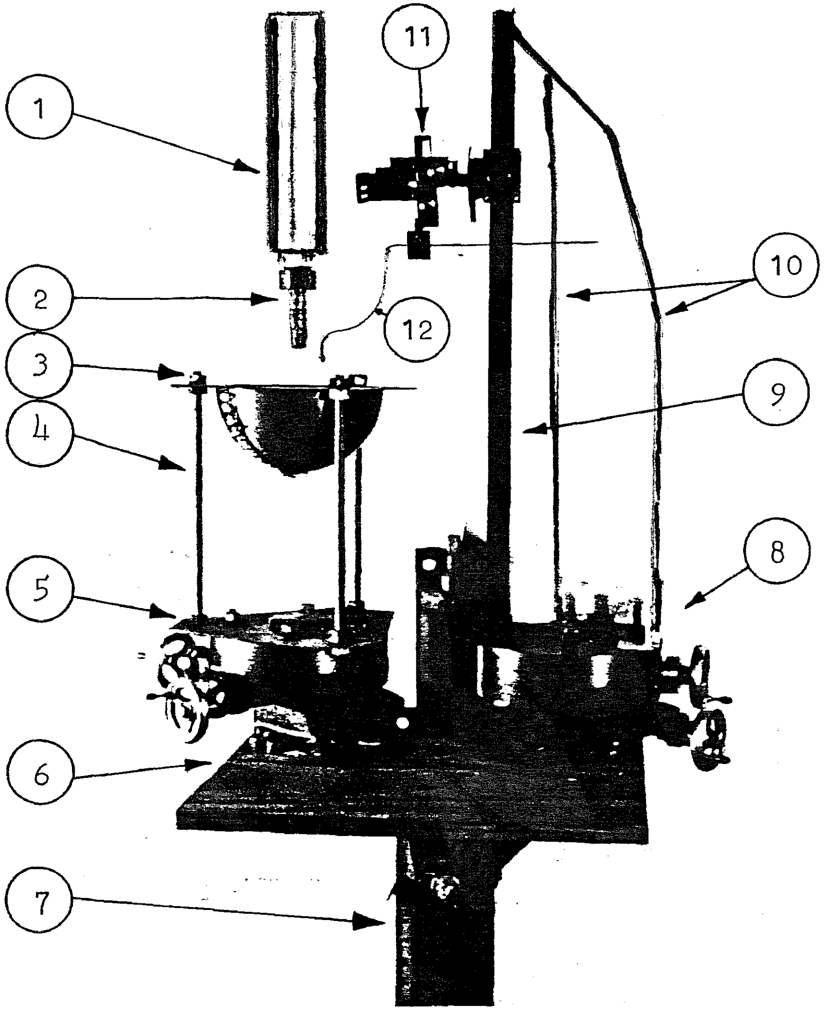

Description

1. Plenum
2. Nozzle
3. Hemispherical impinging plate
4. Adjustable legs
5. Indexing table supporting the impinging plate
6. Support table
7. Vertical guide
8. Indexing table supporting the traversing carriage with probe
9. Traversing carriage beam
10. Beam stiffening rods
11. Traversing carriage
12. Probe

FIG. 1a TEST ARRANGEMENT

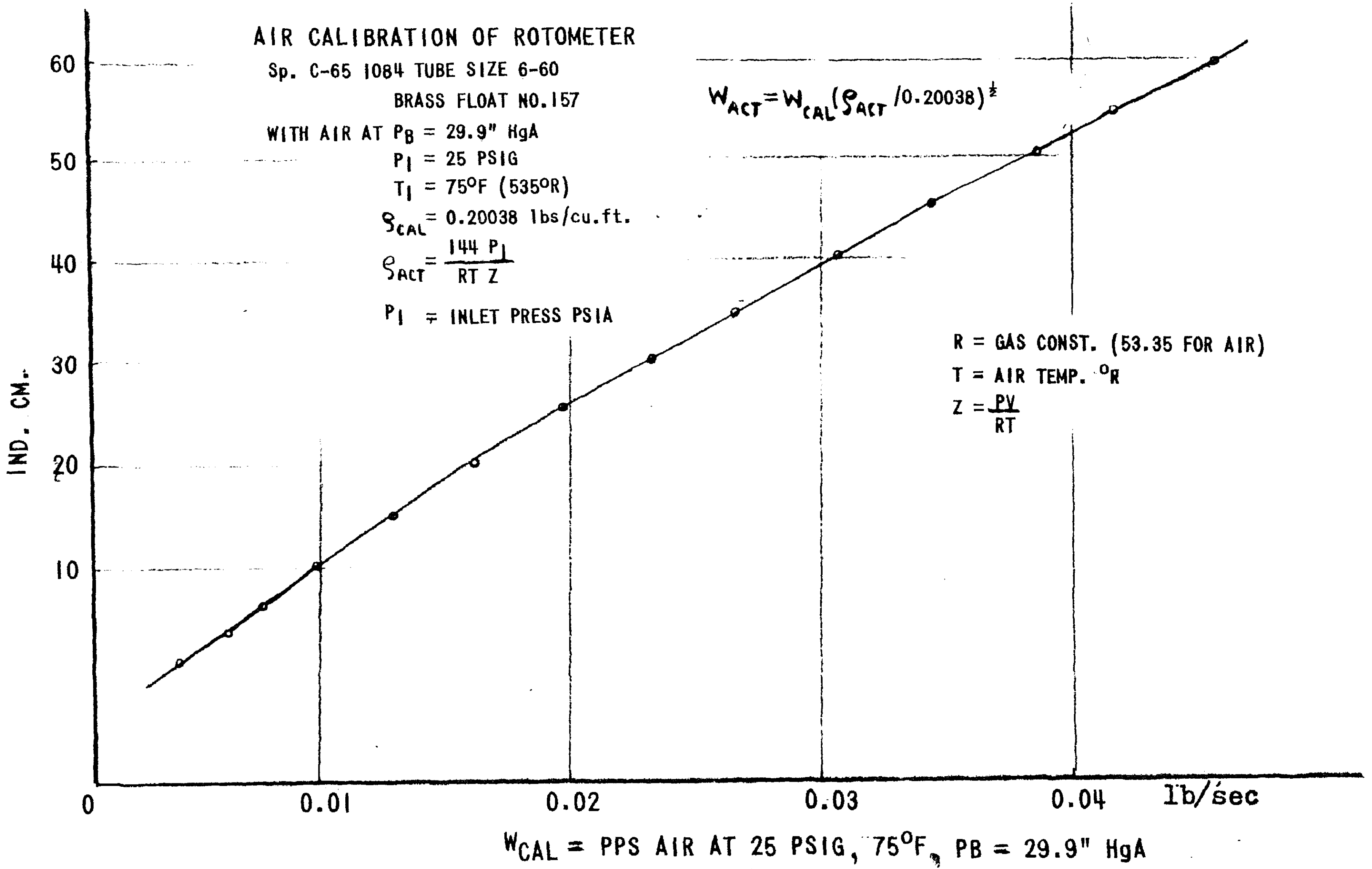

FIG. 1b LARGE ROTOMETER CALIBRATION CURVE

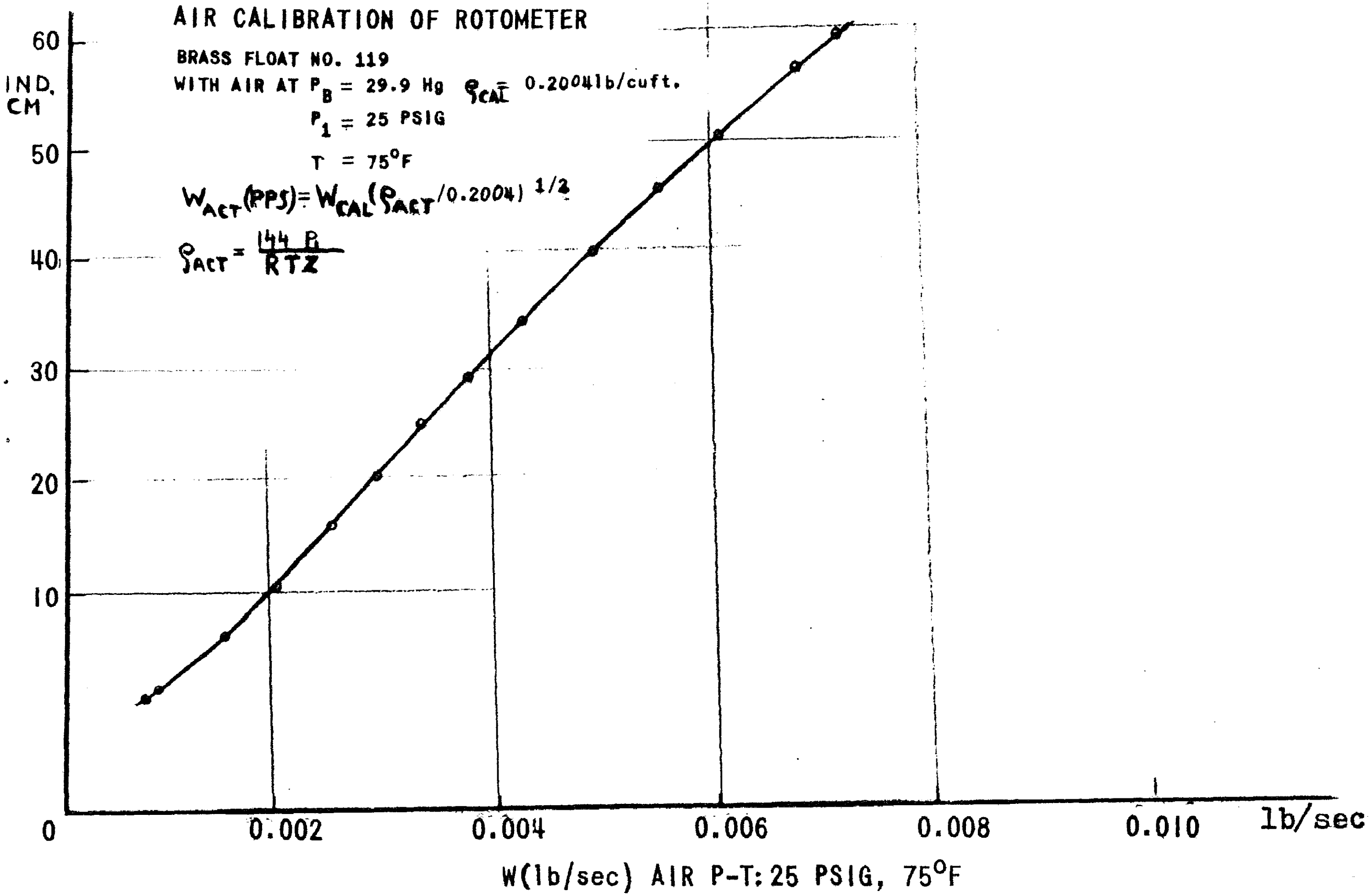

FIG. Ic SMALL ROTOMETER CALIBRATION CURVE

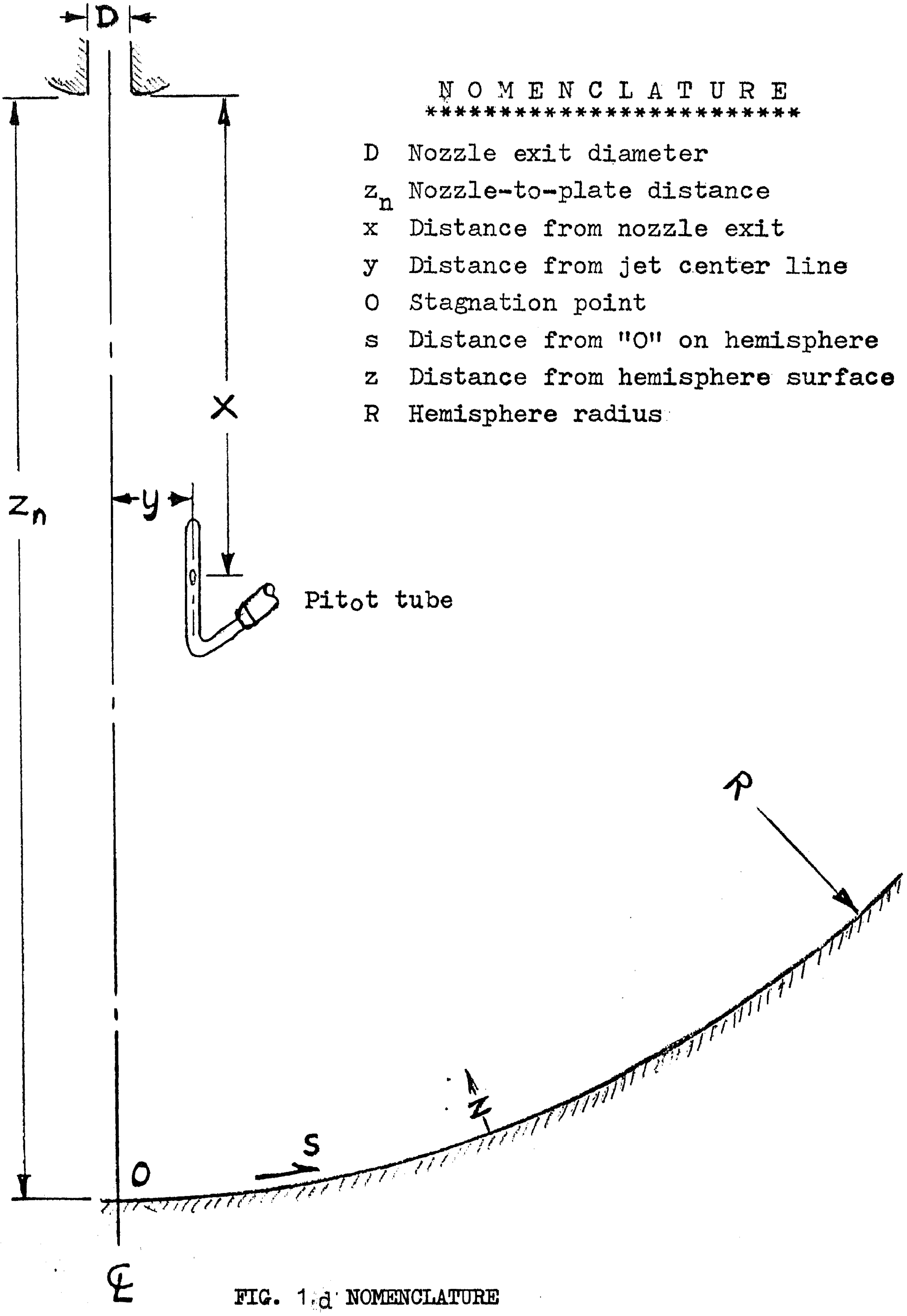

NOMENCLATURE

D	Nozzle exit diameter
z_n	Nozzle-to-plate distance
x	Distance from nozzle exit
y	Distance from jet center line
O	Stagnation point
s	Distance from "O" on hemisphere
z	Distance from hemisphere surface
R	Hemisphere radius

FIG. 1.d NOMENCLATURE

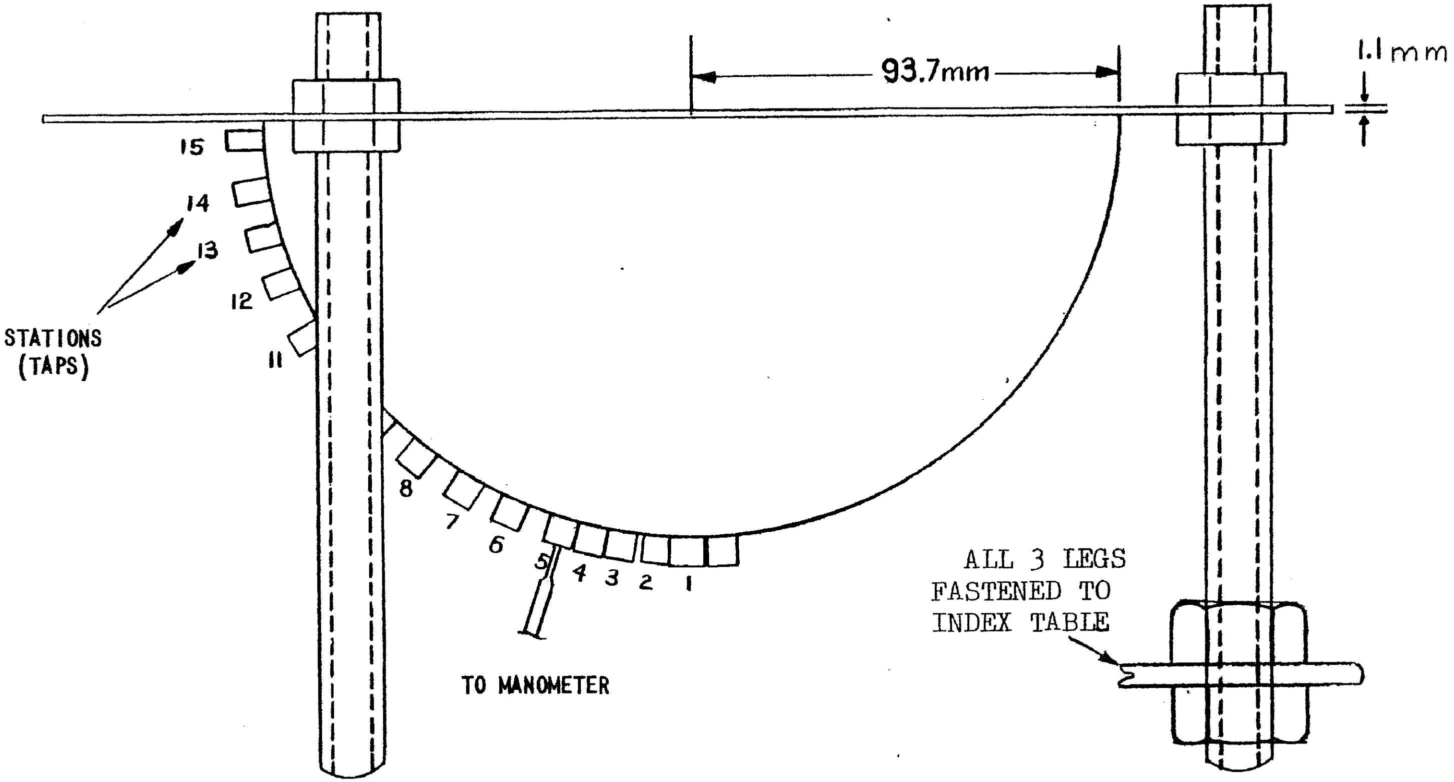

FIG. 2 IMPINGMENT HEMISPHERICAL PLATE FOR FLOW STATIC PRESSURE MEASUREMENTS

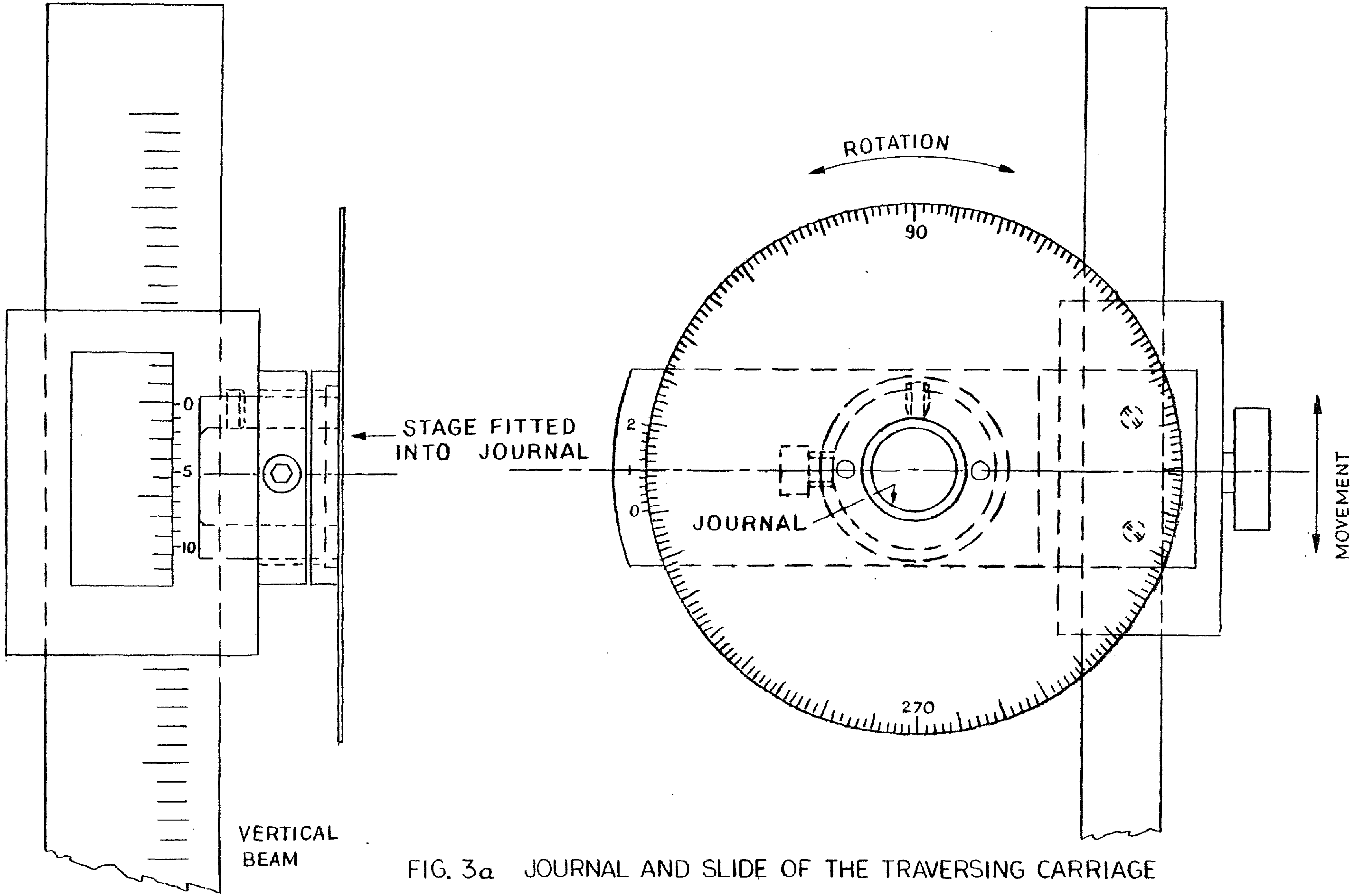

FIG. 3*a* JOURNAL AND SLIDE OF THE TRAVERSING CARRIAGE

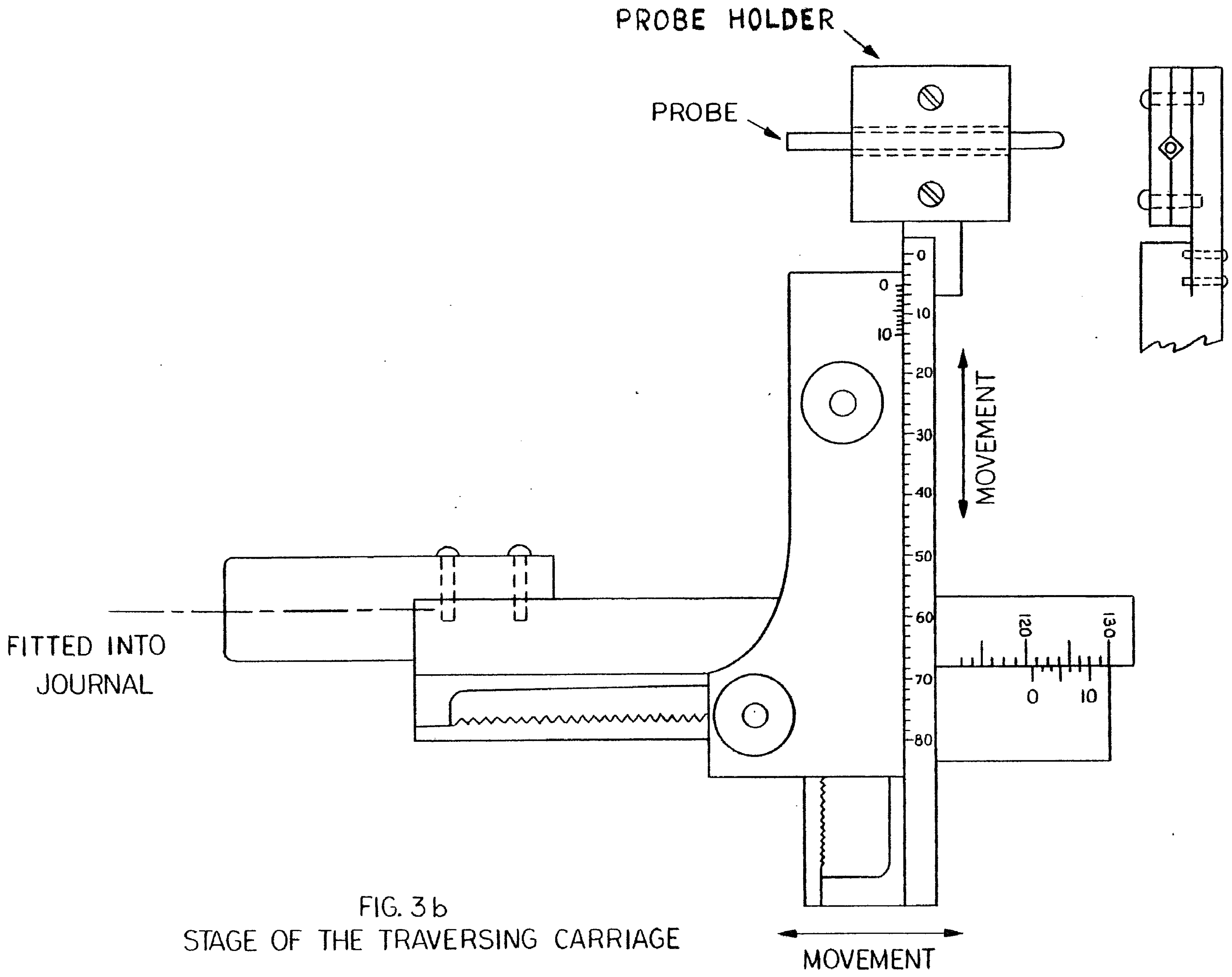

FIG. 3b
STAGE OF THE TRAVERSING CARRIAGE

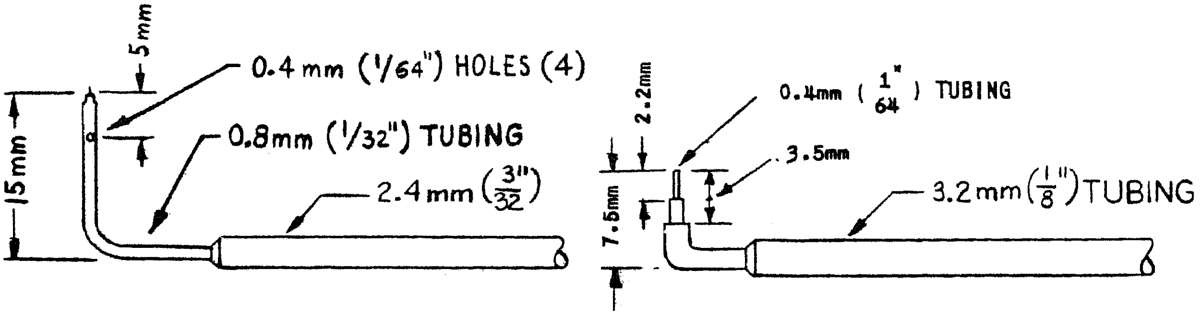

STATIC PRESSURE PROBE

TOTAL PRESSURE PROBE

FIG. 4

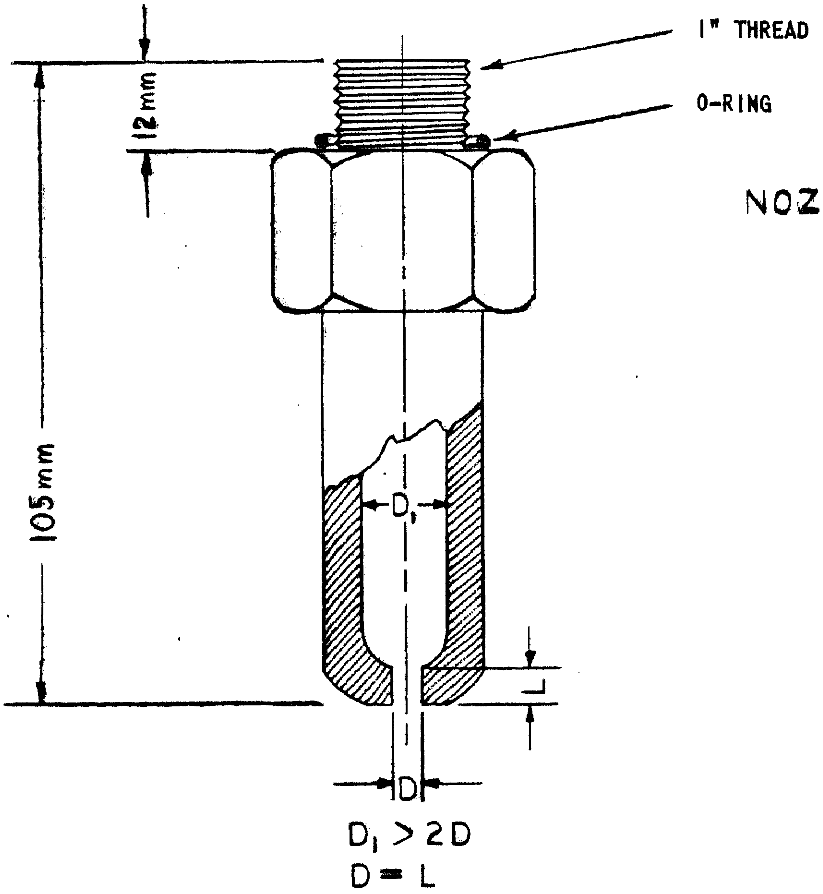

NOZZLES USED
D = 6.35 mm
D = 9.5 mm

FIG. 5
NOZZLE

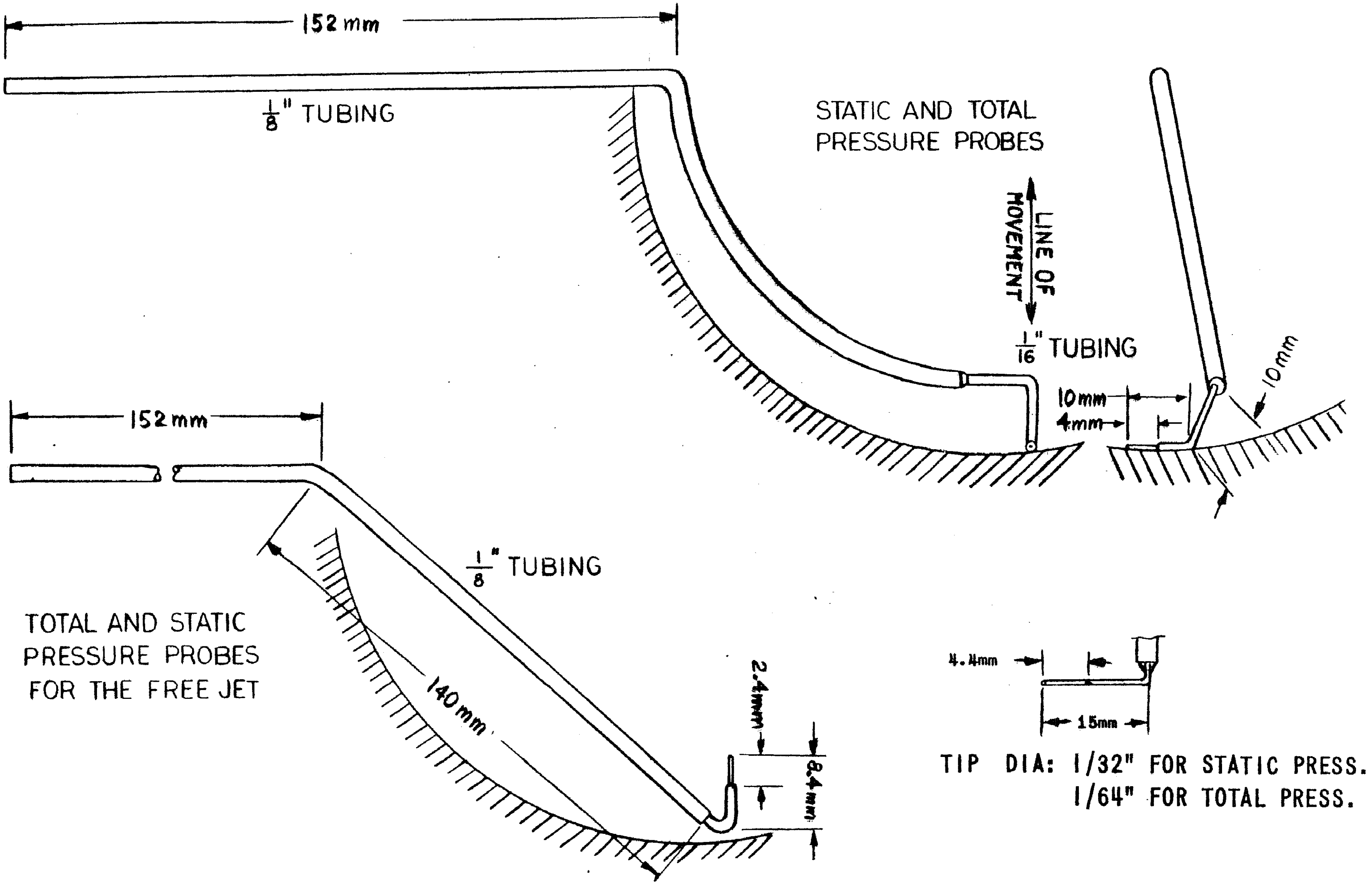

FIG. 6 MODIFIED PRESSURE PROBES

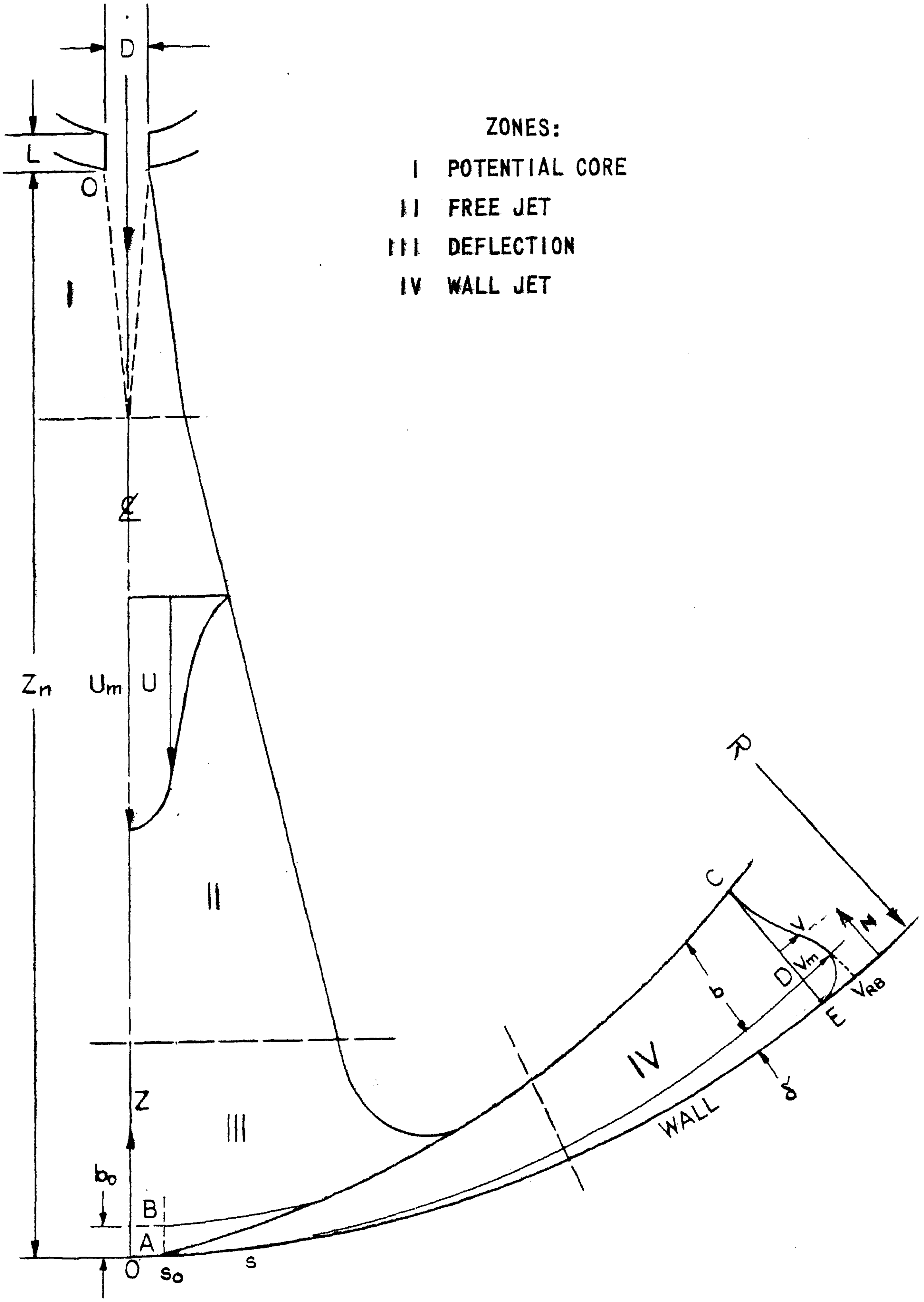

FIG.7 HEMISPHERICAL PLATE JET ZONES

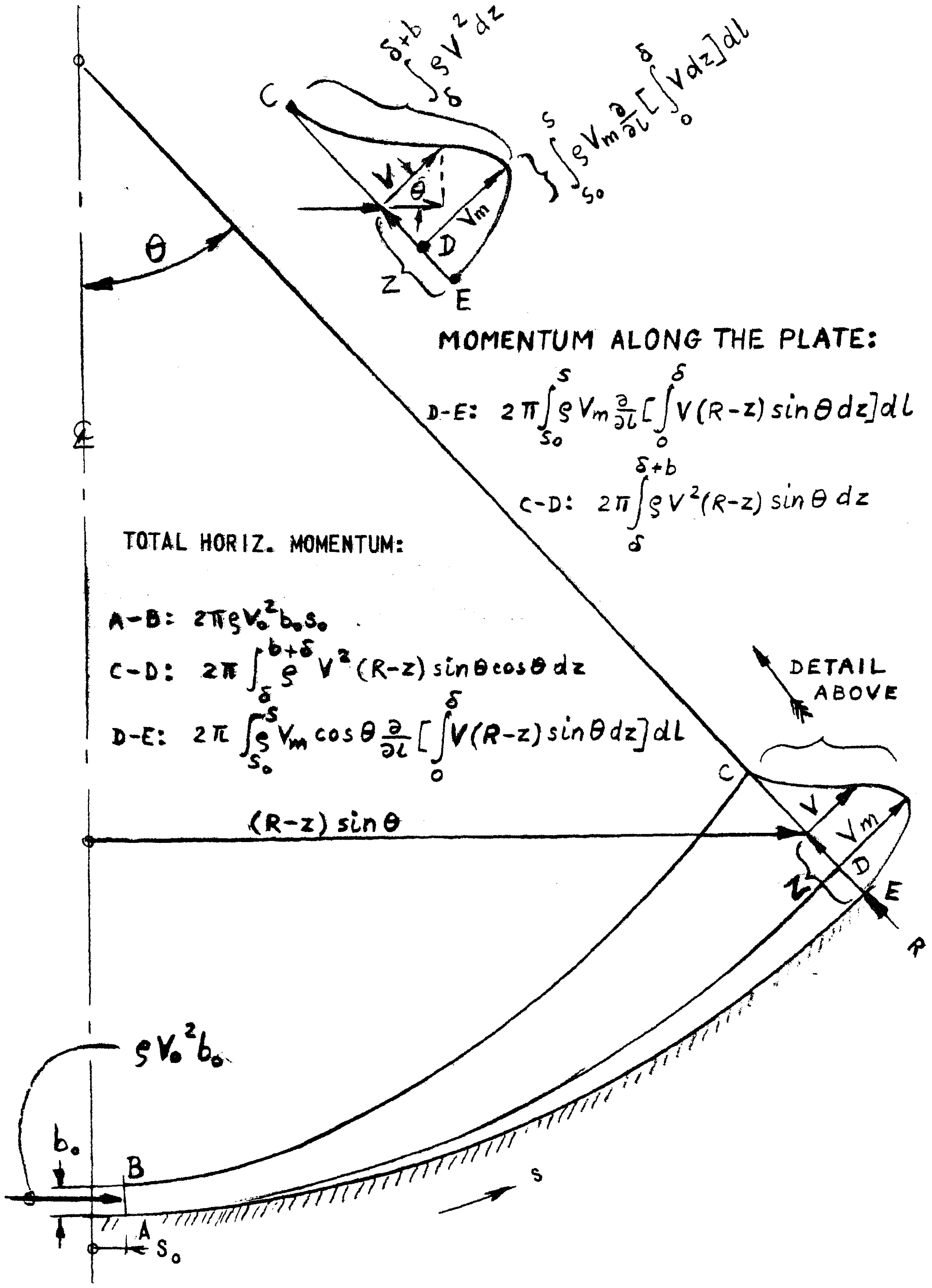

FIG. 7a MOMENTUM FLUX MODEL

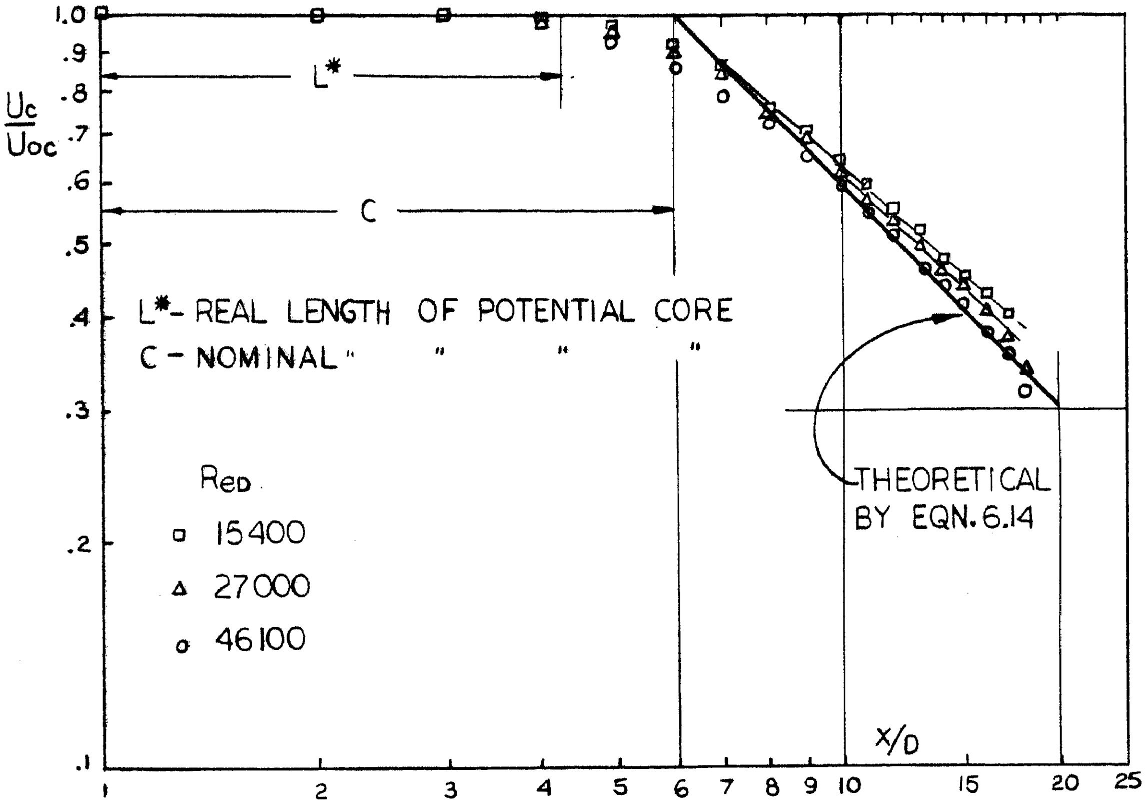

CENTER LINE VELOCITY DECAY FOR Zn/D=20, D=6.35mm

FIG. 8

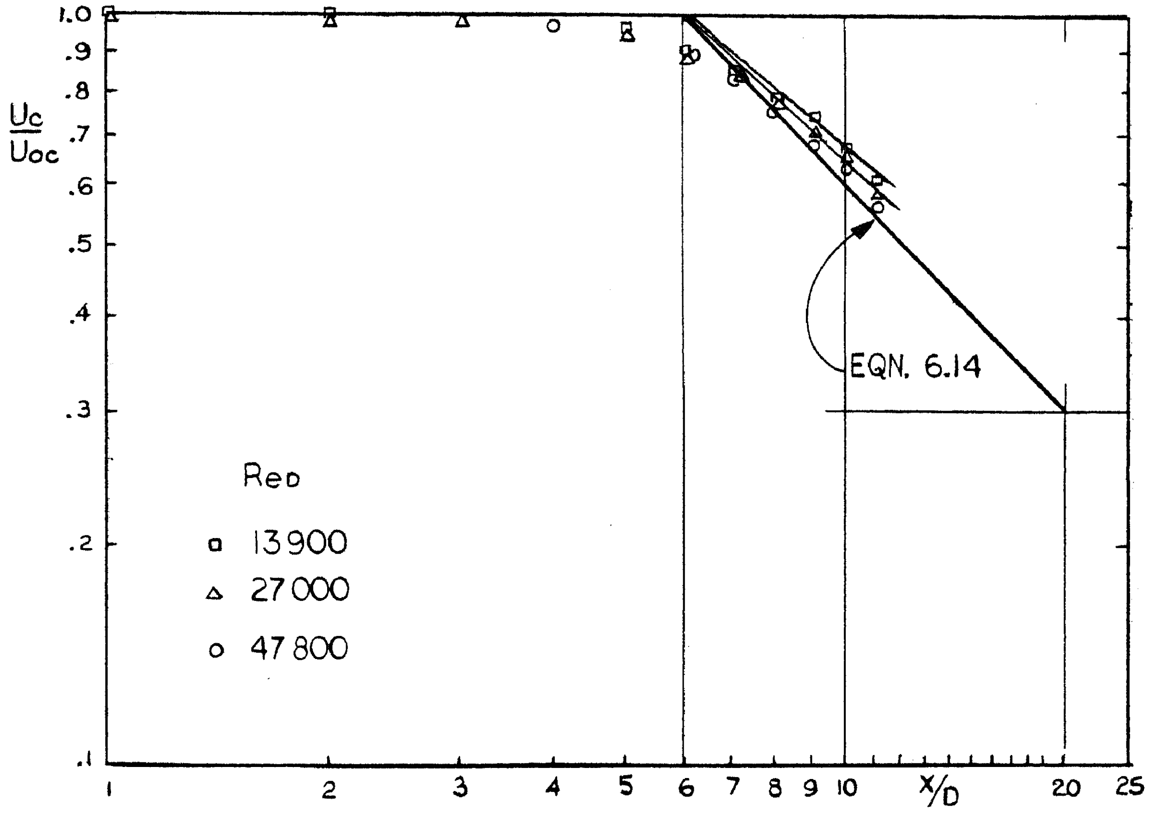

CENTER LINE VELOCITY DECAY FOR Zn/D=13, D=6.35mm

FIG.9

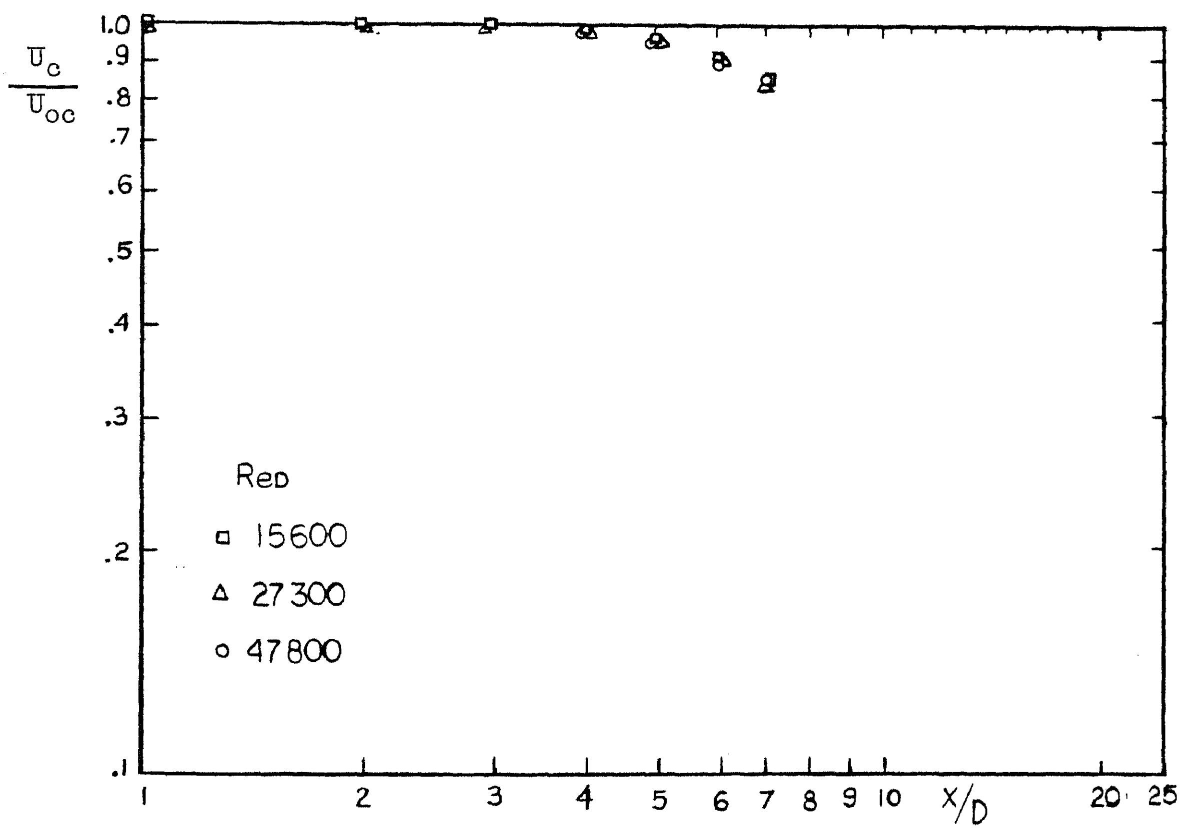

CENTER LINE VELOCITY DECAY FOR Zn/D=9, D=6.35mm

FIG. 10

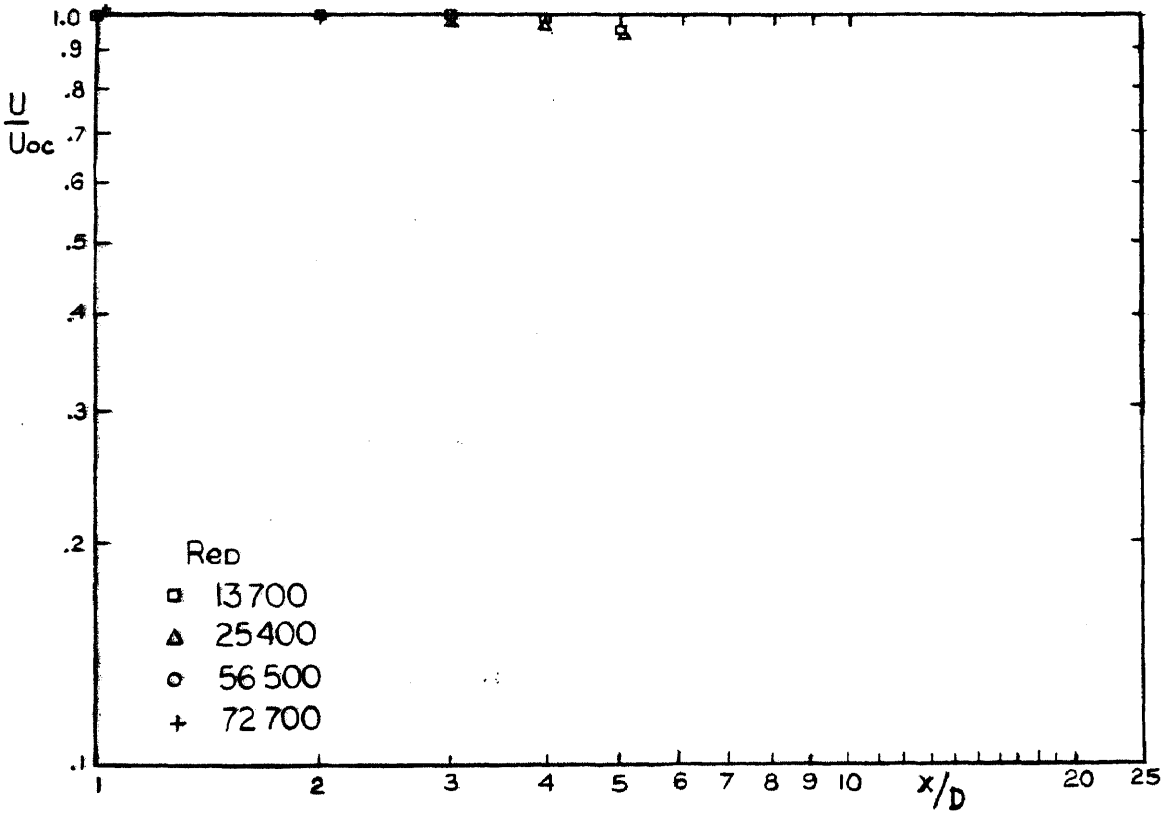

CENTER LINE VELOCITY DECAY FOR Zn/D=7, D=6.35mm

FIG. 11

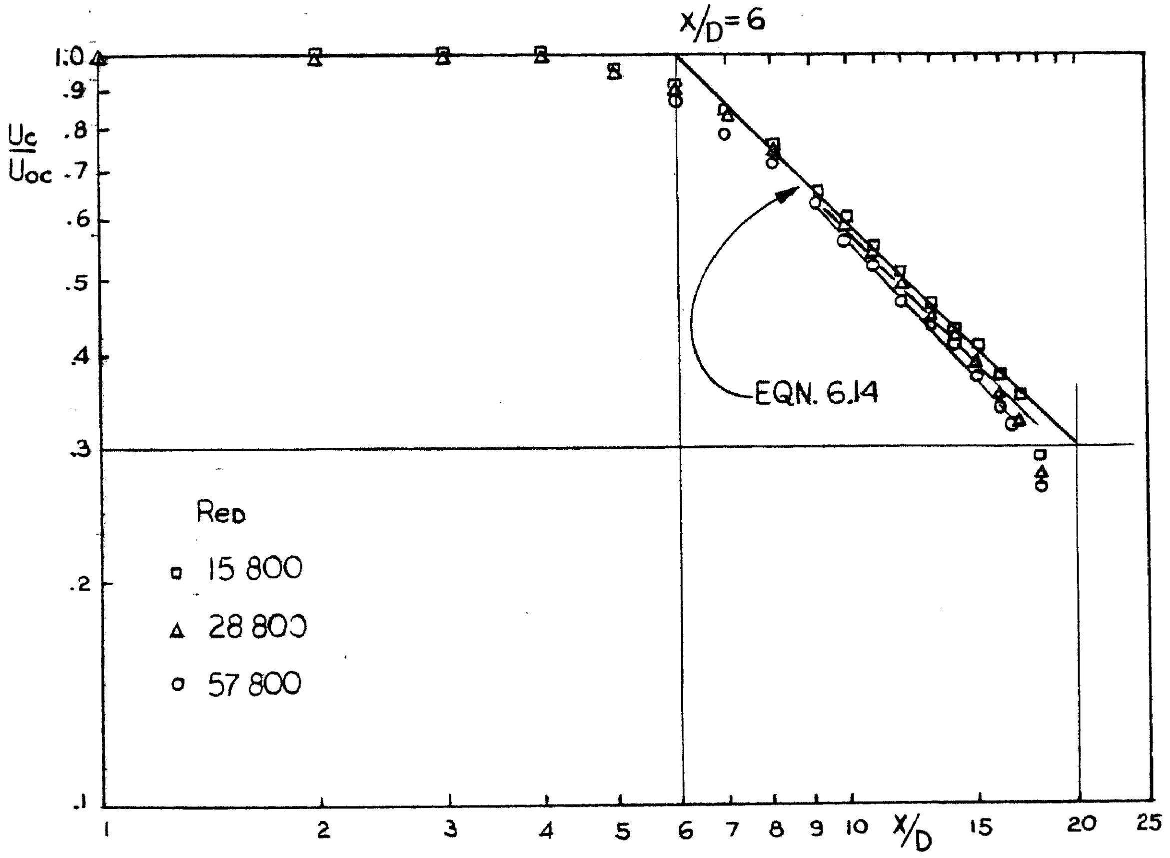

CENTER LINE VELOCITY DECAY FOR Zn/D=20, D=9.5mm

FIG. 12

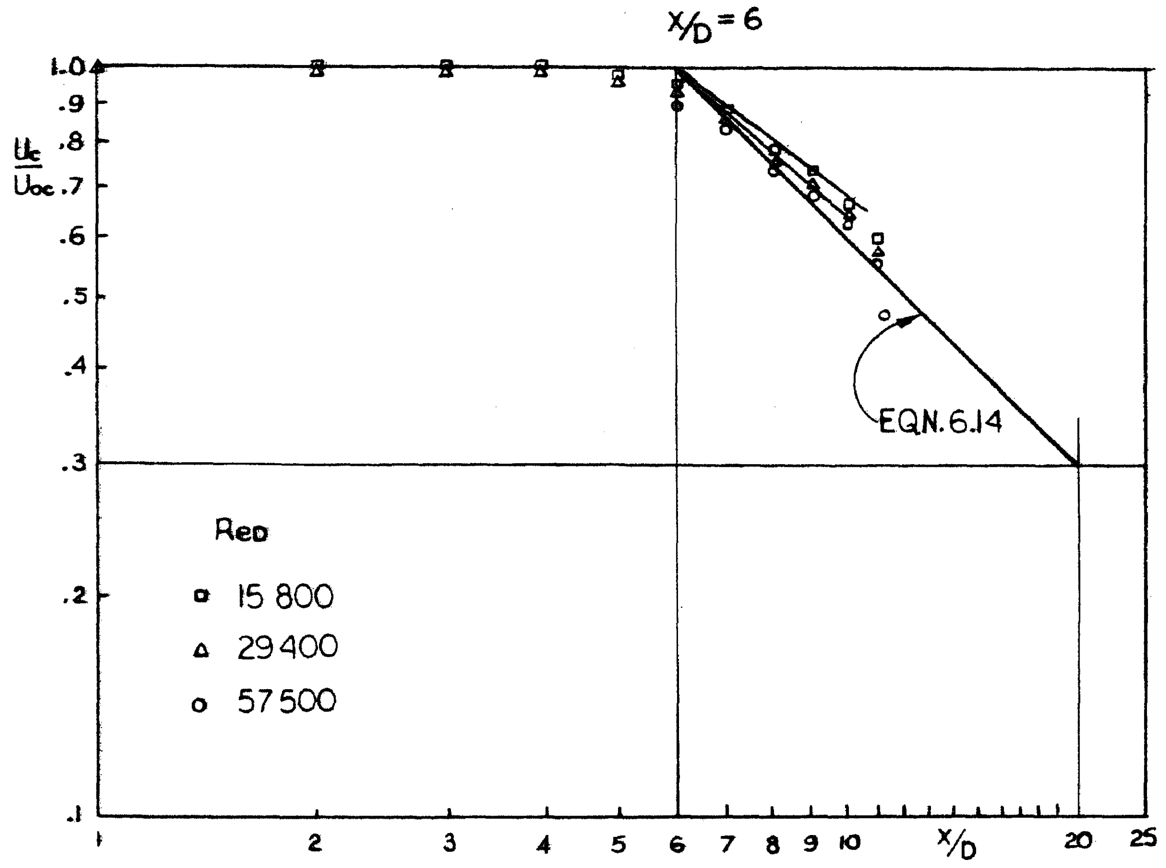

CENTER LINE VELOCITY DECAY FOR Zn/D=13, D=9.5mm

FIG. 13

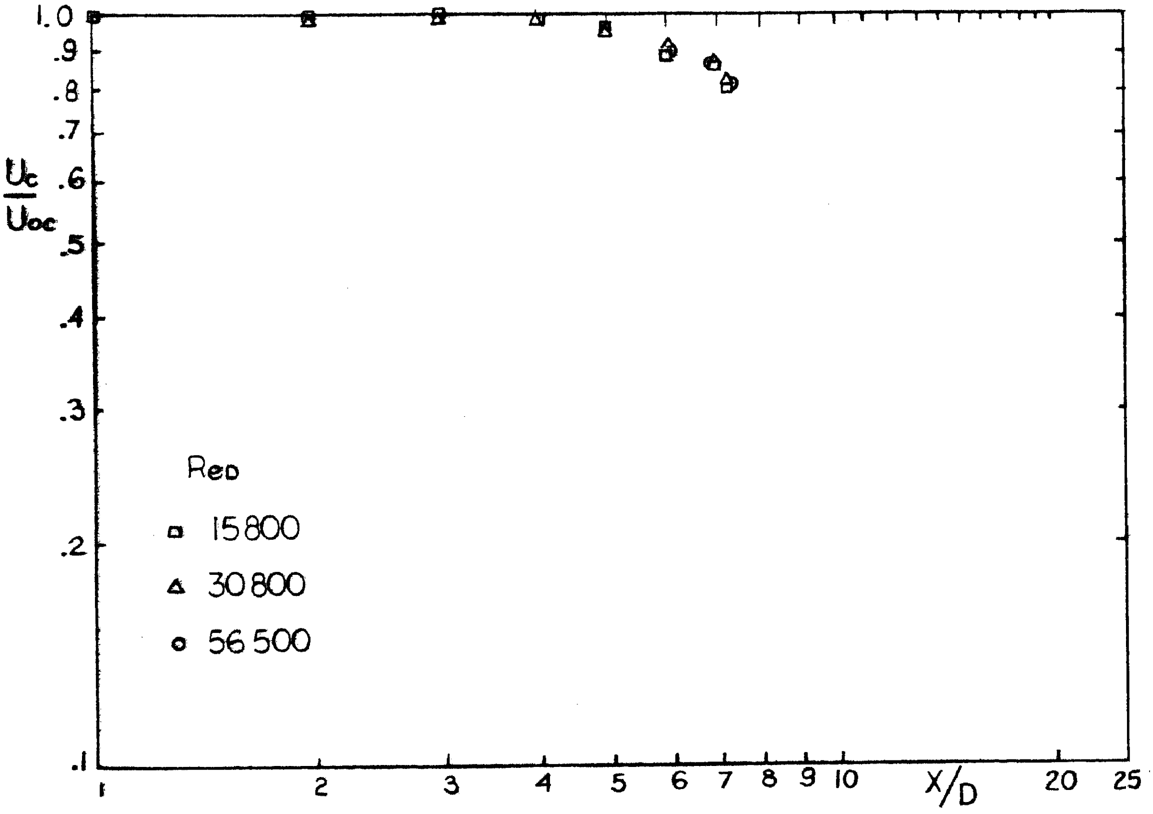

CENTER LINE VELOCITY DECAY FOR Zn/D=9, D=9.5mm

FIG. 14

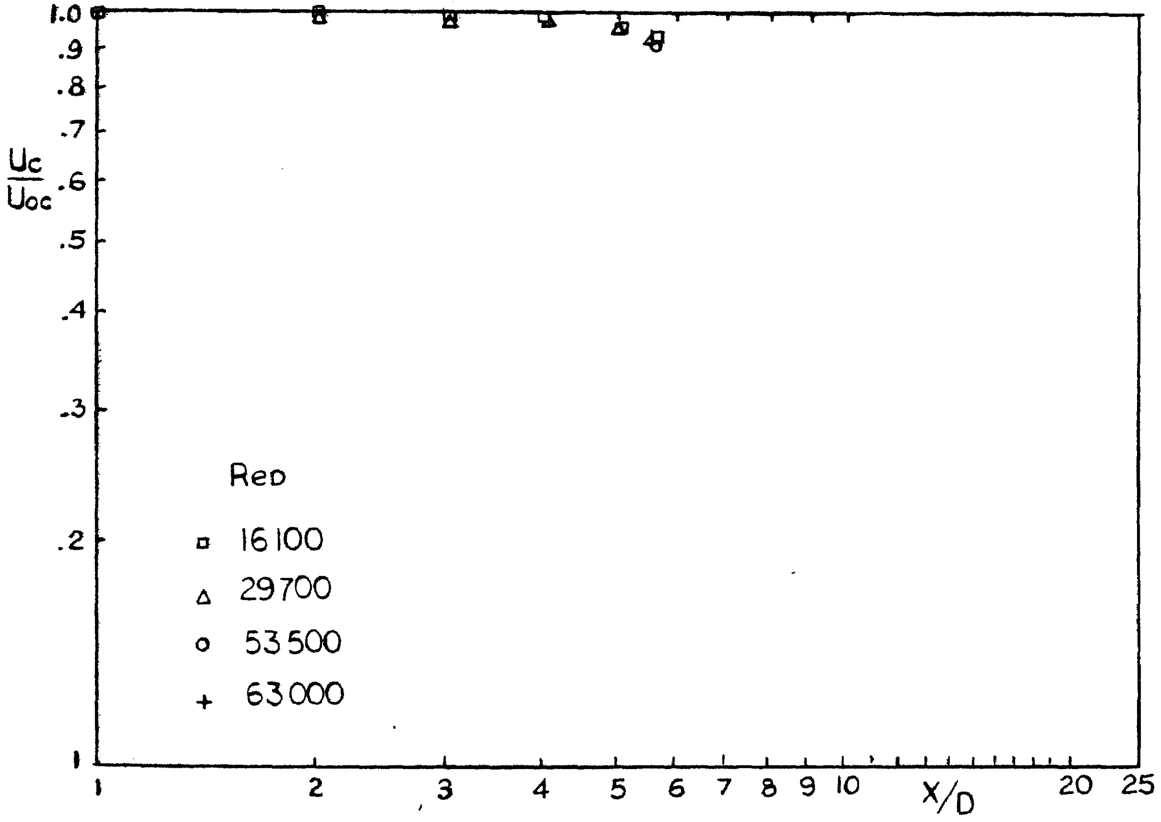

CENTER LINE VELOCITY DECAY FOR Zn/D=7, D=9.5mm

FIG. 15

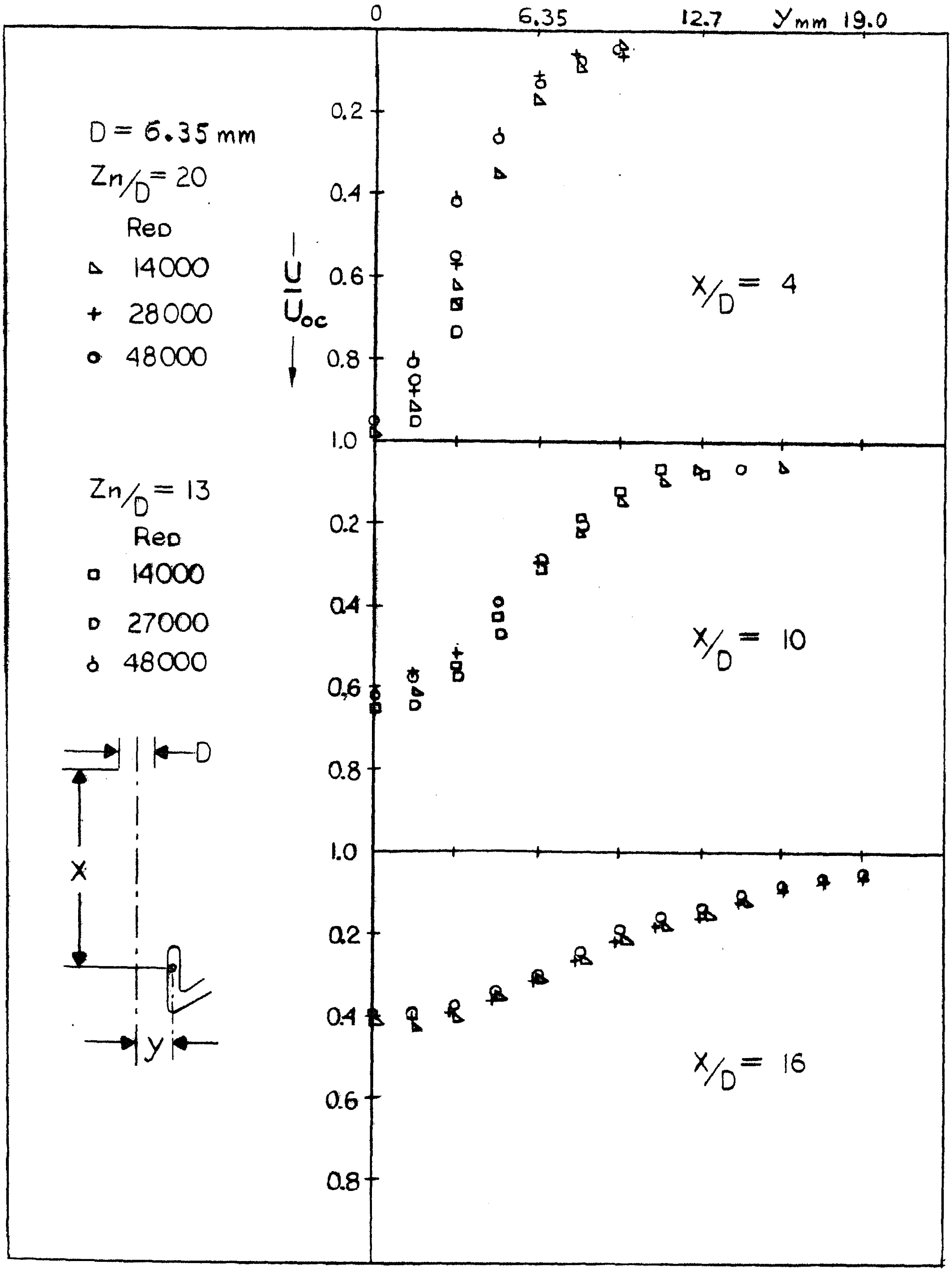

VELOCITY PROFILE ACROSS JET CENTERLINE

FIG. 16-1

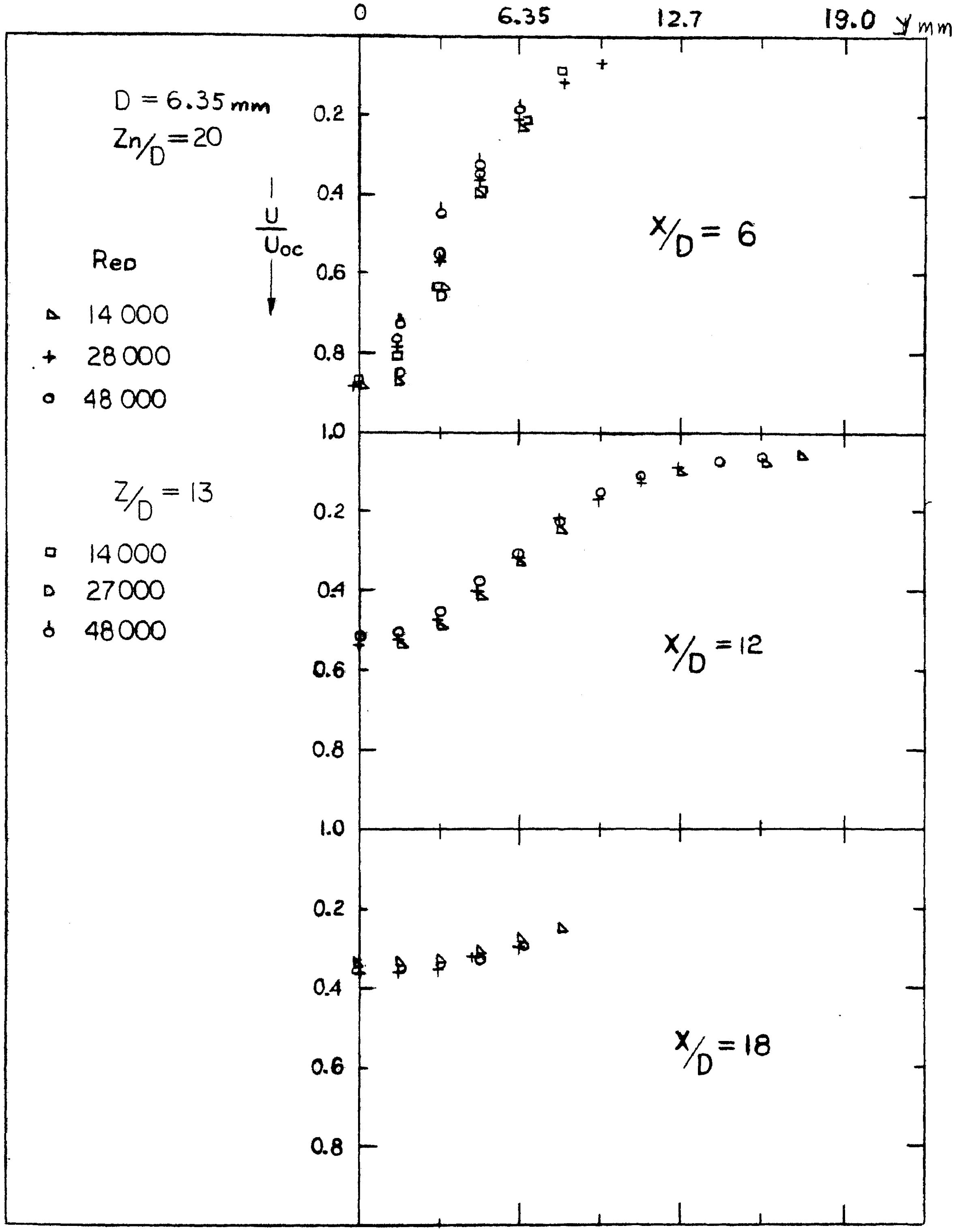

VELOCITY PROFILE ACROSS JET CENTER LINE

FIG. 16-2

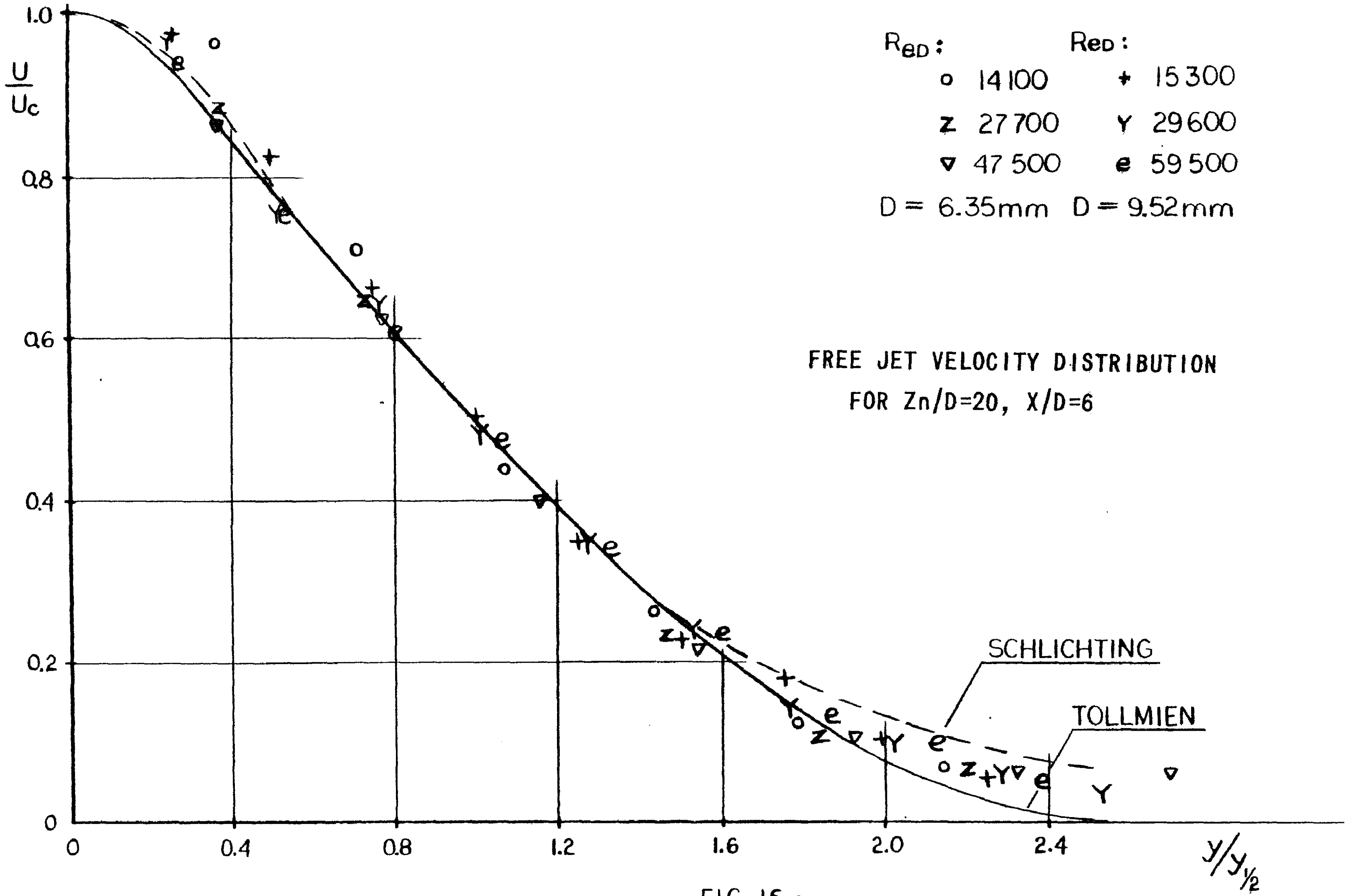

FREE JET VELOCITY DISTRIBUTION
FOR Zn/D=20, X/D=6

FIG.16a

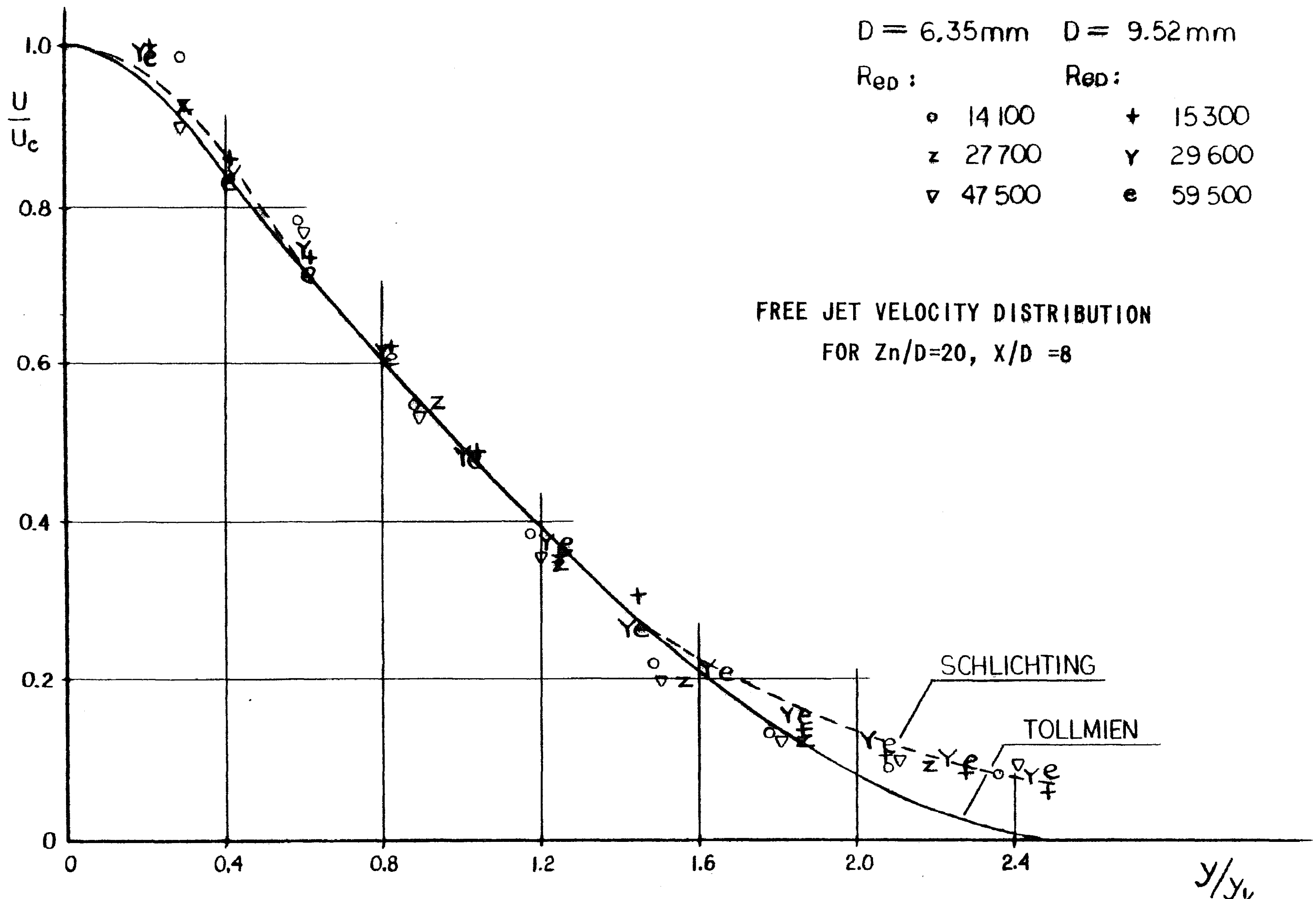

FREE JET VELOCITY DISTRIBUTION
FOR Zn/D=20, X/D =8

FIG. 16b

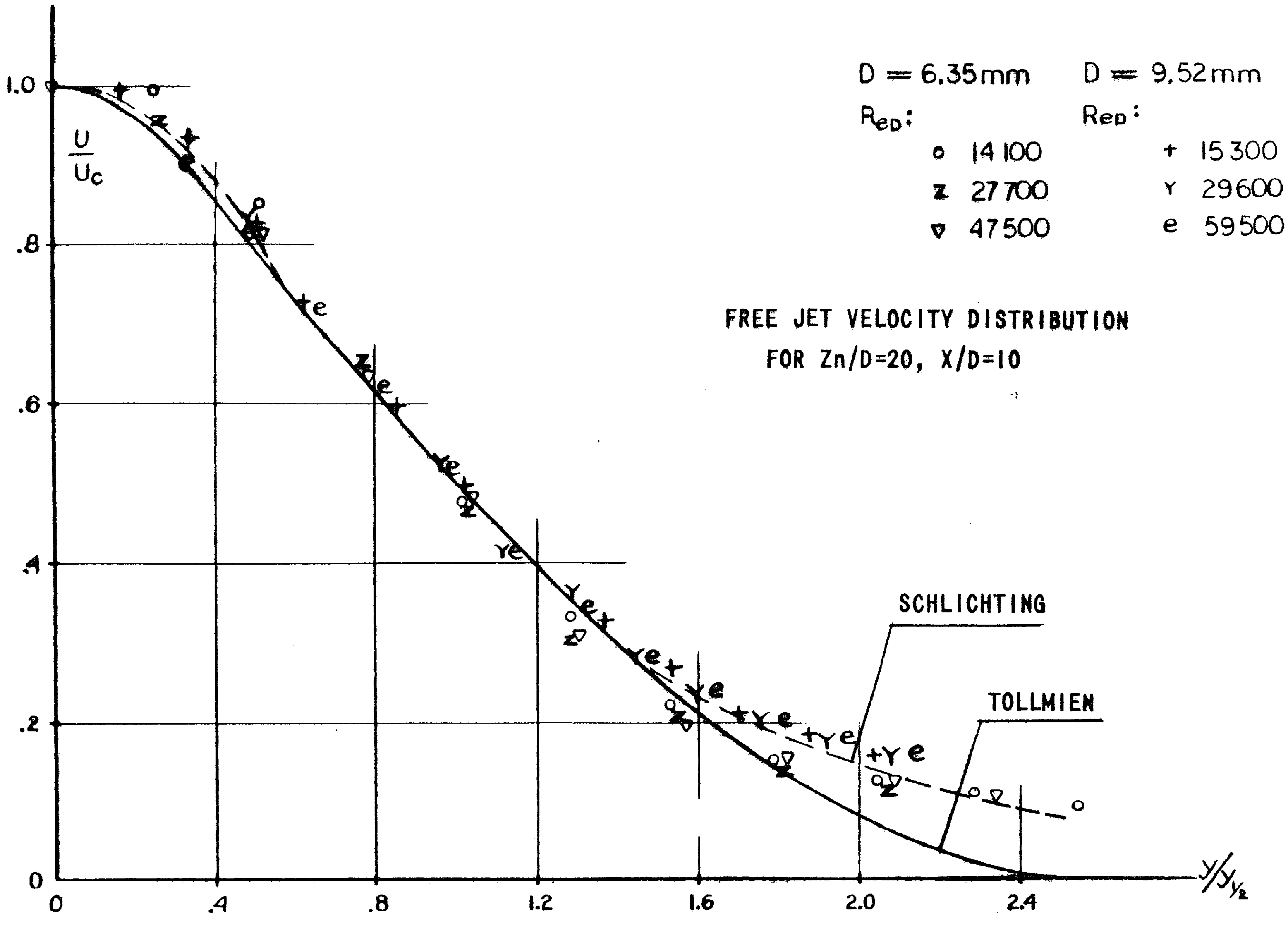
D = 6.35 mm
R_{eD}:
○ 14 100
z 27 700
▽ 47 500
D = 9.52 mm
R_{eD}:
+ 15 300
Y 29600
e 59500
FREE JET VELOCITY DISTRIBUTION
FOR Zn/D=20, X/D=10
SCHLICHTING
TOLLMIEN
U/Uc
1.0
.8
.6
.4
.2
0
0
.4
.8
1.2
1.6
2.0
2.4
y/y½

FIG. 16c

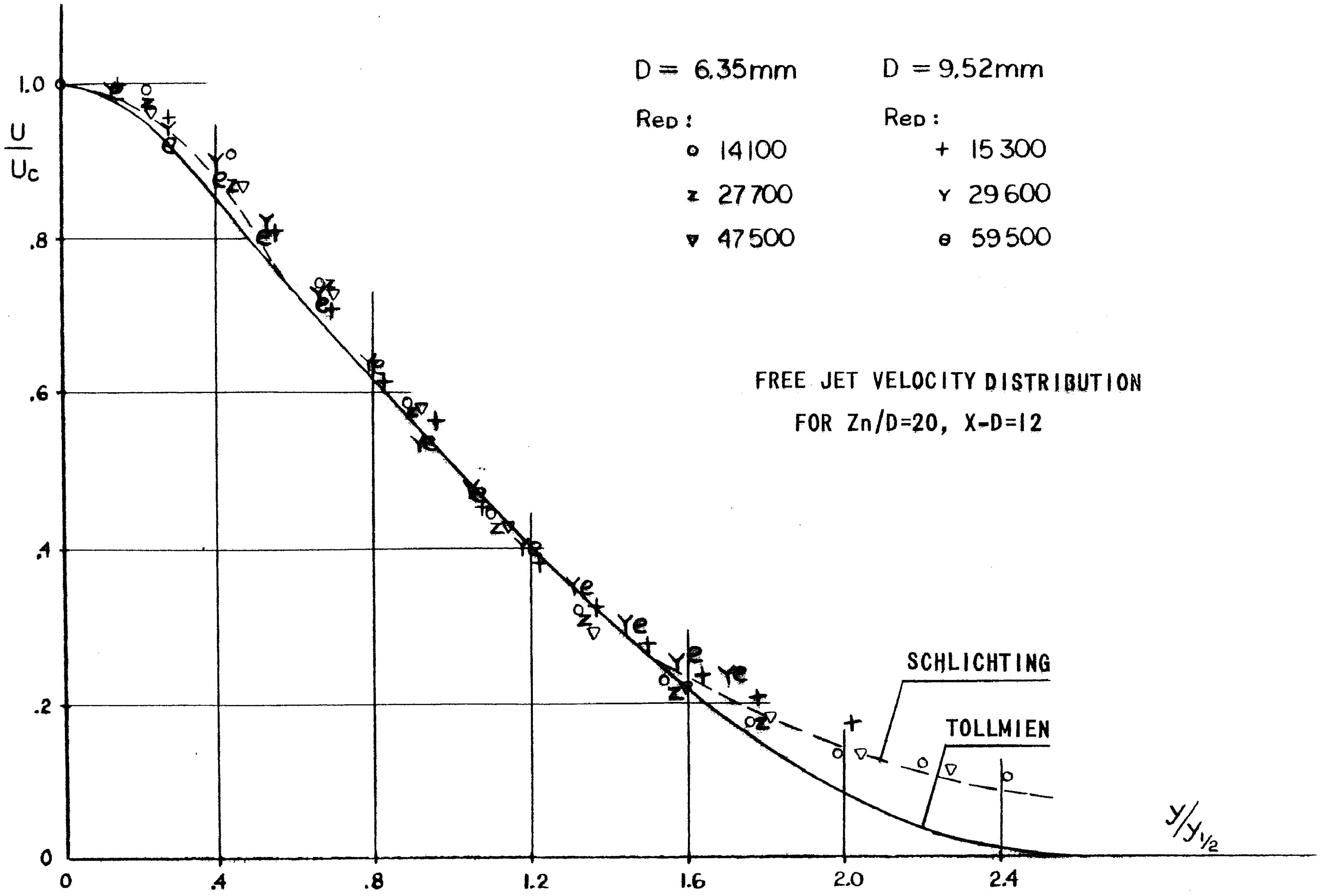
D = 6.35mm
D = 9.52mm
ReD :
○ 14100
z 27700
▽ 47500
ReD :
+ 15300
Y 29600
e 59500
FREE JET VELOCITY DISTRIBUTION
FOR Zn/D=20, X-D=12
SCHLICHTING
TOLLMIEN
U/Uc
1.0
.8
.6
.4
.2
0
.4
.8
1.2
1.6
2.0
2.4
y/y½

FIG. 16d

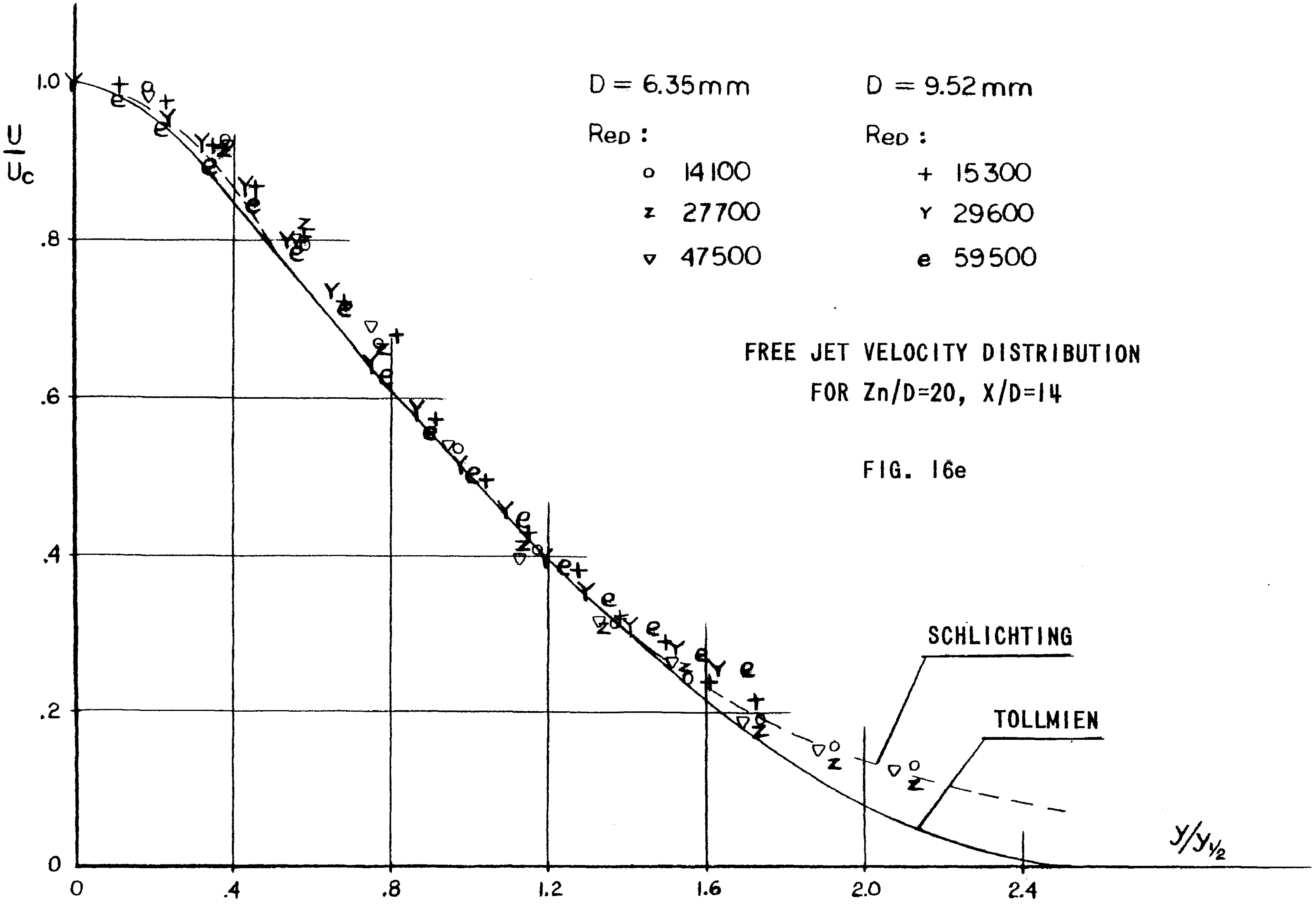

FREE JET VELOCITY DISTRIBUTION
FOR Zn/D=20, X/D=14

FIG. 16e

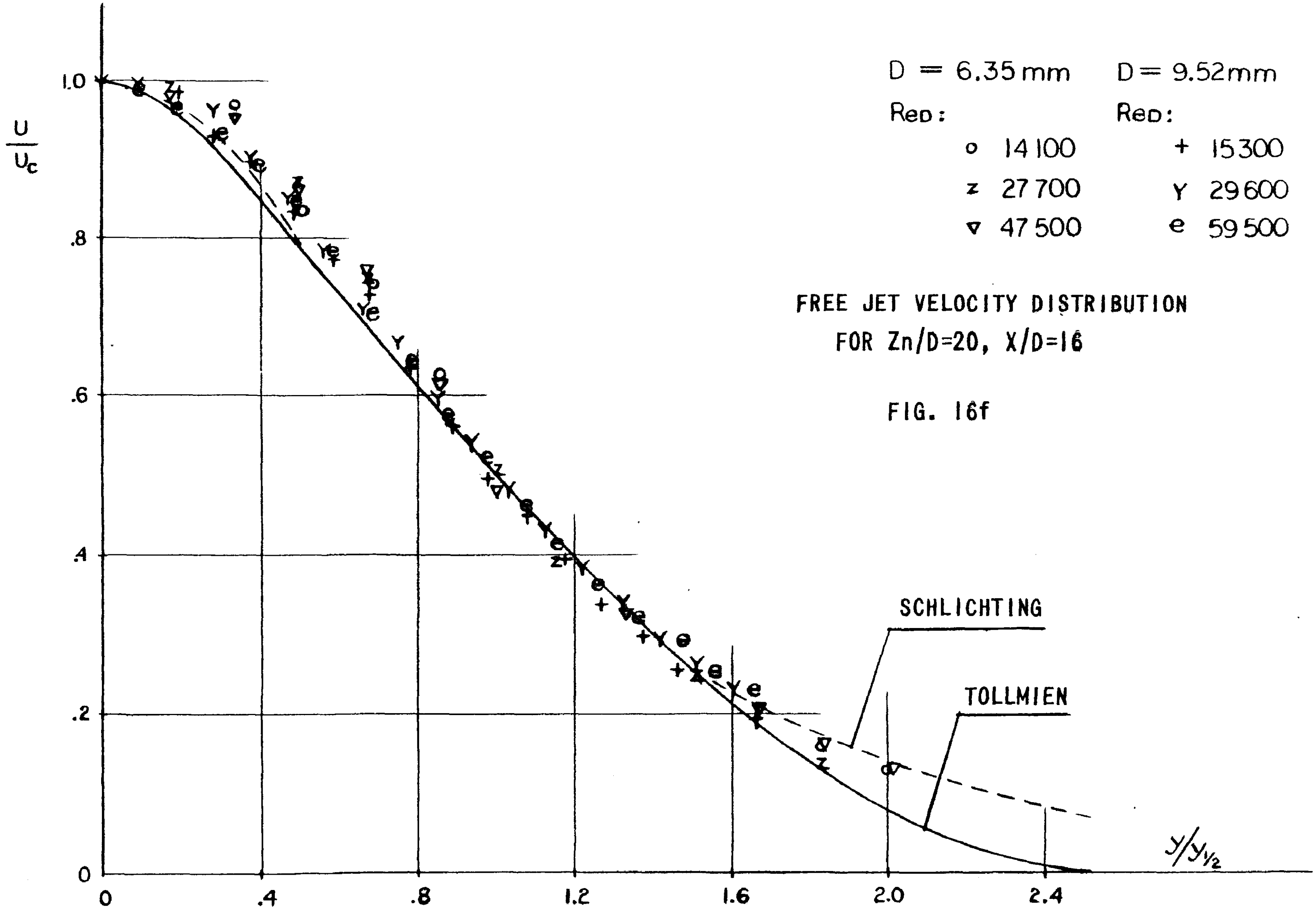

FREE JET VELOCITY DISTRIBUTION
FOR Zn/D=20, X/D=16

FIG. 16f

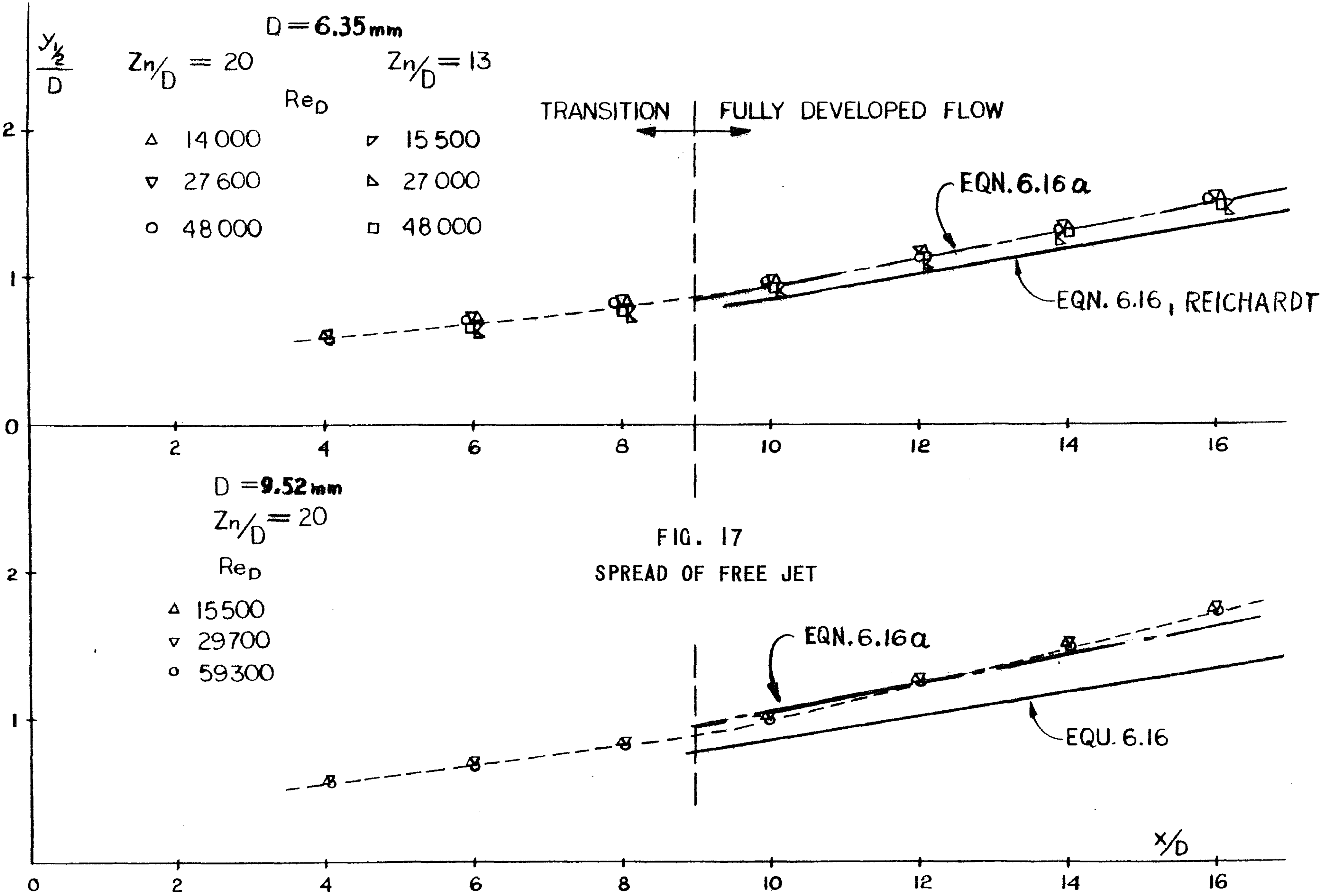

FIG. 17

SPREAD OF FREE JET

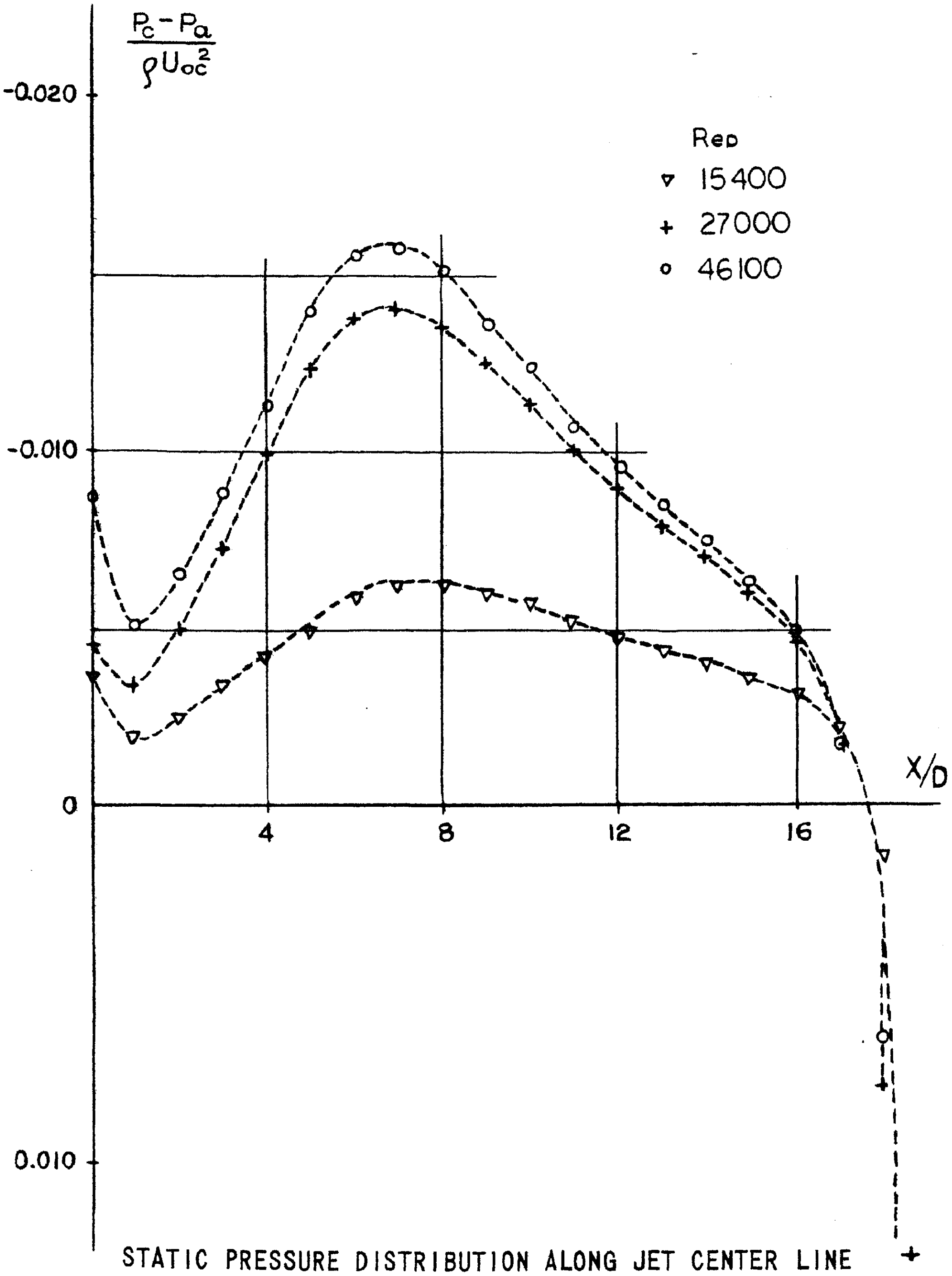

STATIC PRESSURE DISTRIBUTION ALONG JET CENTER LINE

FOR Zn/D=20, D=6.35mm

FIG.18a

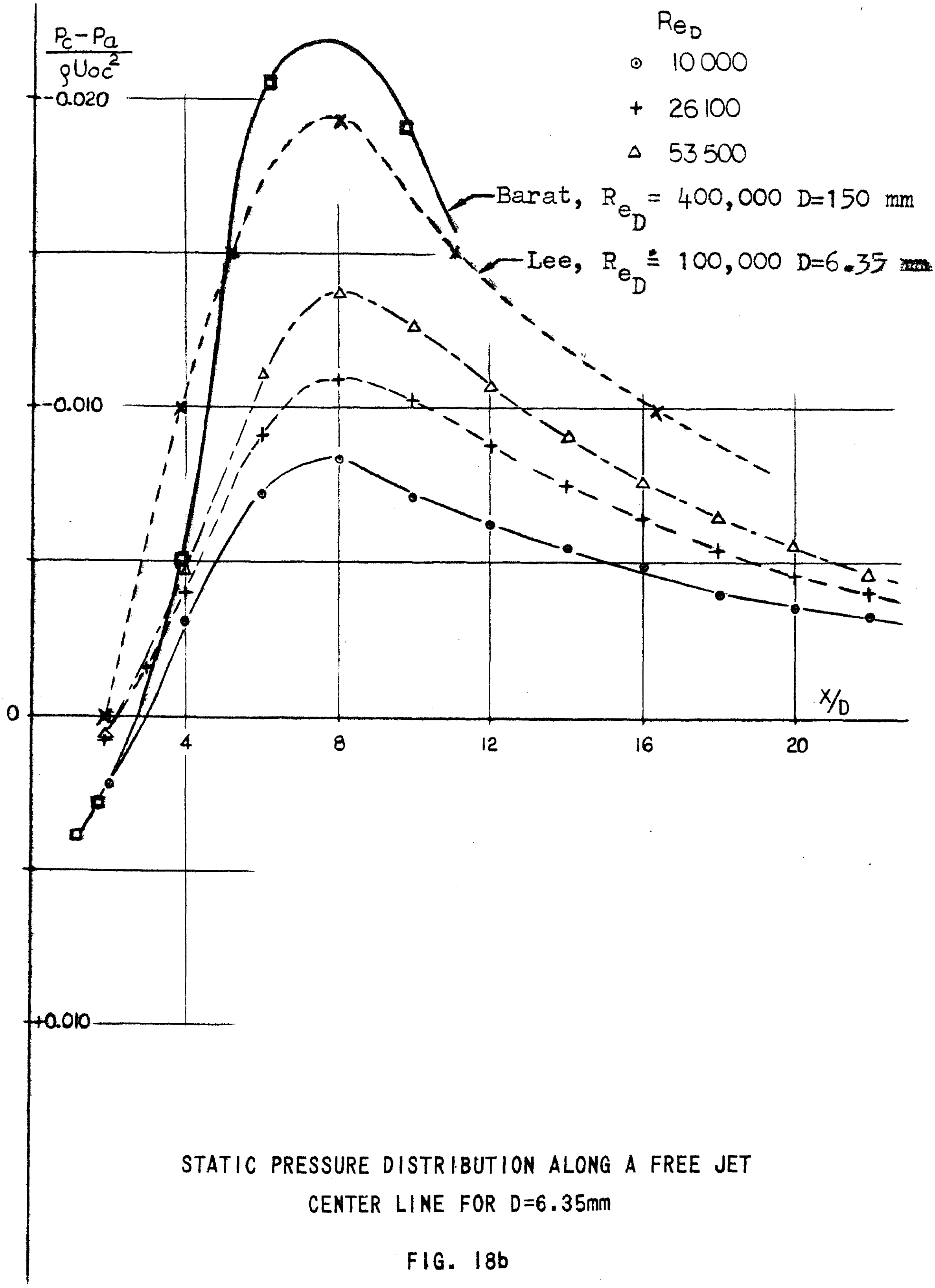

STATIC PRESSURE DISTRIBUTION ALONG A FREE JET CENTER LINE FOR D=6.35mm

FIG. 18b

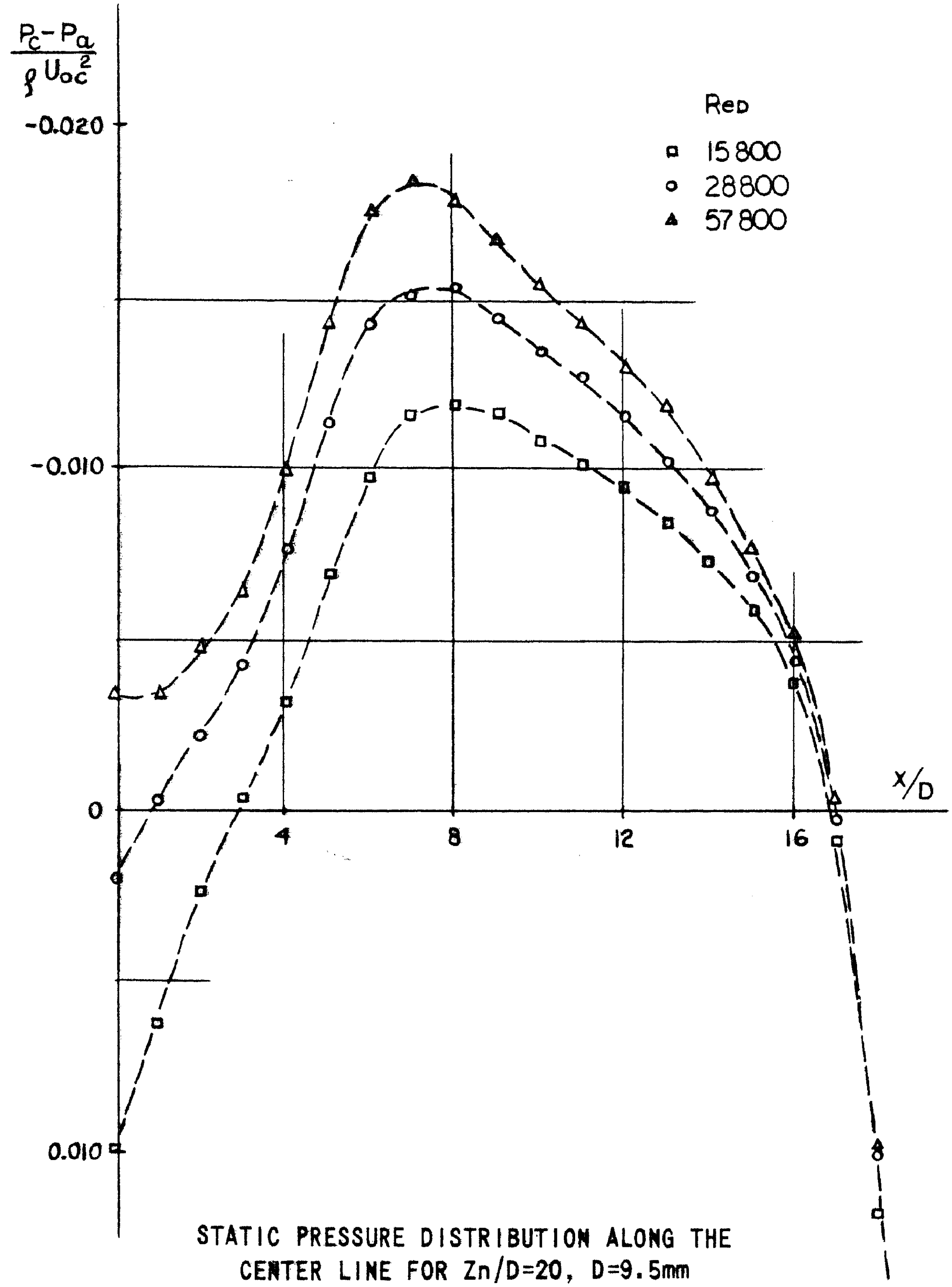

STATIC PRESSURE DISTRIBUTION ALONG THE CENTER LINE FOR Zn/D=20, D=9.5mm

FIG. 19

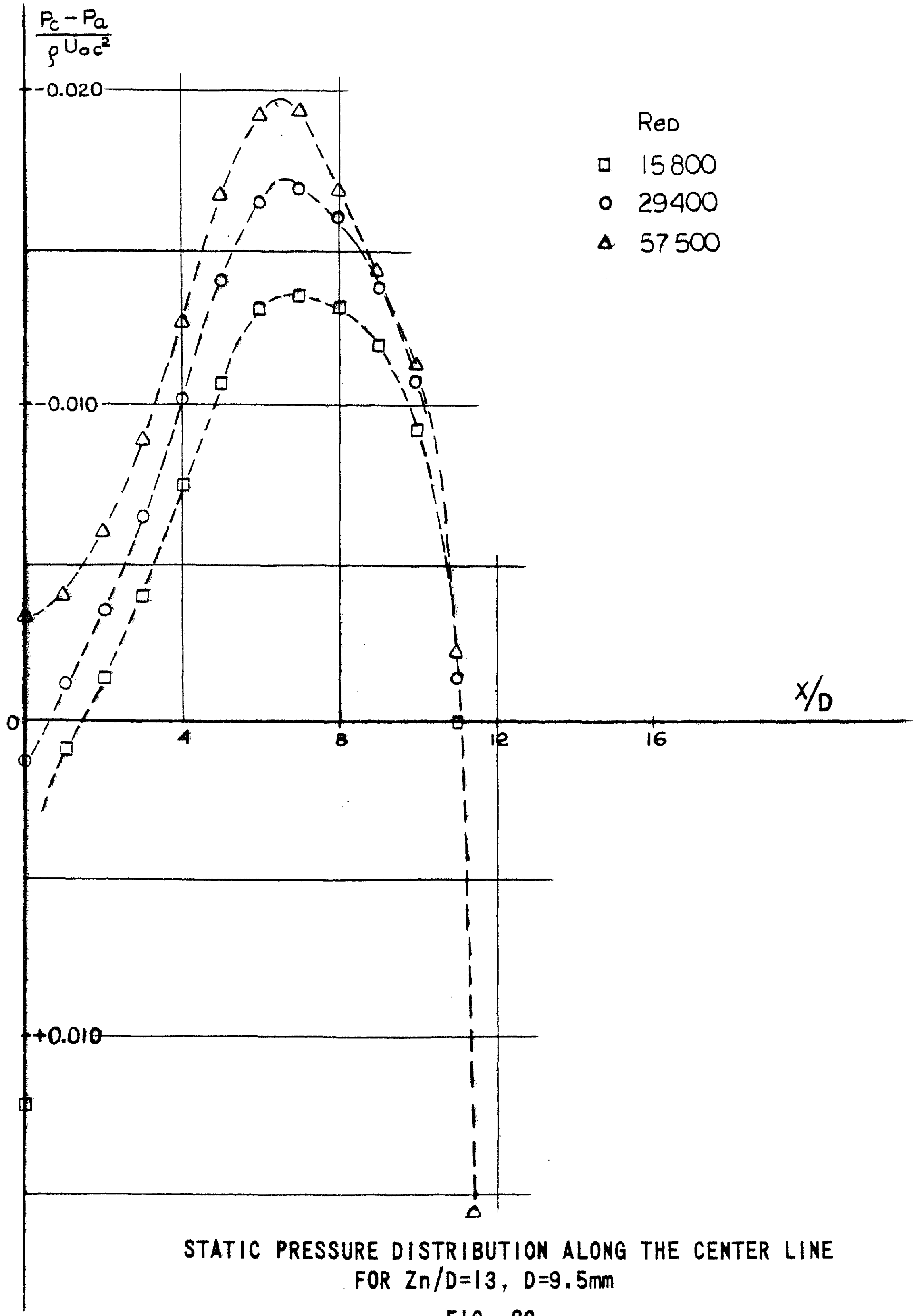

STATIC PRESSURE DISTRIBUTION ALONG THE CENTER LINE FOR Zn/D=13, D=9.5mm

FIG. 20

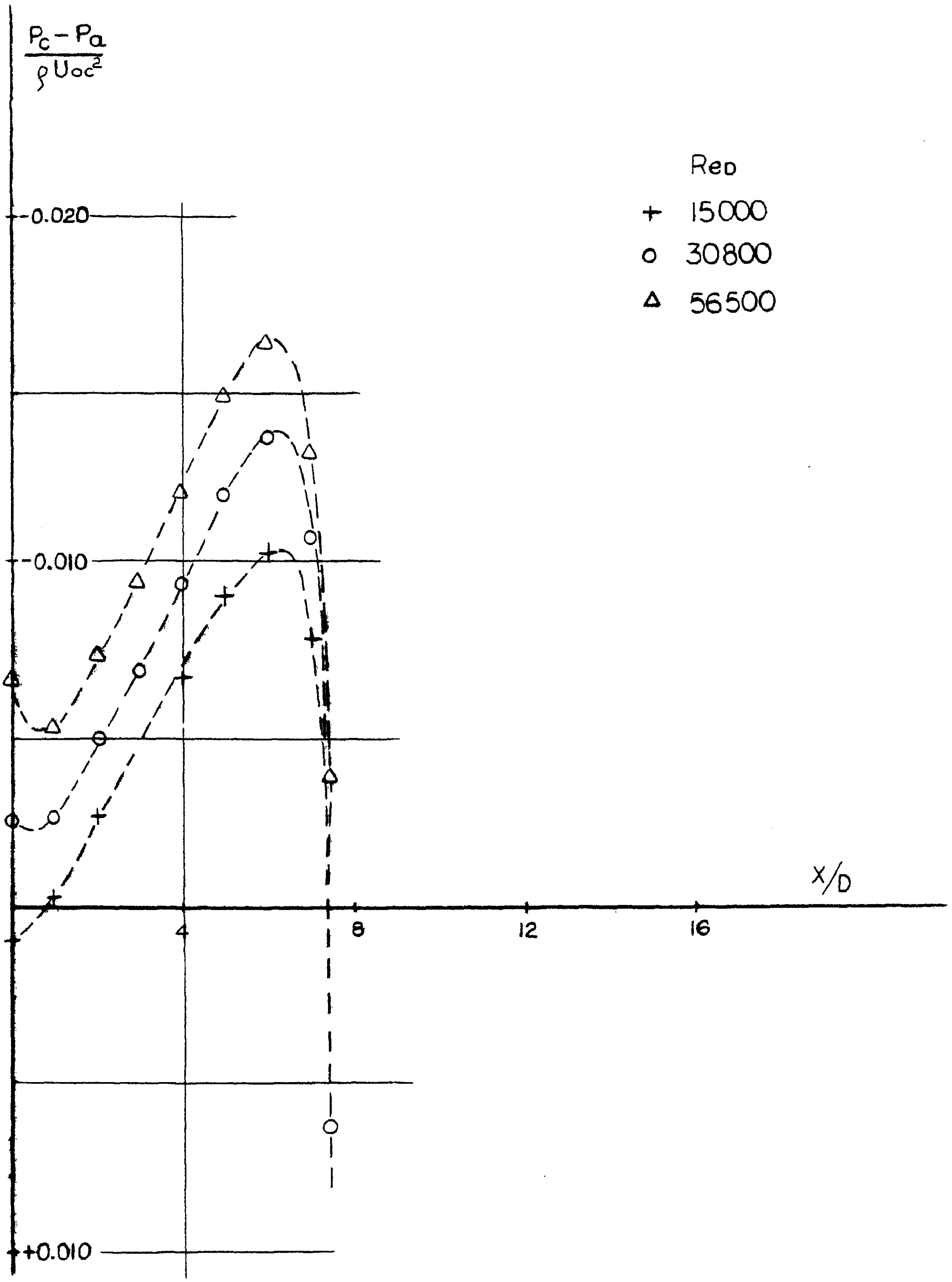

STATIC PRESSURE DISTRIBUTION ALONG THE CENTER LINE FOR Zn/D=9, D=9.5mm

FIG. 21

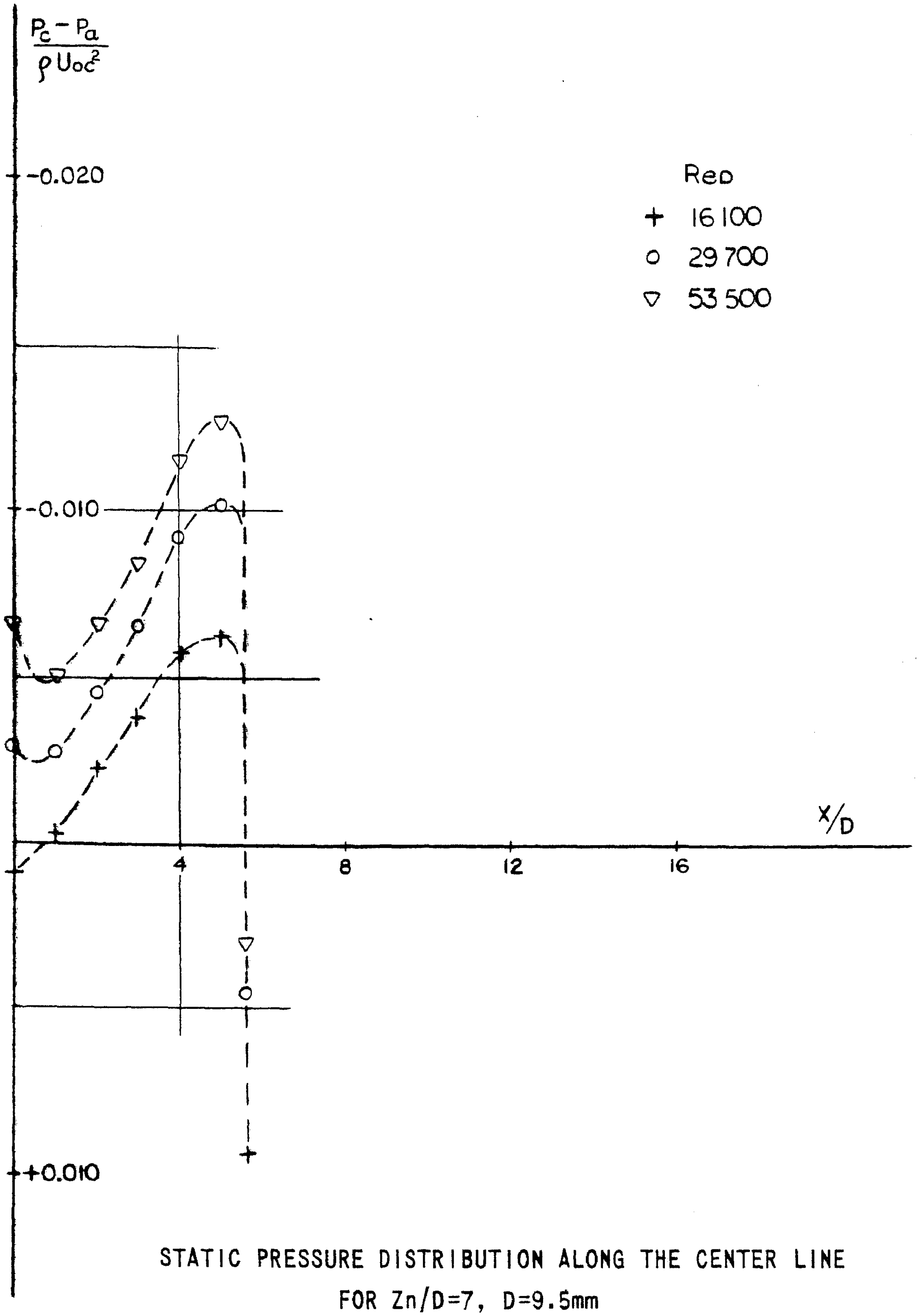

STATIC PRESSURE DISTRIBUTION ALONG THE CENTER LINE FOR Zn/D=7, D=9.5mm

FIG. 22

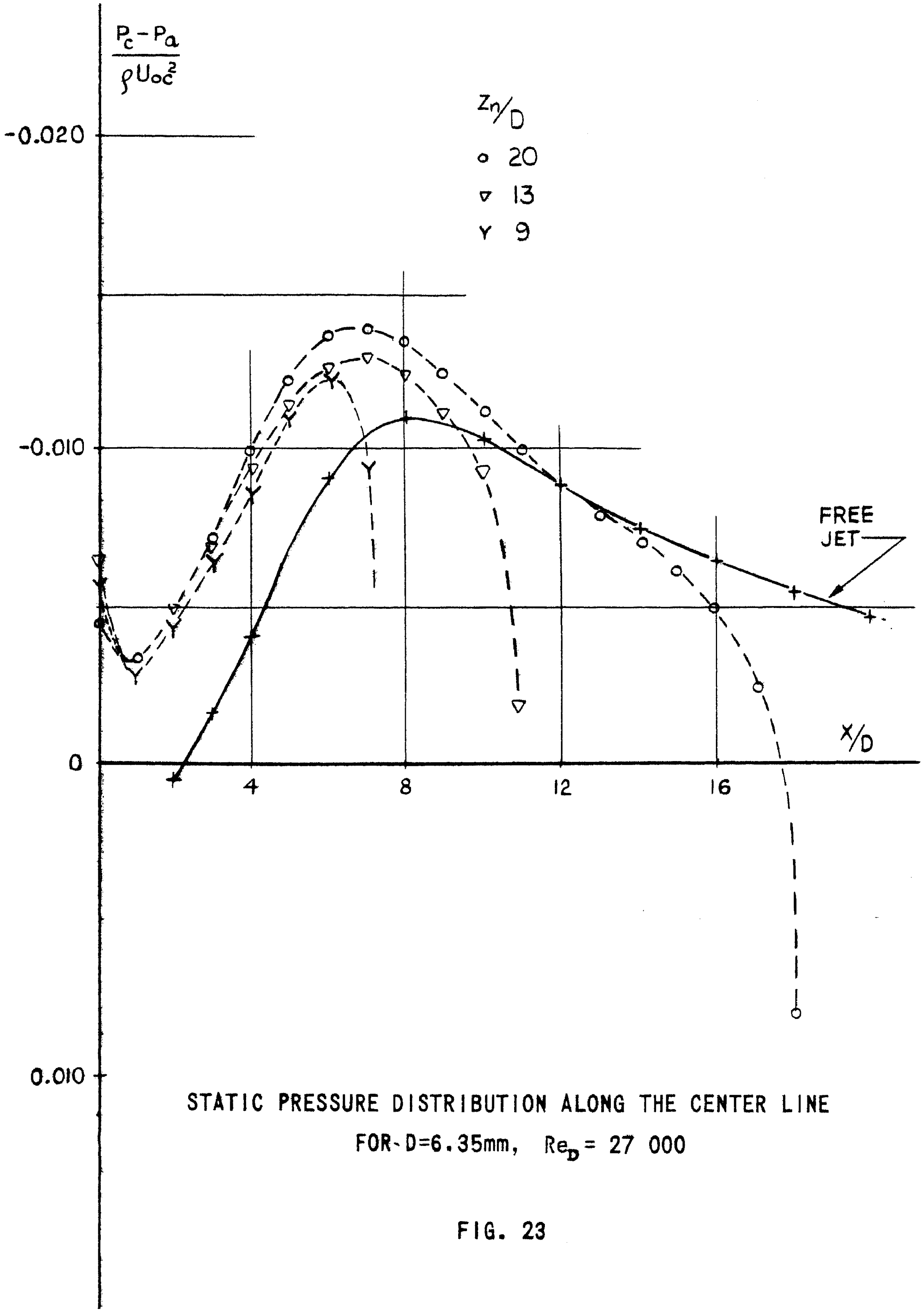

STATIC PRESSURE DISTRIBUTION ALONG THE CENTER LINE FOR D=6.35mm, Re_D = 27 000

FIG. 23

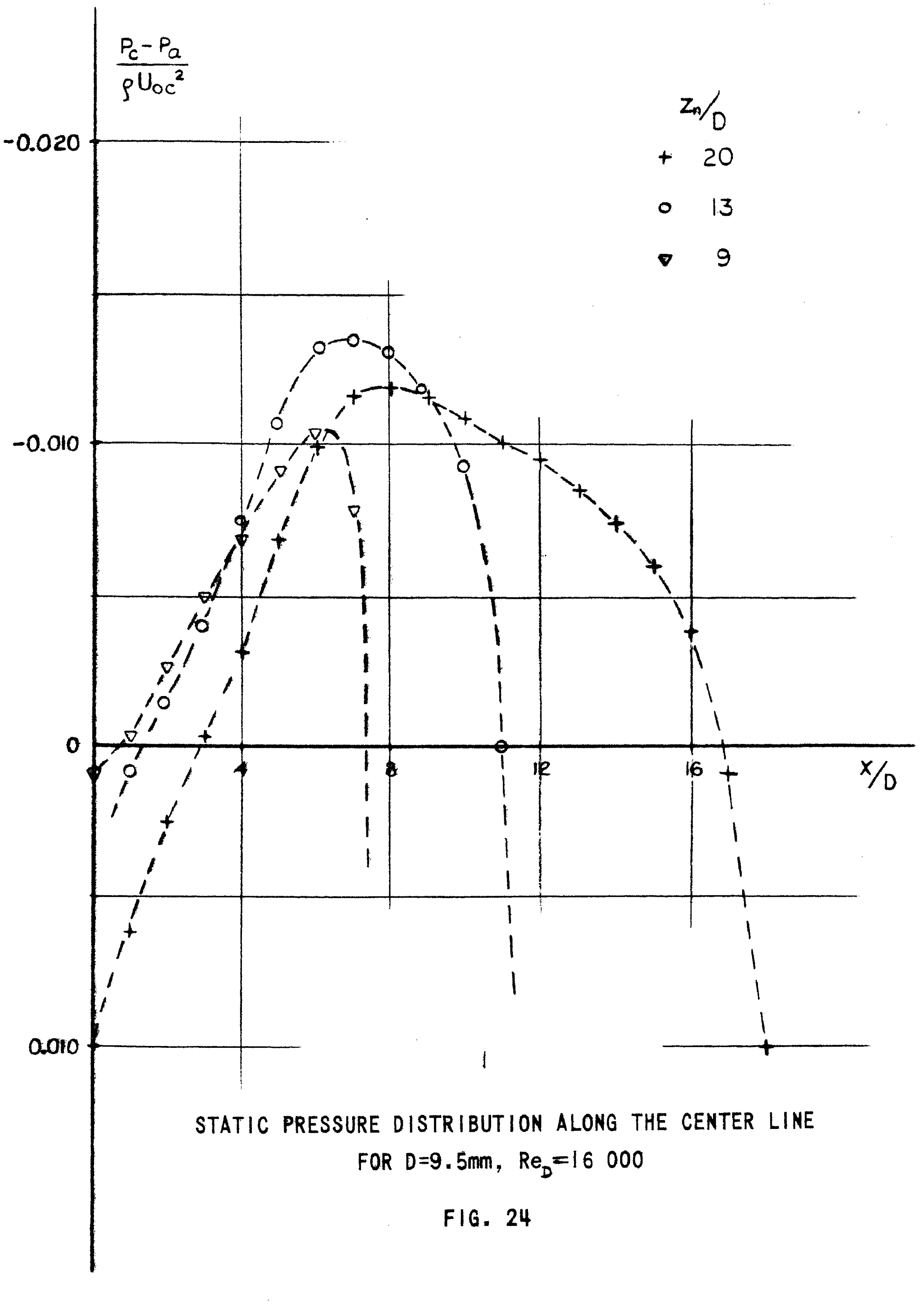

STATIC PRESSURE DISTRIBUTION ALONG THE CENTER LINE
FOR D=9.5mm, Re_D=16 000

FIG. 24

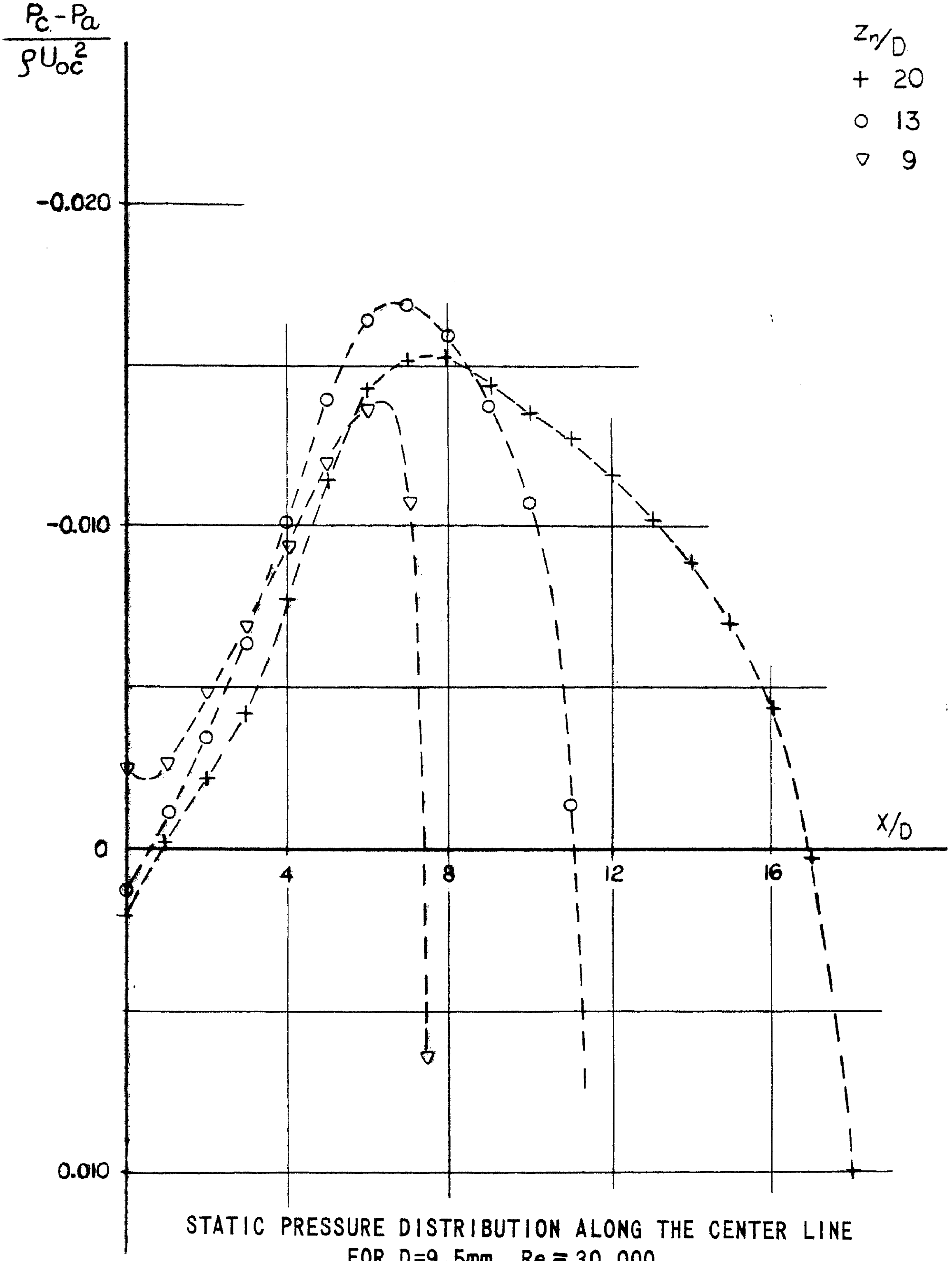

STATIC PRESSURE DISTRIBUTION ALONG THE CENTER LINE FOR D=9.5mm, Re_D= 30 000

FIG. 25

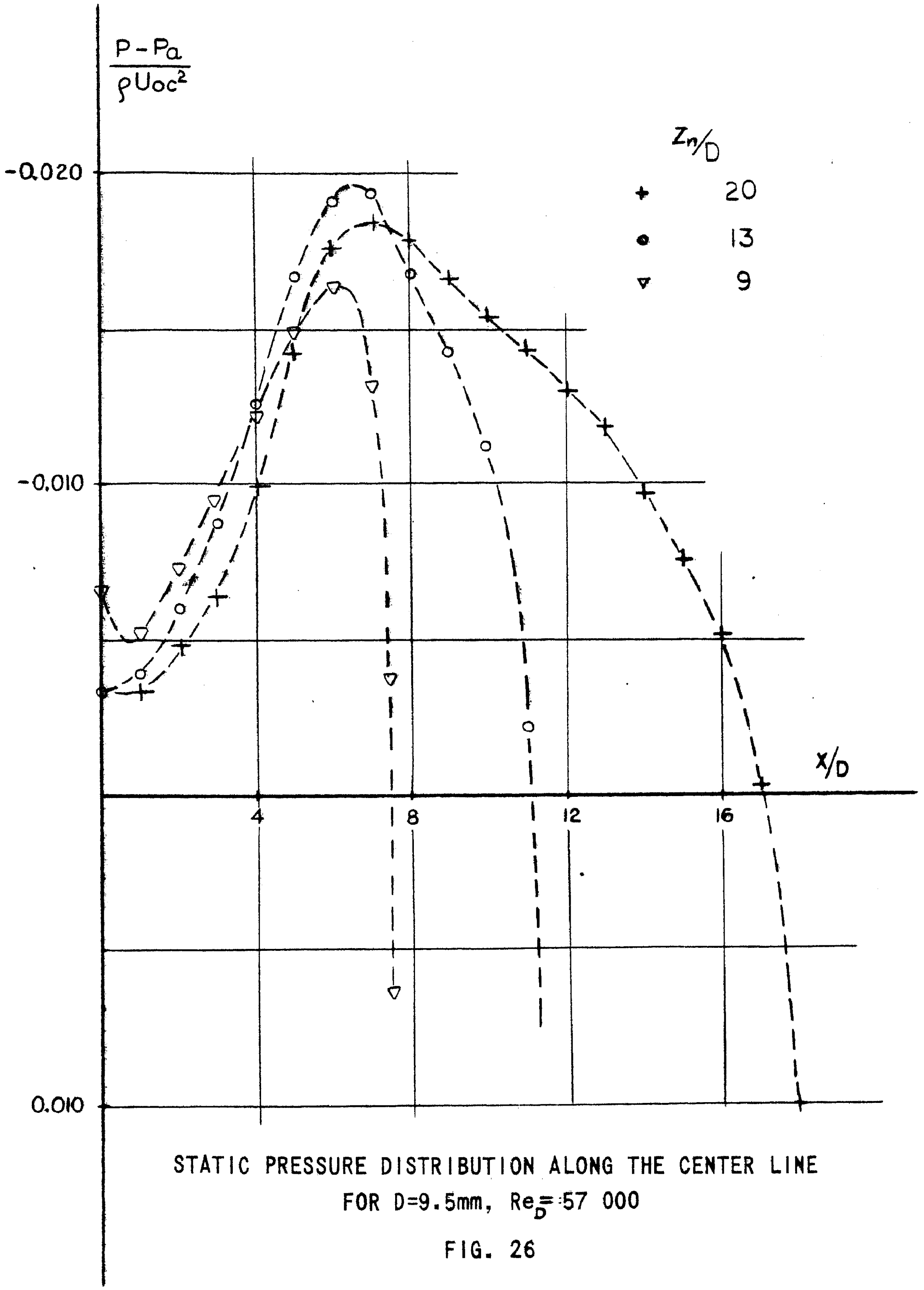

STATIC PRESSURE DISTRIBUTION ALONG THE CENTER LINE
FOR D=9.5mm, Re_D= 57 000

FIG. 26

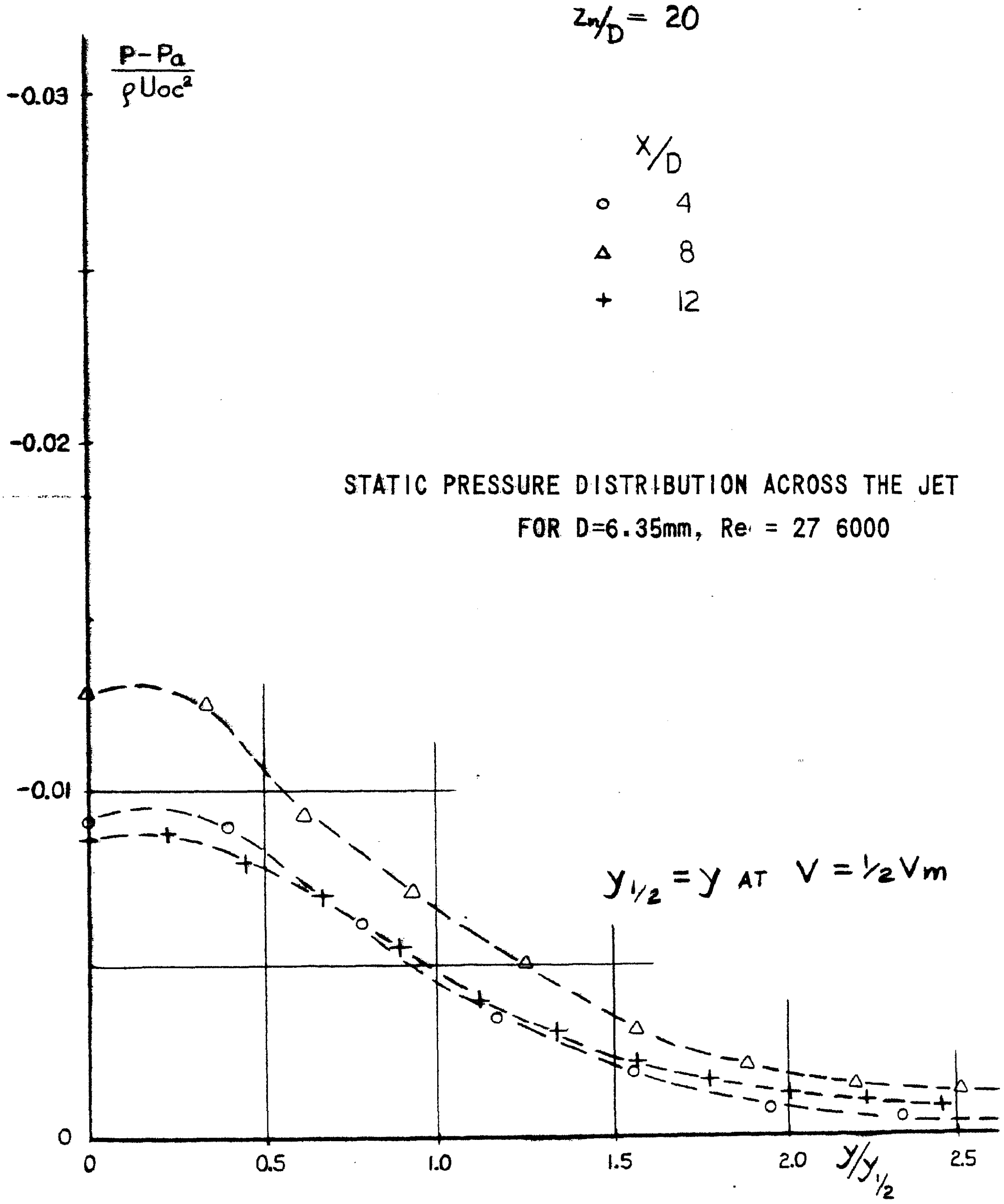

STATIC PRESSURE DISTRIBUTION ACROSS THE JET
FOR D=6.35mm, Re = 27 6000

FIG. 27a

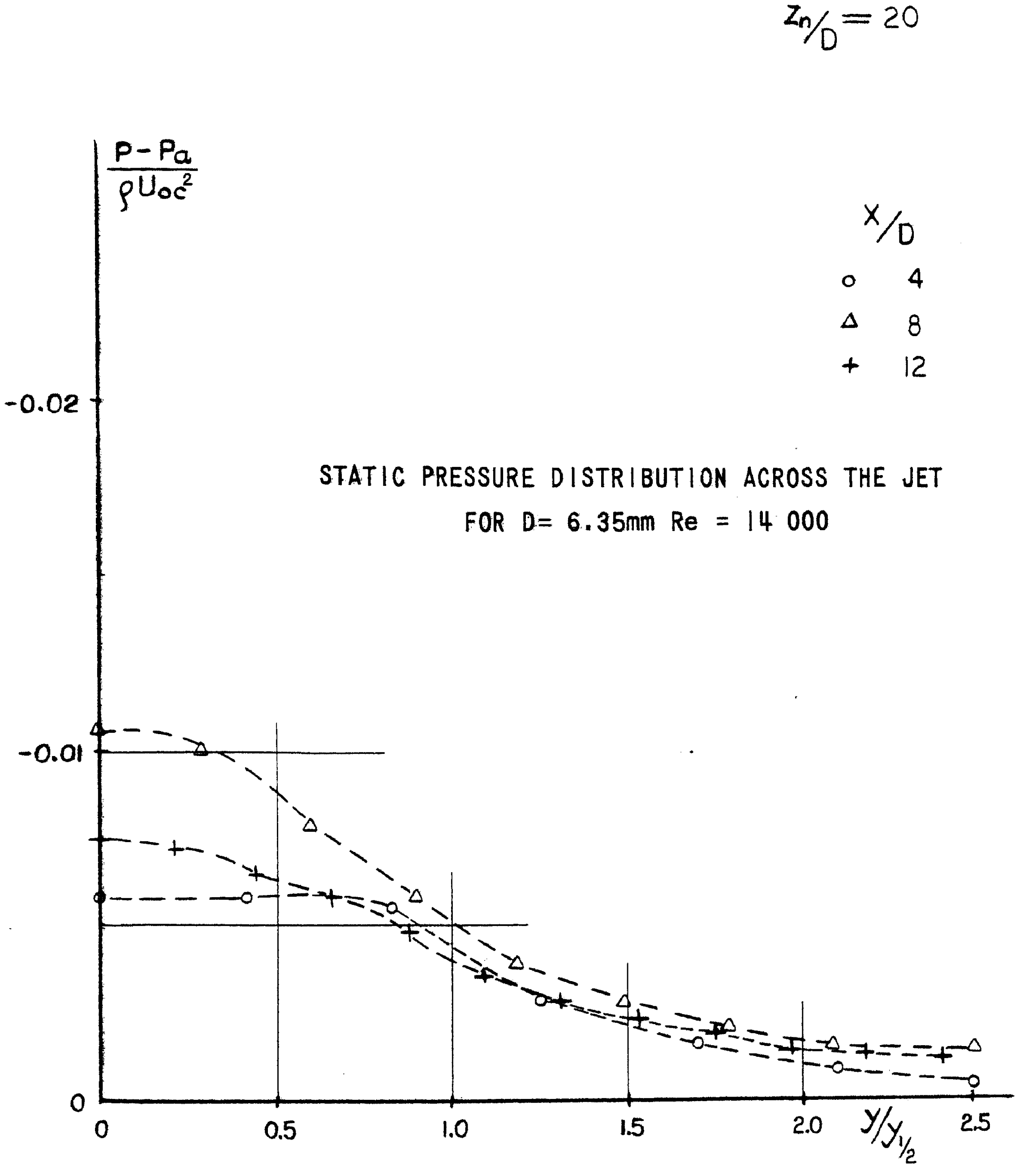

STATIC PRESSURE DISTRIBUTION ACROSS THE JET
FOR D= 6.35mm Re = 14 000

FIG. 27 b

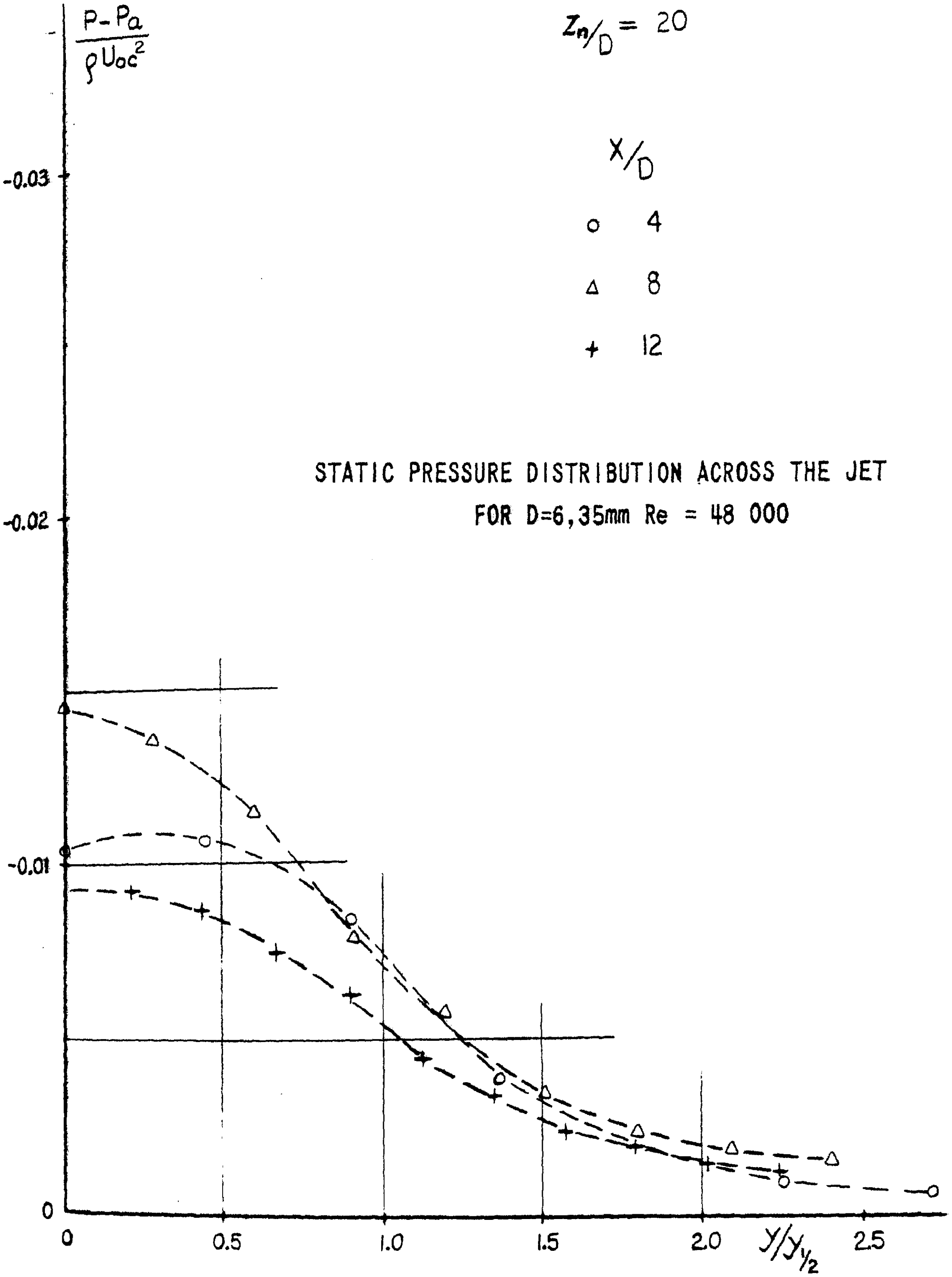

STATIC PRESSURE DISTRIBUTION ACROSS THE JET
FOR D=6,35mm Re = 48 000

FIG. 27c

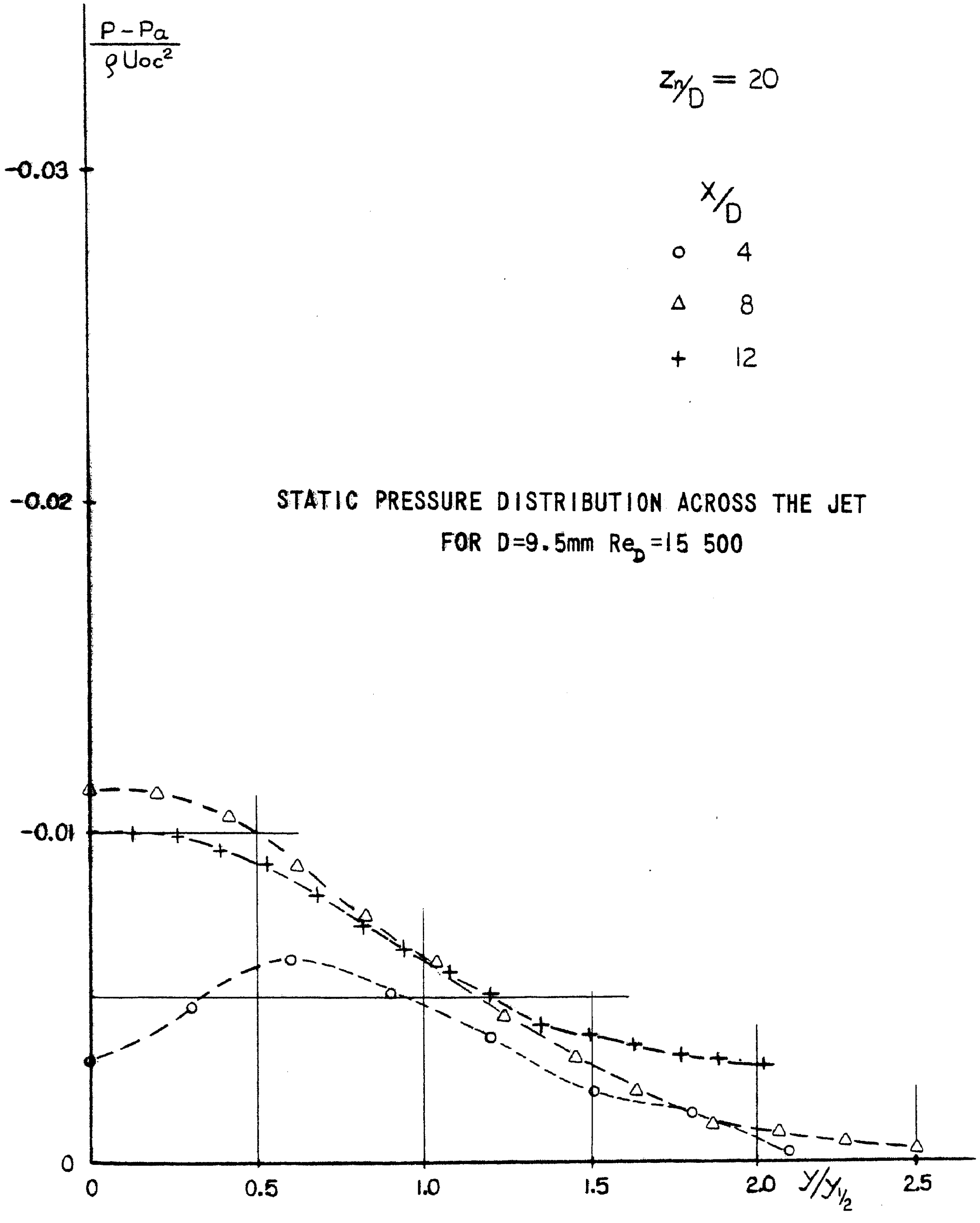
$\frac{P - P_a}{\rho U_{oc}^2}$
$Z_n/D = 20$
X/D
○ 4
△ 8
+ 12
-0.03
-0.02
-0.01
0
0.5
1.0
1.5
2.0
2.5
$y/y_{1/2}$
STATIC PRESSURE DISTRIBUTION ACROSS THE JET
FOR D=9.5mm Re_D=15 500

FIG. 27d

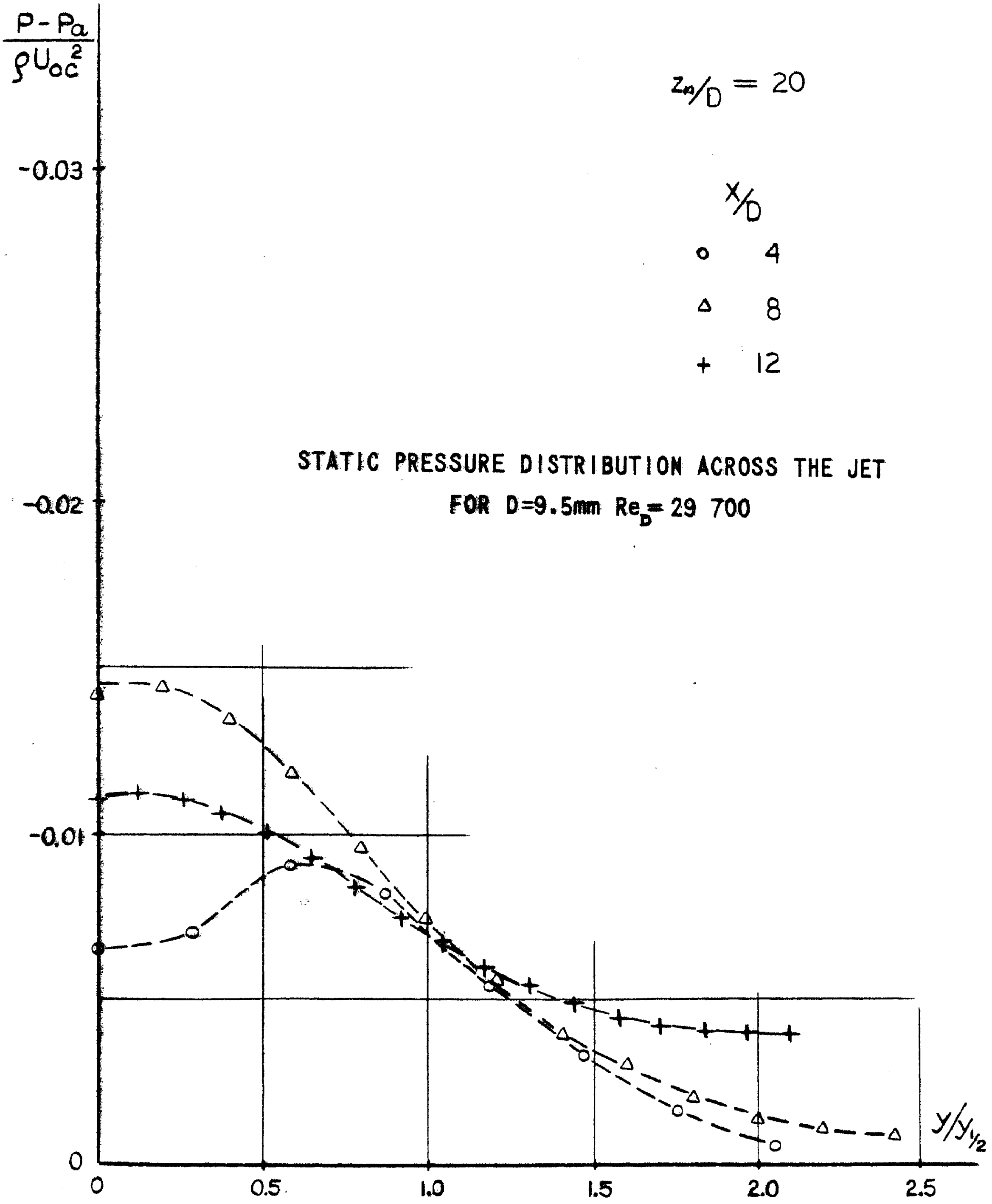

STATIC PRESSURE DISTRIBUTION ACROSS THE JET FOR D=9.5mm $Re_D = 29\ 700$

FIG. 27e

$Z_n/D = 20$

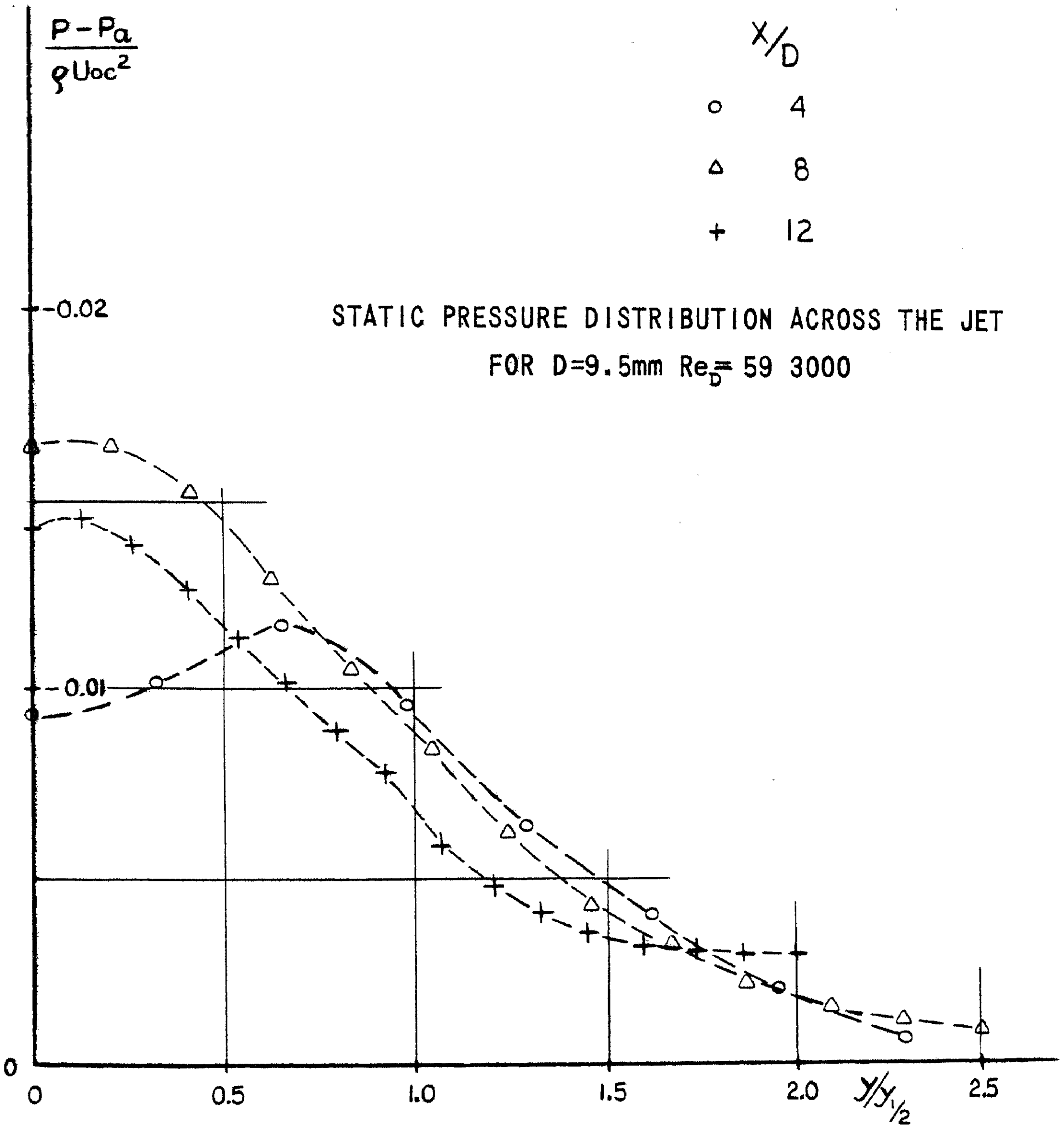

STATIC PRESSURE DISTRIBUTION ACROSS THE JET FOR D=9.5mm Re_D= 59 3000

FIG. 27f

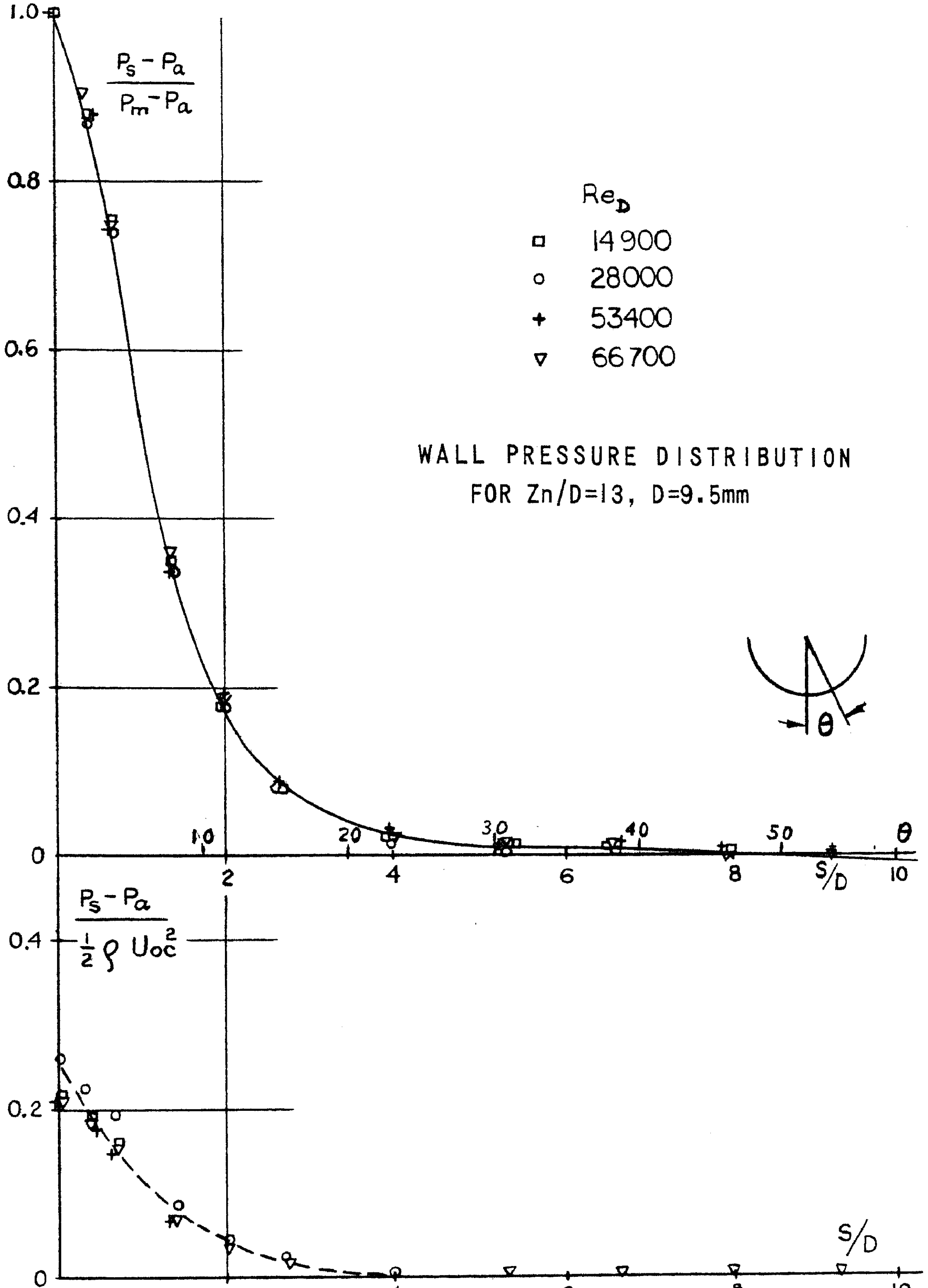
1.0
0.8
0.6
0.4
0.2
0
$\frac{P_s - P_a}{P_m - P_a}$
Re_D
□ 14900
○ 28000
+ 53400
▽ 66700
WALL PRESSURE DISTRIBUTION
FOR Zn/D=13, D=9.5mm
θ
10
20
30
40
50
θ
2
4
6
8
S/D
10
$\frac{P_s - P_a}{\frac{1}{2}\rho U_{oc}^2}$
0.4
0.2
0
S/D
2
4
6
8
10

FIG. 28a

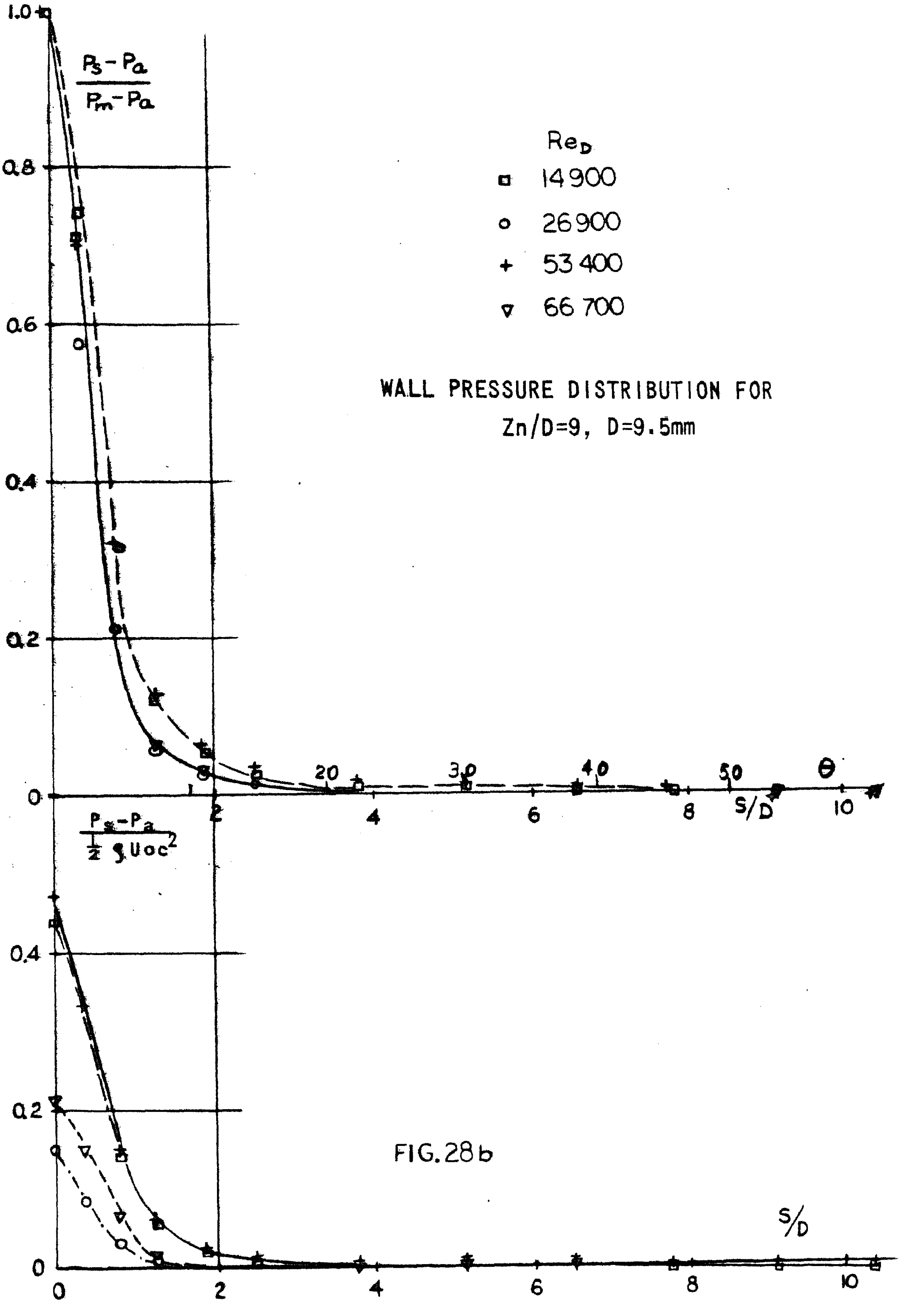
$\frac{P_s - P_a}{P_m - P_a}$
1.0
0.8
0.6
0.4
0.2
0
Re$_D$
□ 14900
○ 26900
+ 53400
▽ 66700
WALL PRESSURE DISTRIBUTION FOR
Zn/D=9, D=9.5mm
20
30
40
50
θ
2
4
6
8
S/D
10
$\frac{P_s - P_a}{\frac{1}{2}\rho U_{oc}^2}$
0.4
0.2
0
S/D
0
2
4
6
8
10

FIG. 28b

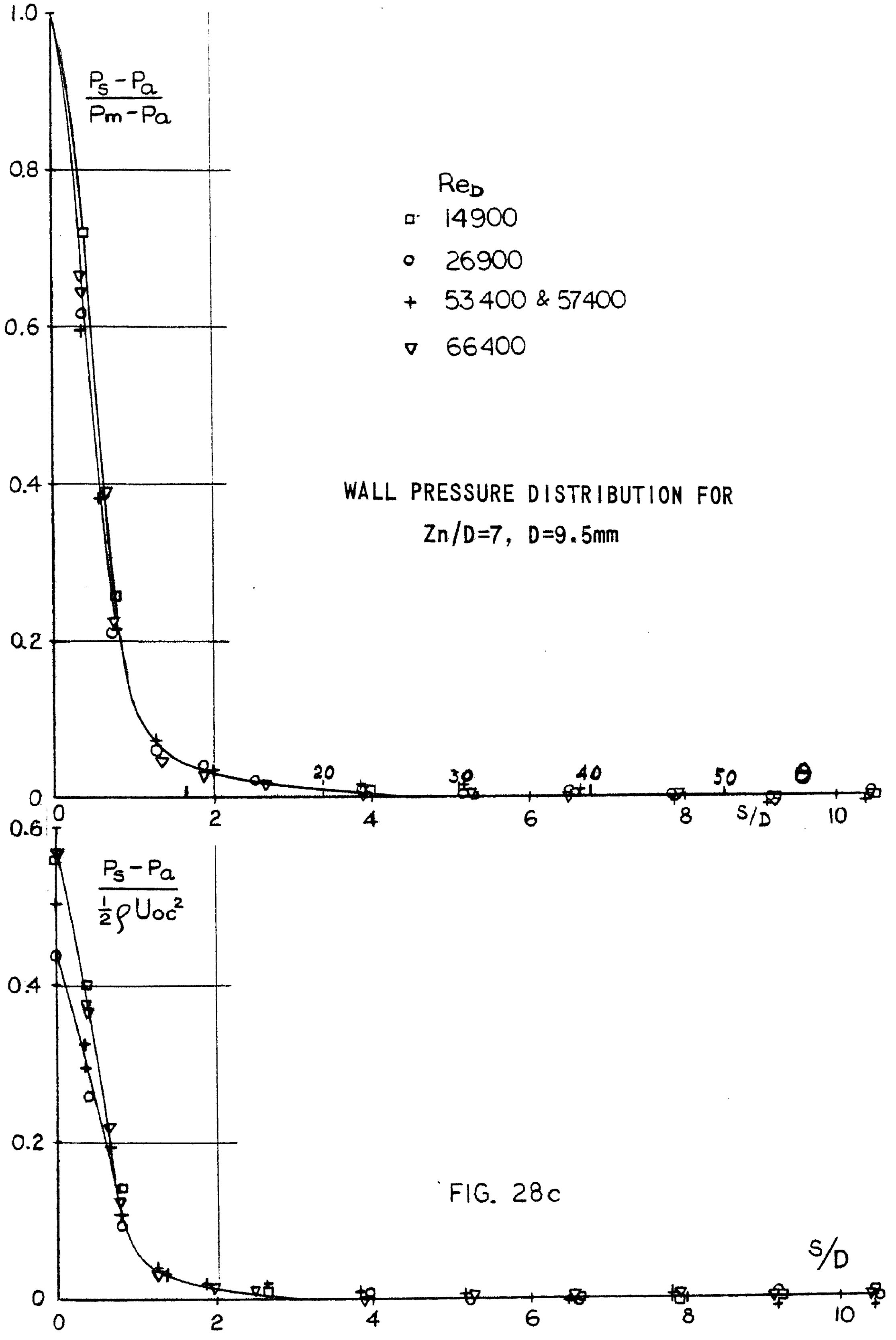

WALL PRESSURE DISTRIBUTION FOR Zn/D=7, D=9.5mm

FIG. 28c

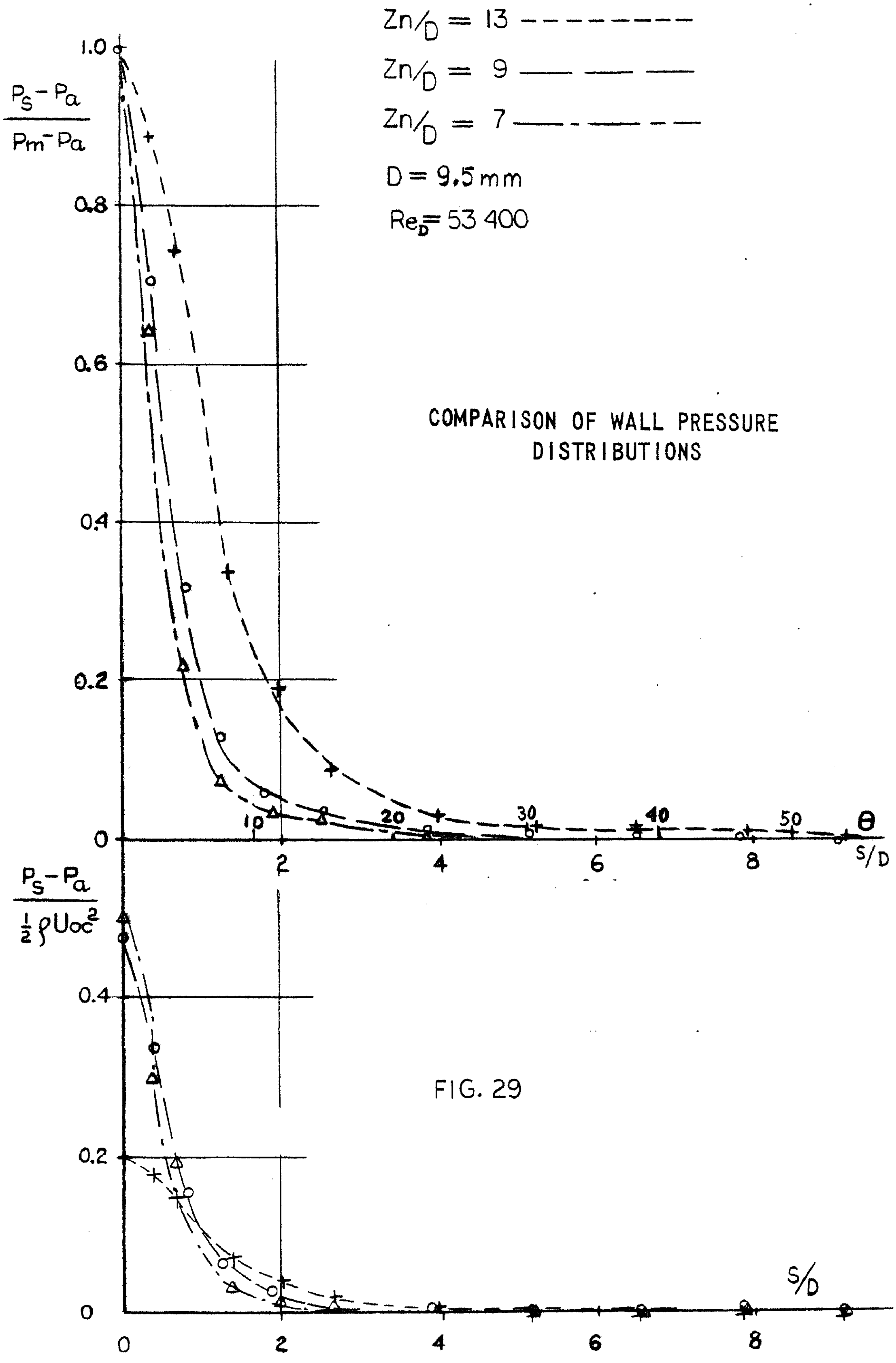

COMPARISON OF WALL PRESSURE DISTRIBUTIONS

FIG. 29

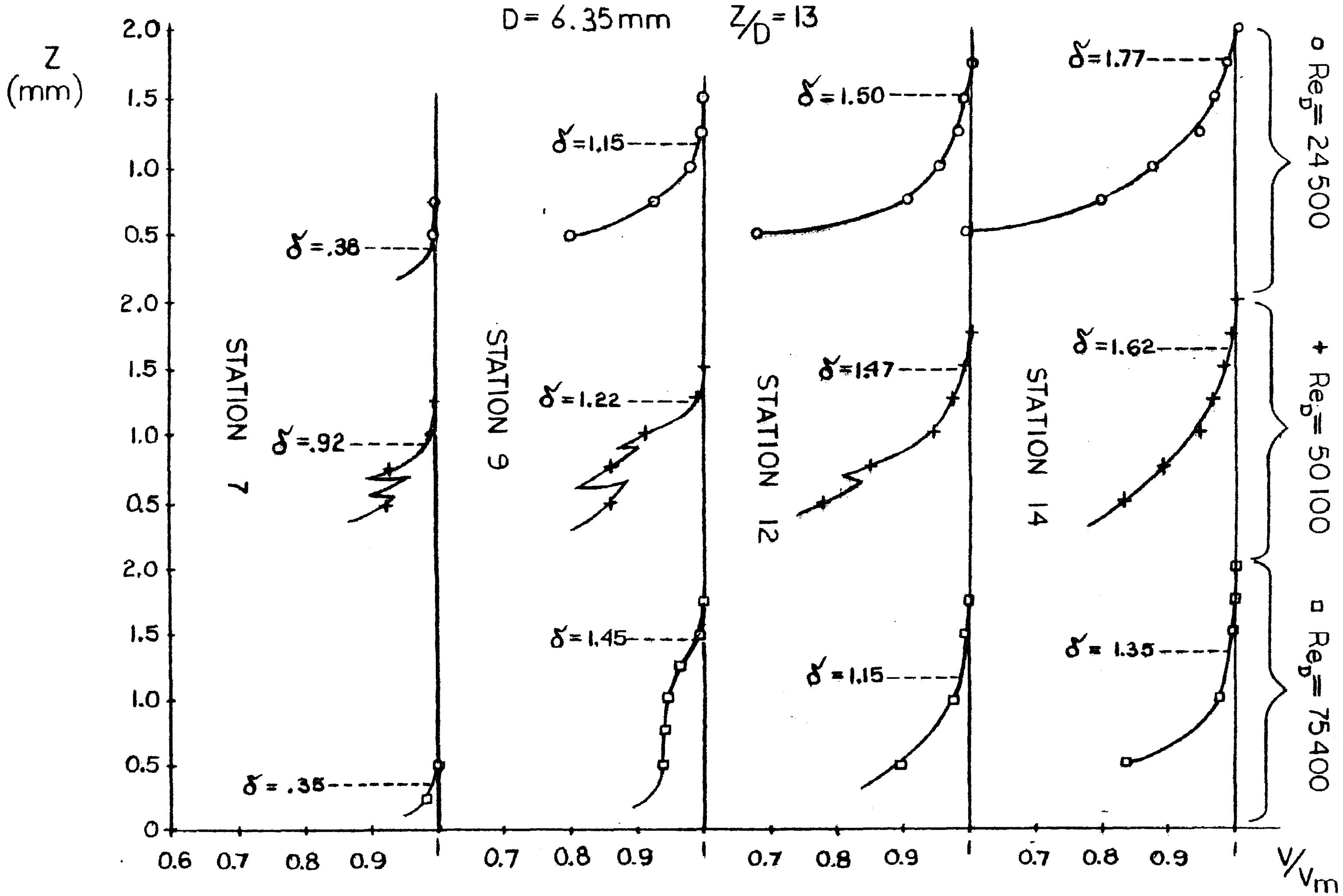

FIG.30 DETERMINATION OF BOUNDARY LAYER THICKNESS

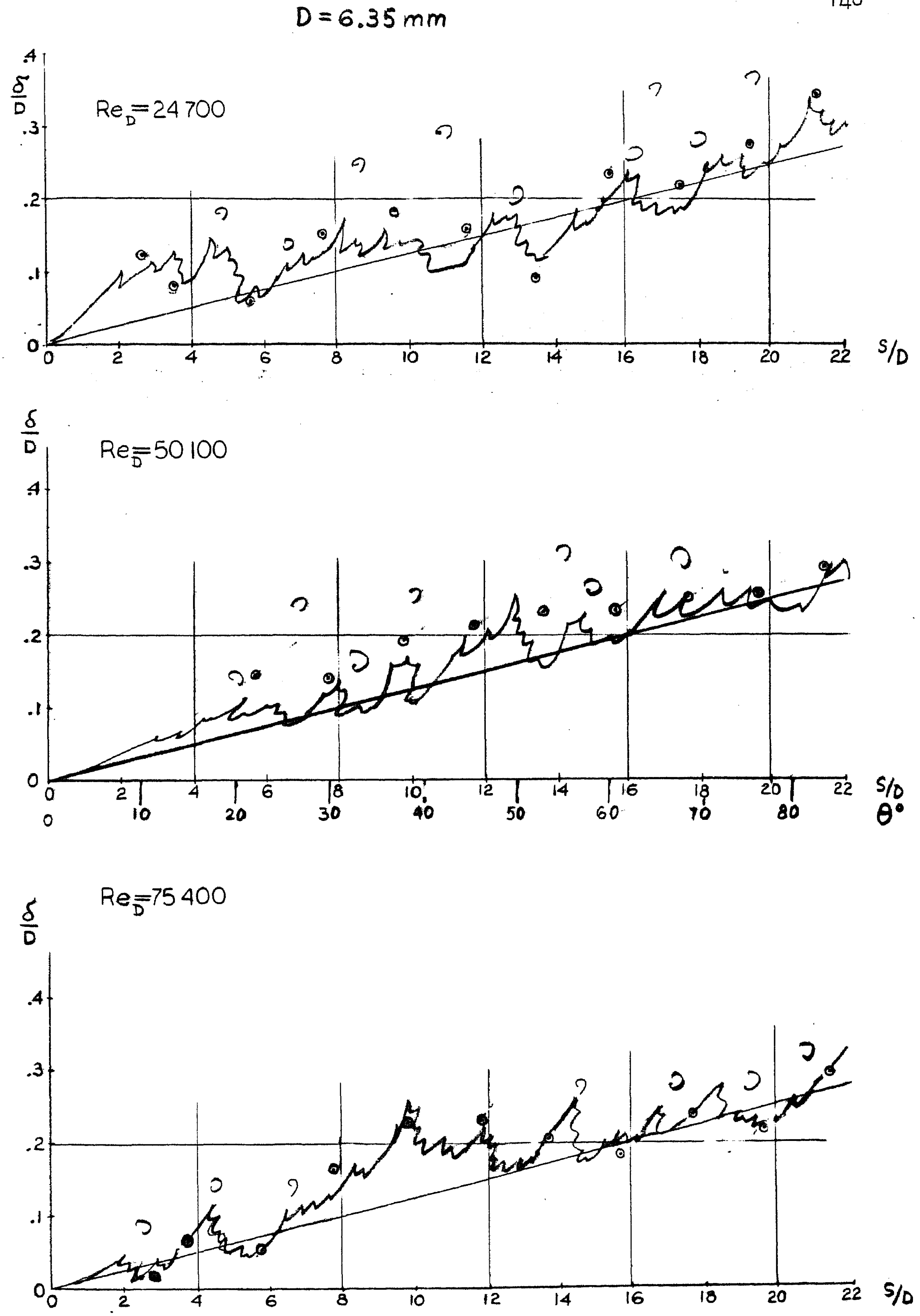

FIG.31a BOUNDARY LAYER THICKNESS FOR Zn/D=1·3

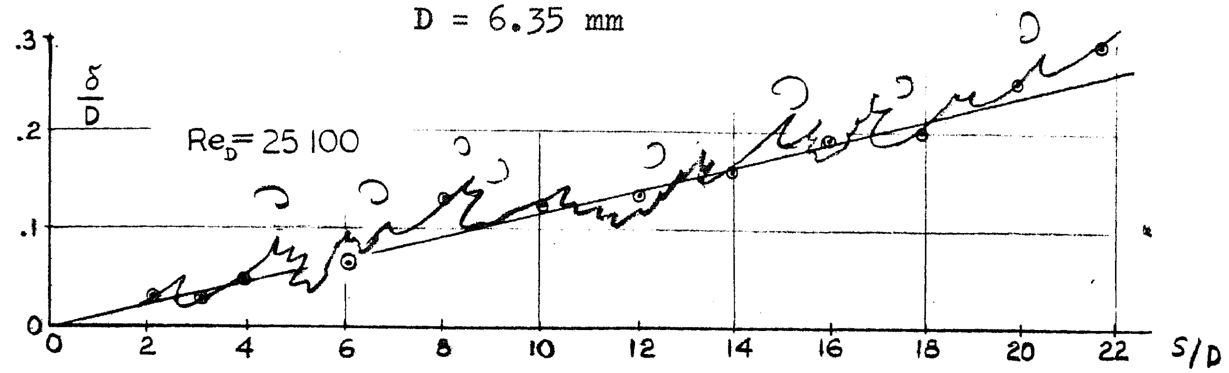

Note: The jagged appearence of the curves representing boundary layer thickness fluctuation has been determined in a special study. See e.g. A. A. Townsend, "The Structure of Turbulent Shear Flow", 1956, concerning representation of the edge of a turbulent jet.

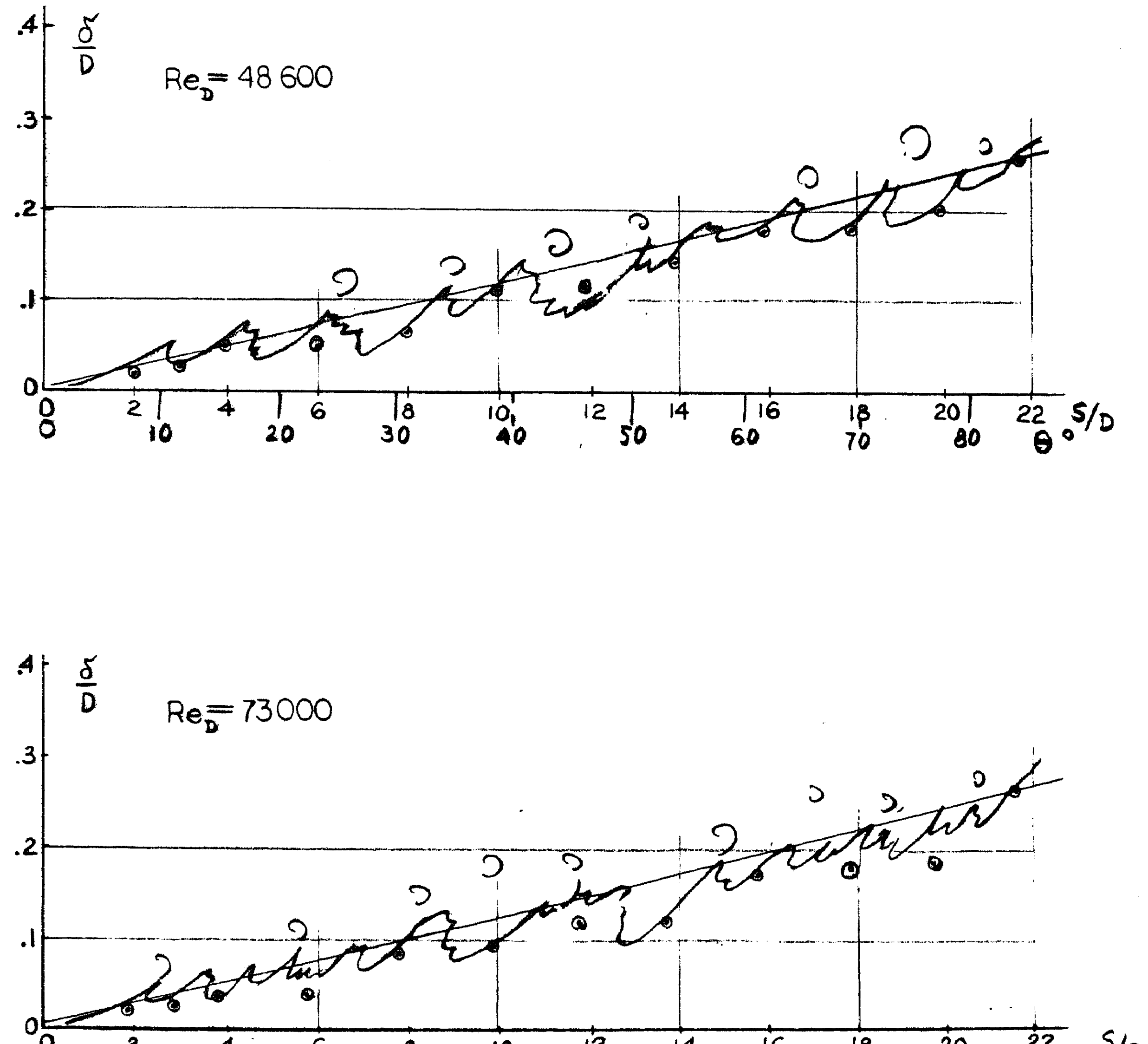

FIG. 31b BOUNDARY LAYER THICKNESS FOR Zn/D=9

D = 6.35mm

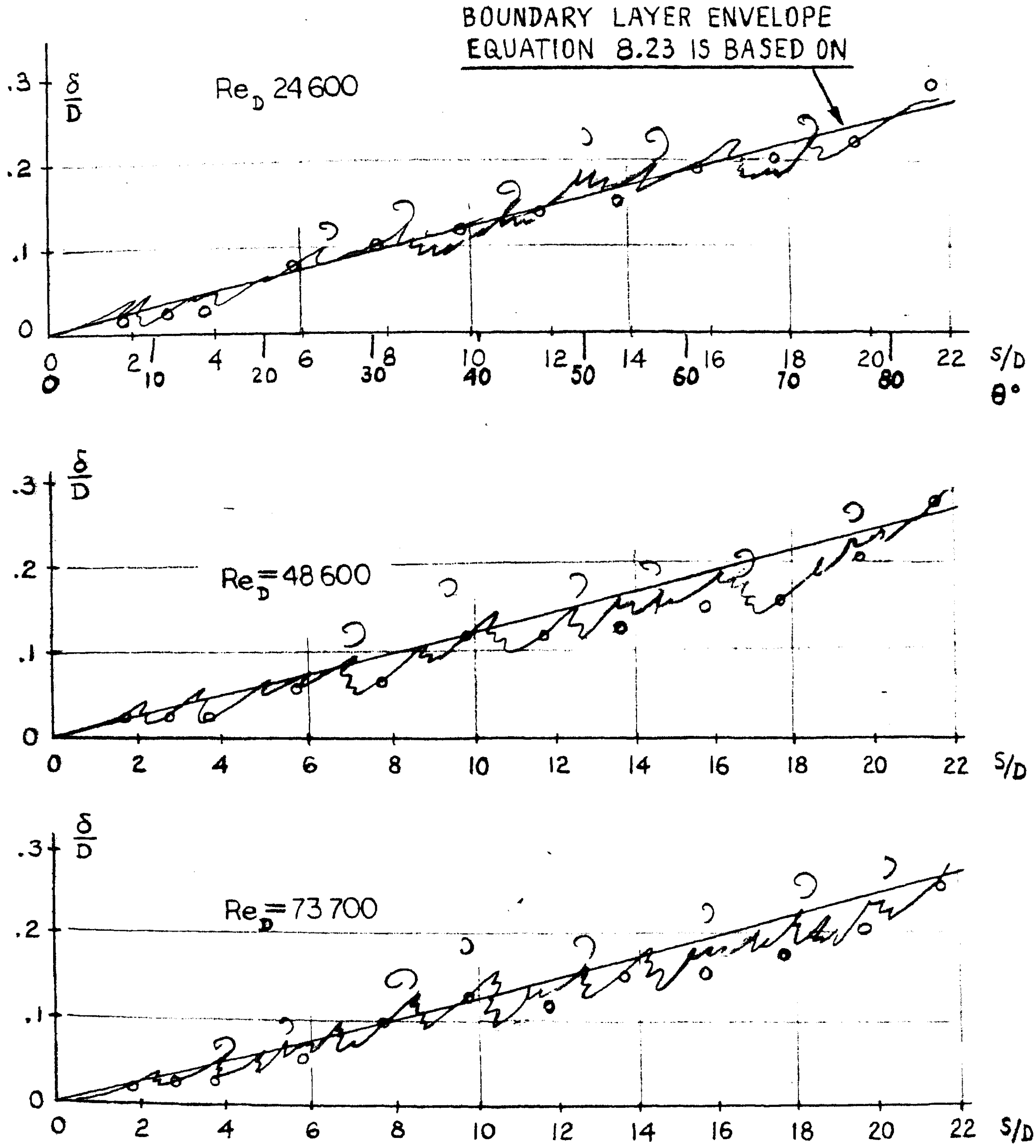

FIG. 31c BOUNDARY LAYER THICKNESS FOR Zn/D=7

D = 6.35 mm

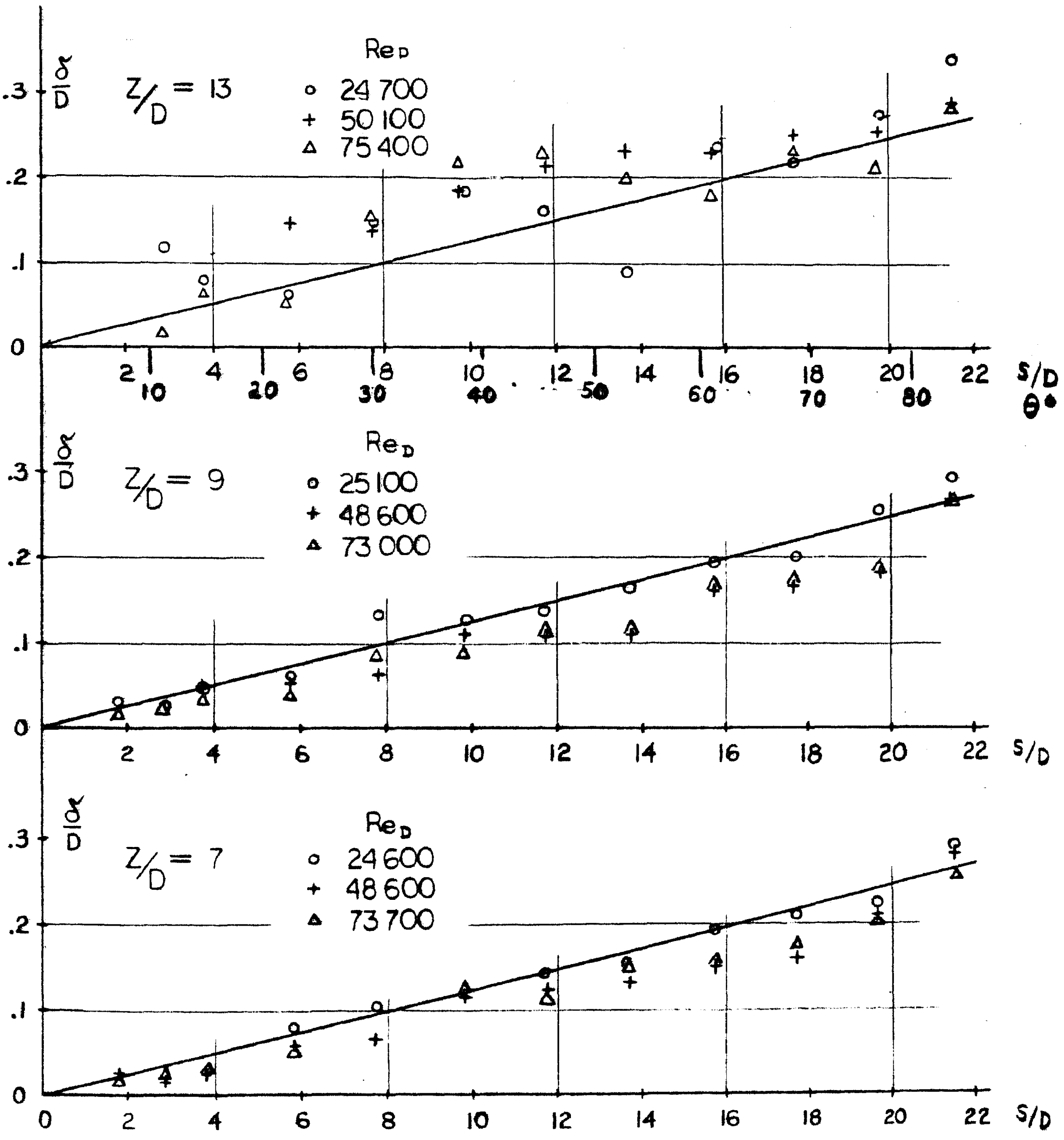

FIG. 32
DIMENSIONLESS BOUNDARY LAYER THICKNESS

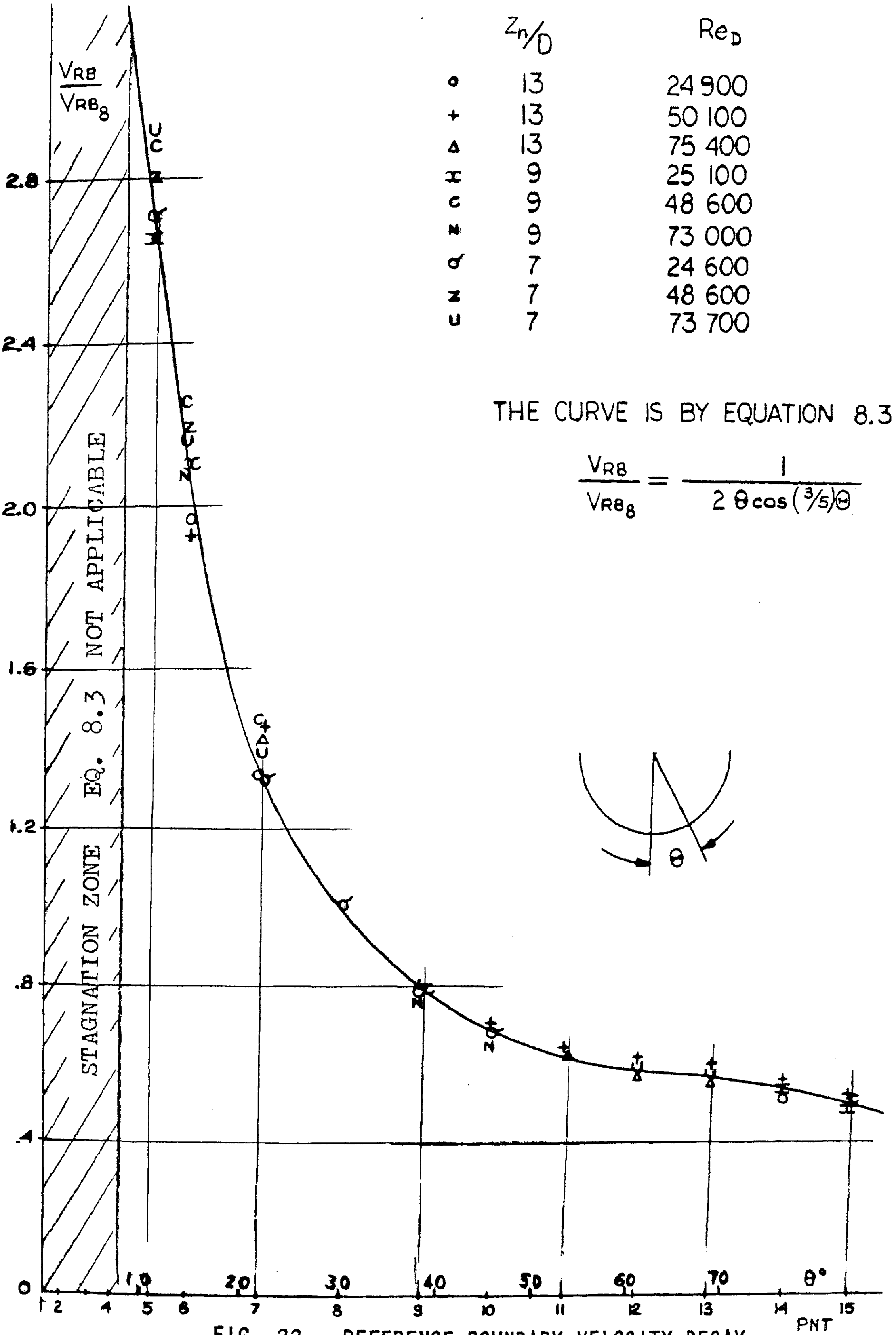

FIG. 33 REFERENCE BOUNDARY VELOCITY DECAY

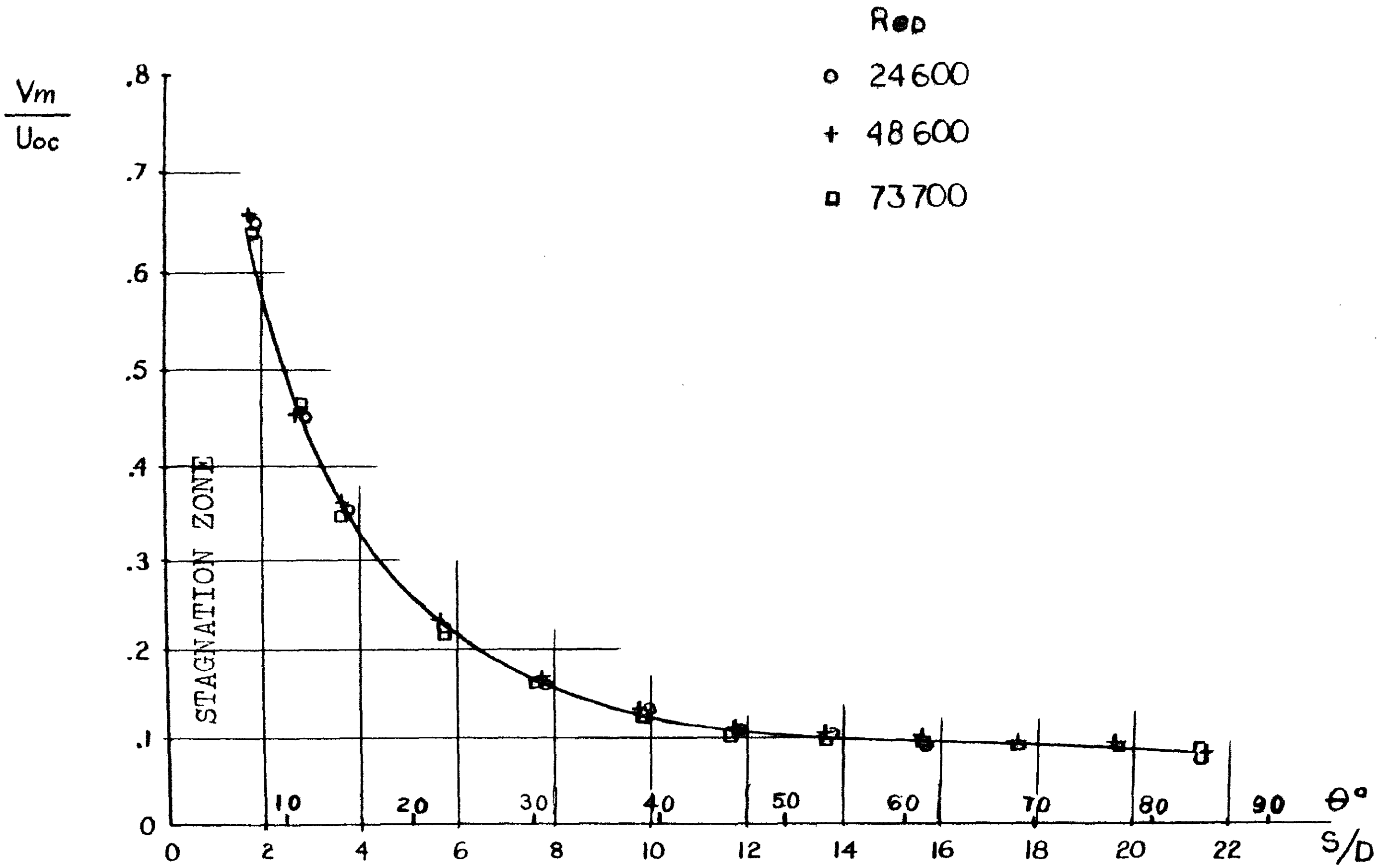

MAXIMUM VELOCITY DECAY IN THE WALL JET
FOR Zn/D=7, D=6.35mm

FIG. 33a

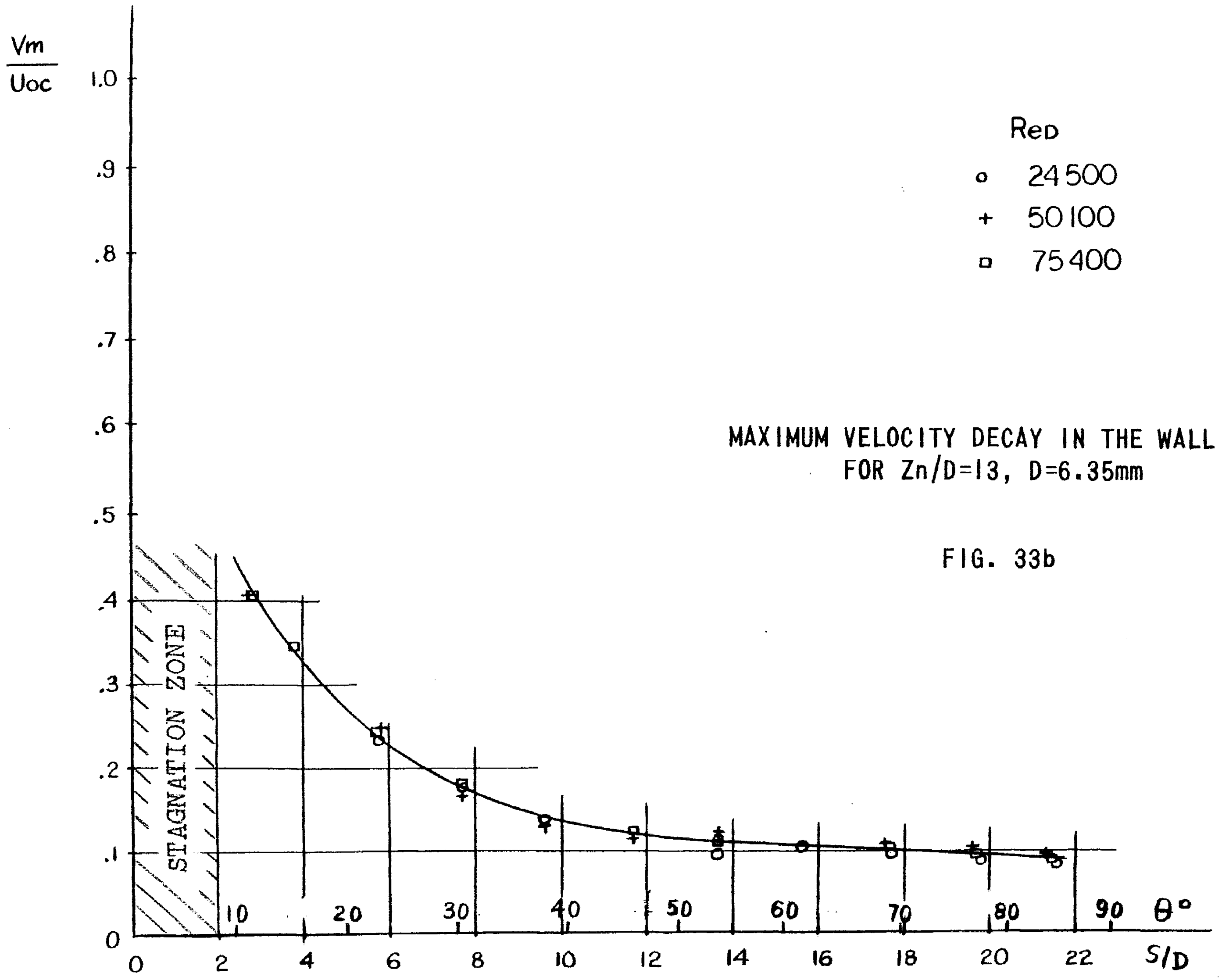

MAXIMUM VELOCITY DECAY IN THE WALL JET
FOR Zn/D=13, D=6.35mm

FIG. 33b

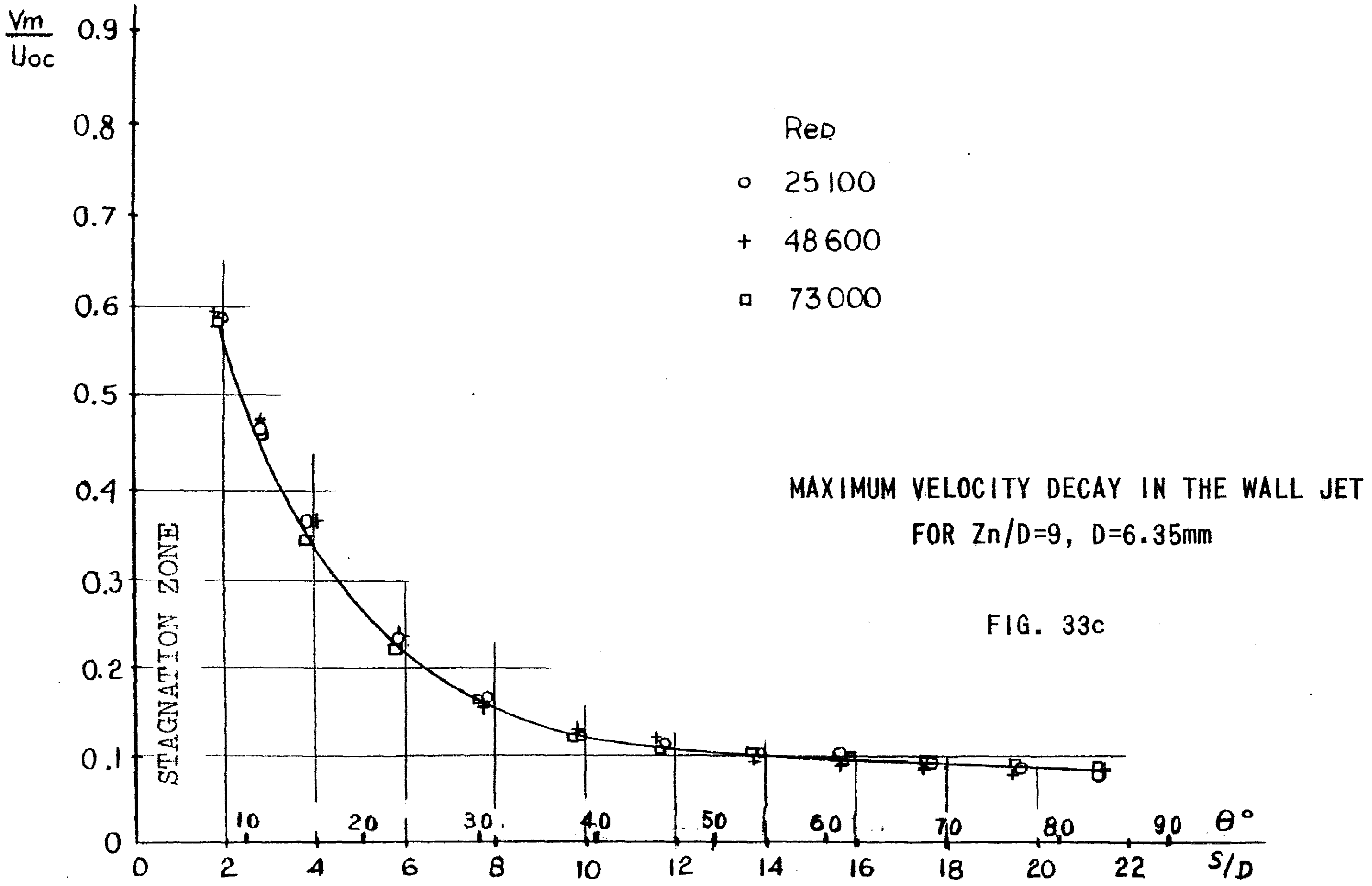

MAXIMUM VELOCITY DECAY IN THE WALL JET FOR Zn/D=9, D=6.35mm

FIG. 33c

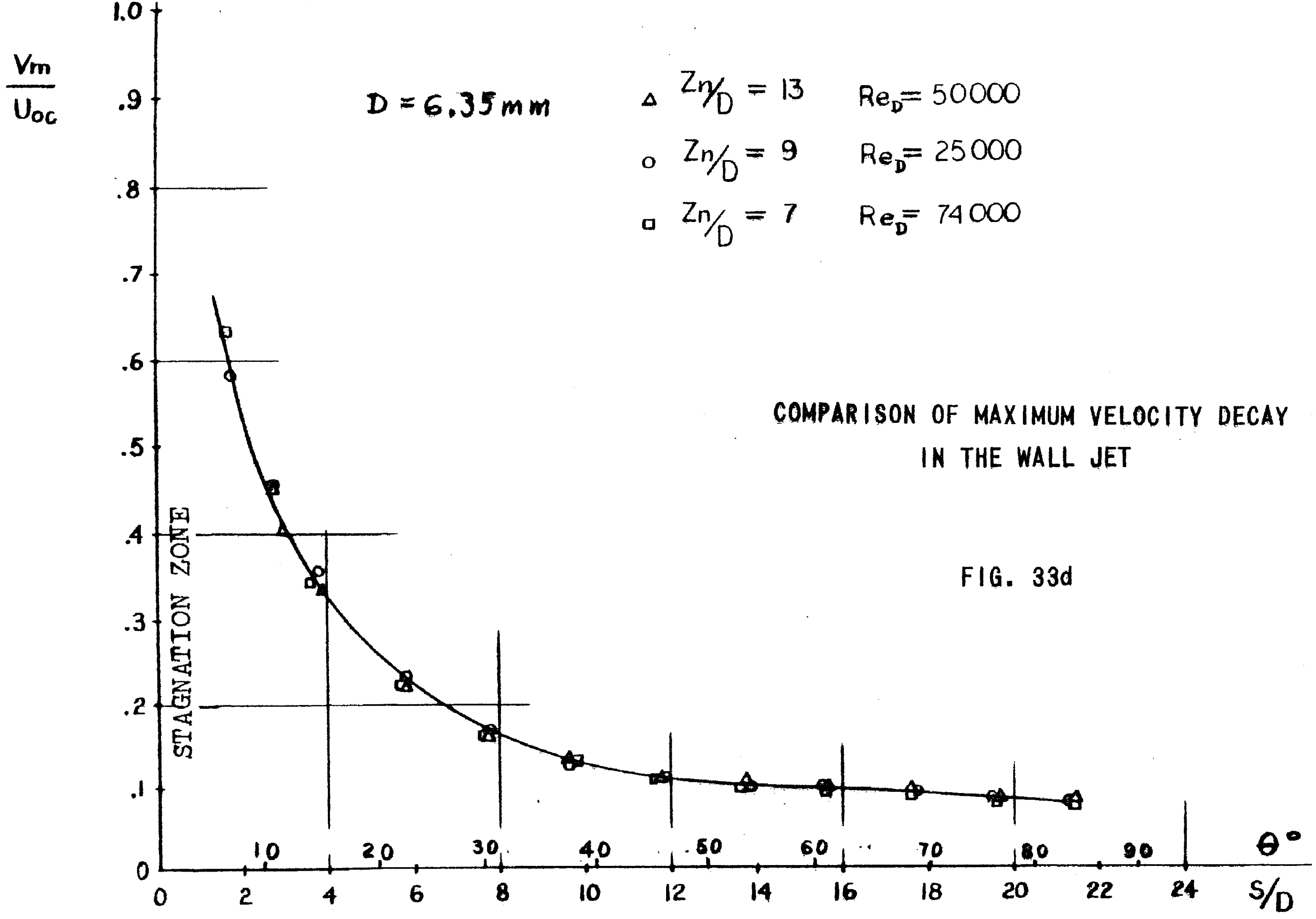

COMPARISON OF MAXIMUM VELOCITY DECAY IN THE WALL JET

FIG. 33d

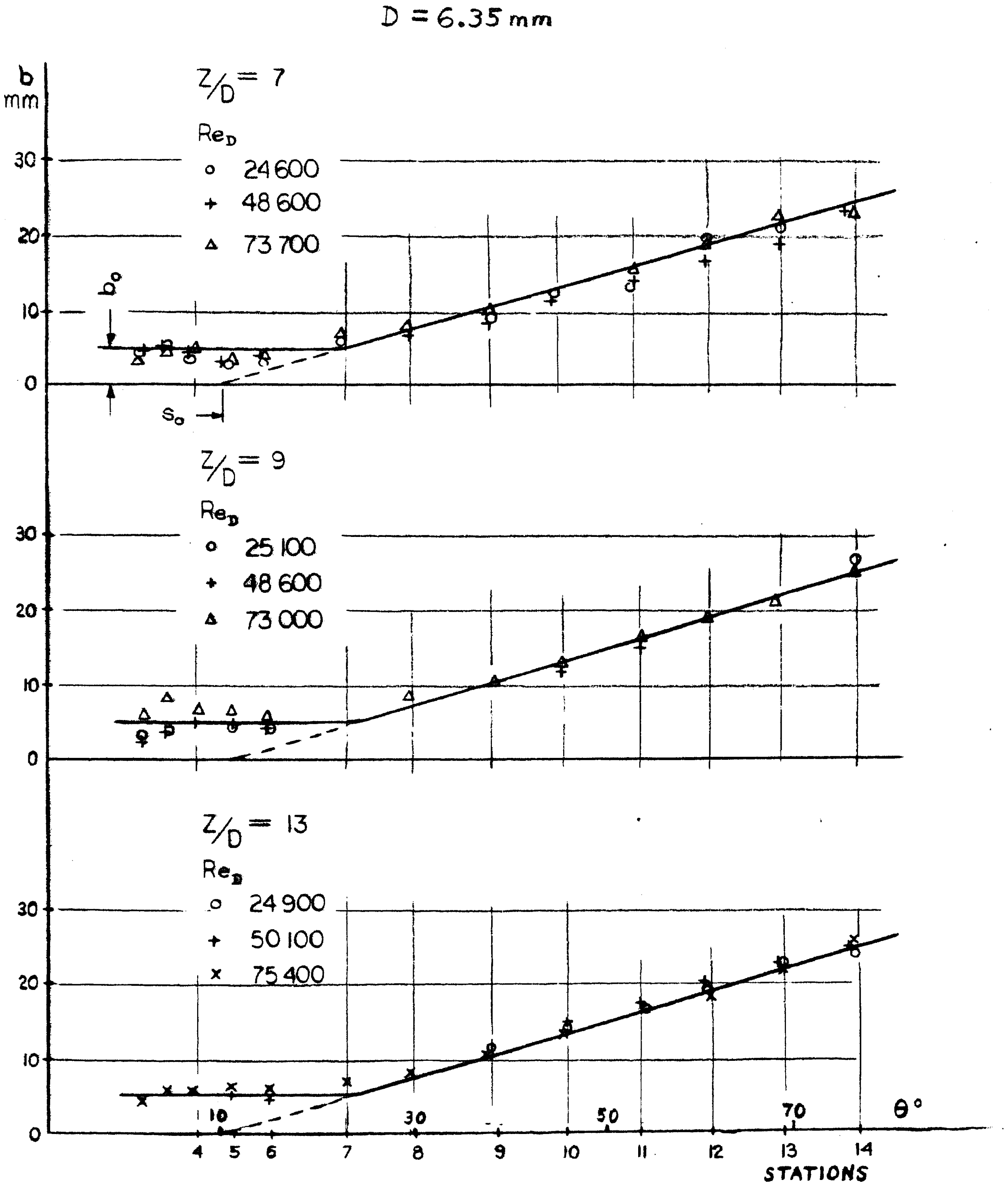

FIG. 34

WALL JET WIDTH

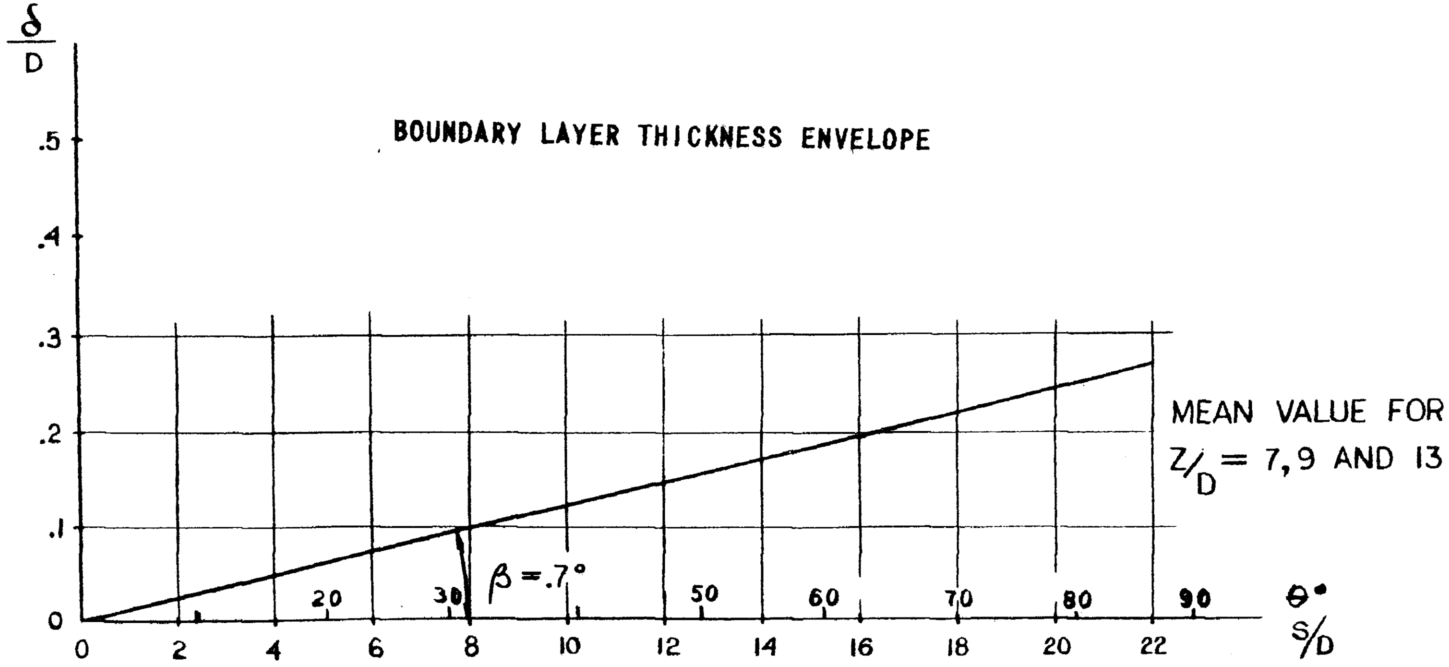

δ/D
.5
.4
.3
.2
.1
0
BOUNDARY LAYER THICKNESS ENVELOPE
MEAN VALUE FOR
Z/D = 7, 9 AND 13
β = .7°
20
30
50
60
70
80
90
θ°
0
2
4
6
8
10
12
14
16
18
20
22
S/D

FIG. 35

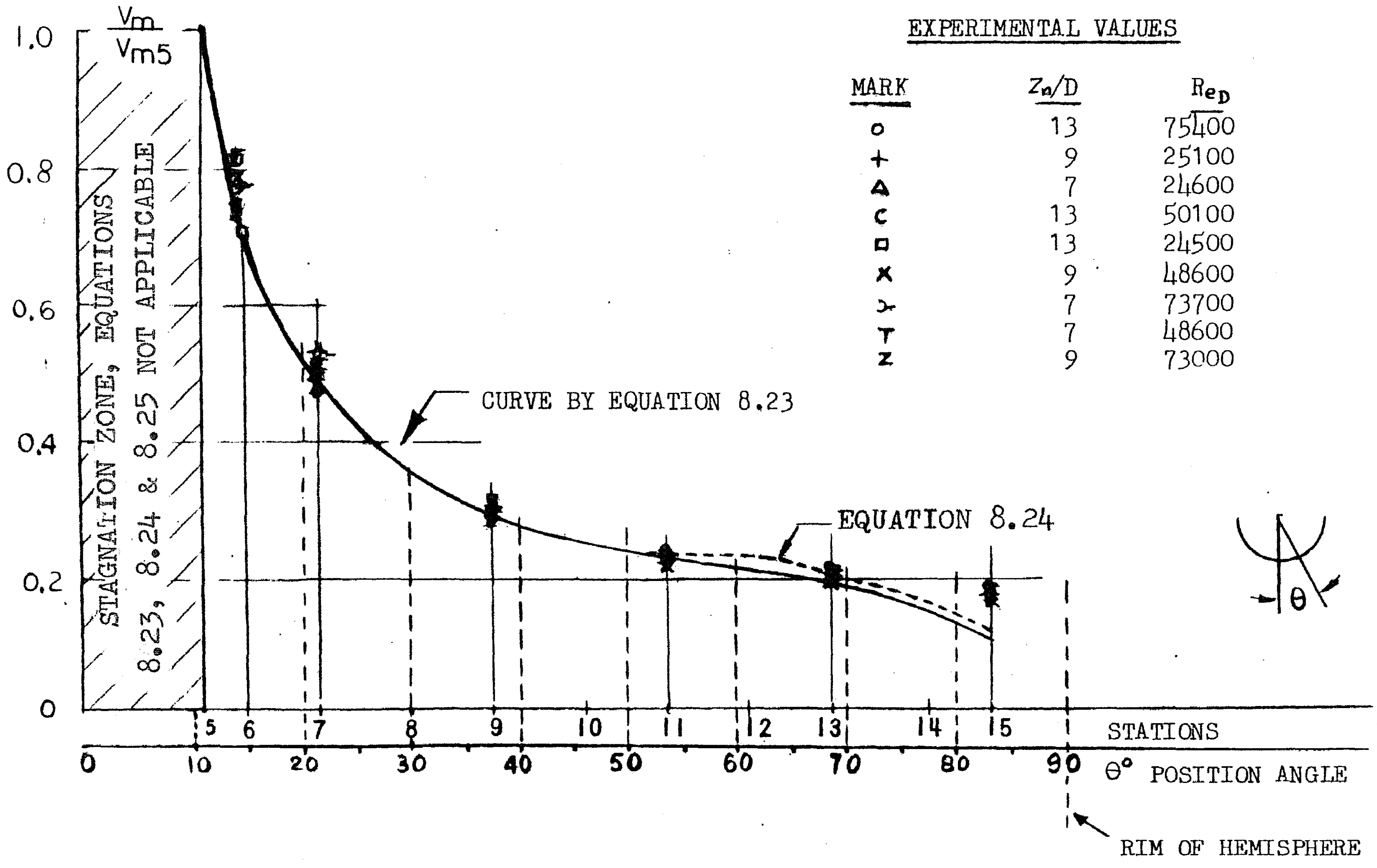

EXPERIMENTAL VALUES

MARK	Z_n/D	R_{e_D}
o	13	75400
+	9	25100
△	7	24600
c	13	50100
□	13	24500
×	9	48600
⅄	7	73700
T	7	48600
z	9	73000

FIG. 36 MAXIMUM VELOCITY DECAY IN THE WALL JET

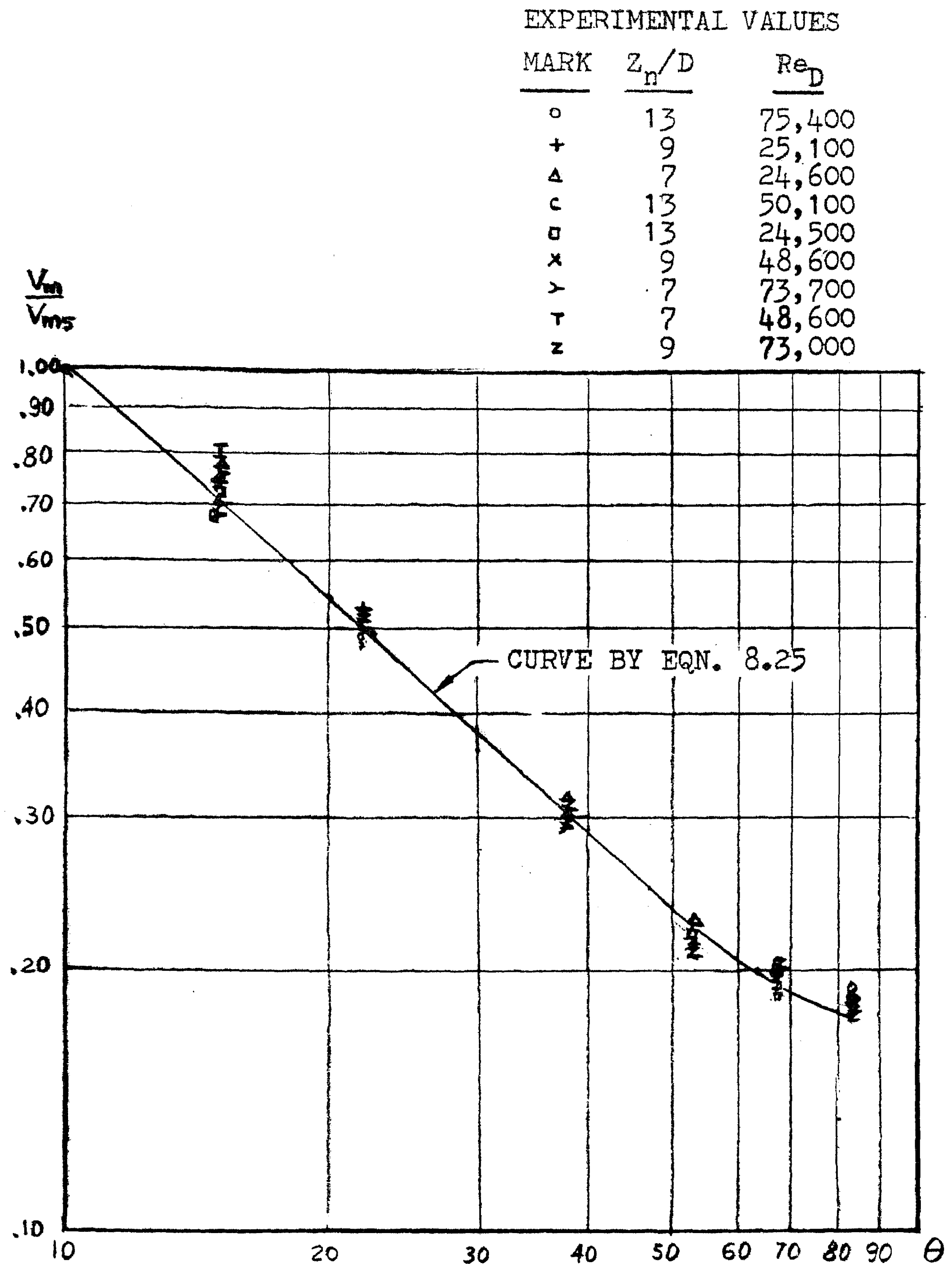

EXPERIMENTAL VALUES

MARK	Z_n/D	Re_D
○	13	75,400
+	9	25,100
Δ	7	24,600
c	13	50,100
□	13	24,500
×	9	48,600
≻	7	73,700
T	7	48,600
z	9	73,000

FIG. 36a MAXIMUM VELOCITY DECAY WITH CURVE BY EQN. 8.25

REDUCTION FORMULA FOR FIG.36:

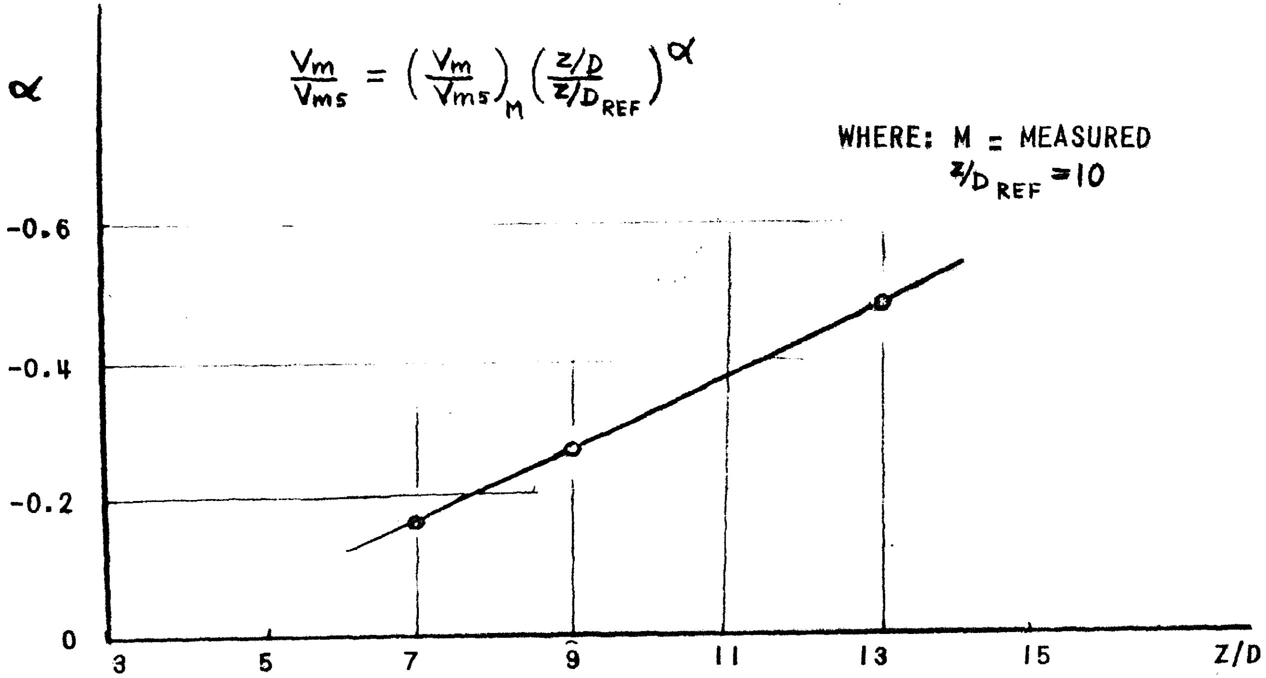

$$\frac{V_m}{V_{ms}} = \left(\frac{V_m}{V_{ms}}\right)_M \left(\frac{Z/D}{Z/D_{REF}}\right)^{\alpha}$$

WHERE: M = MEASURED
$Z/D_{REF} = 10$

FIG. 36b MAXIMUM VELOCITY DECAY EXPONENT PLOT

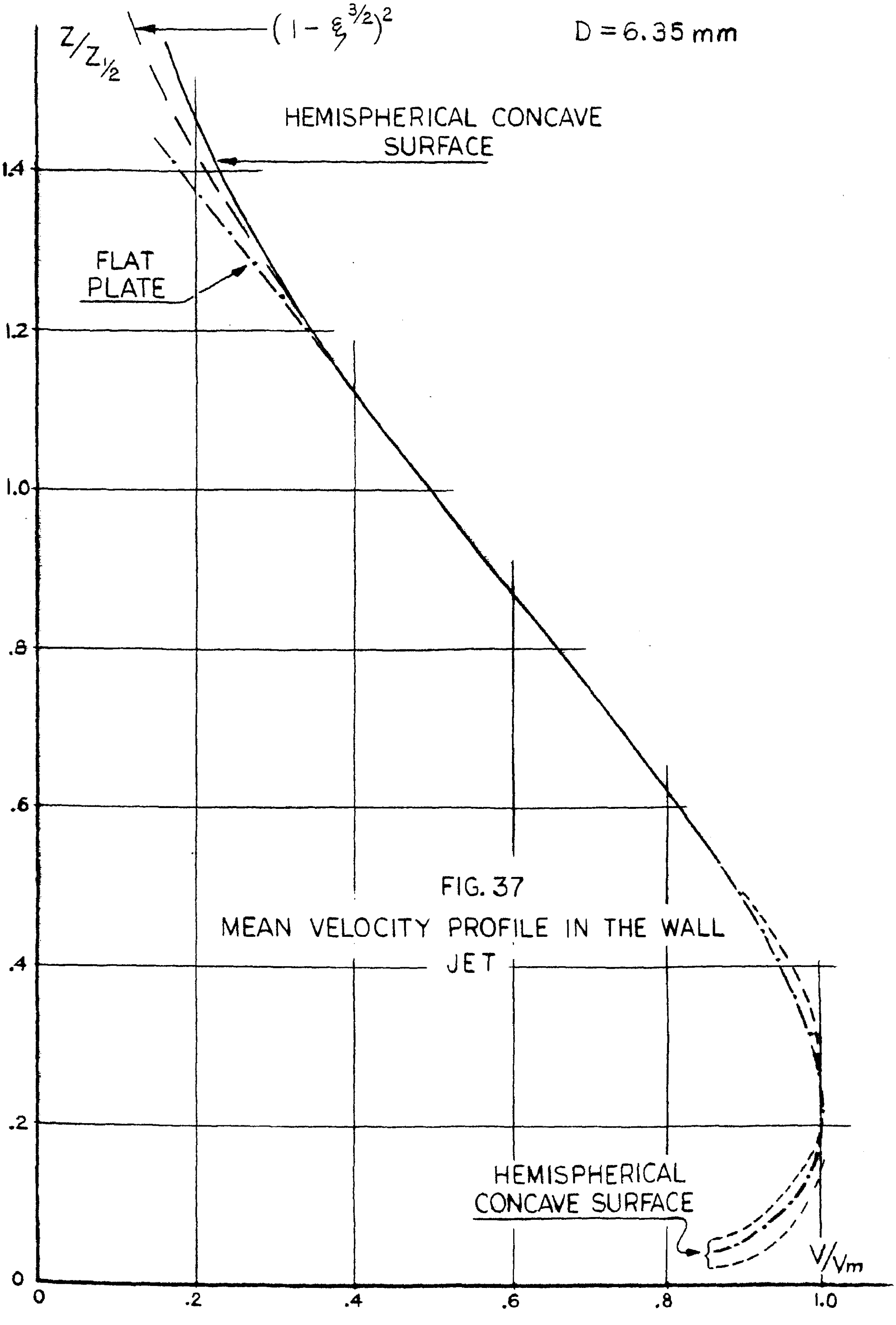

FIG. 37

MEAN VELOCITY PROFILE IN THE WALL JET

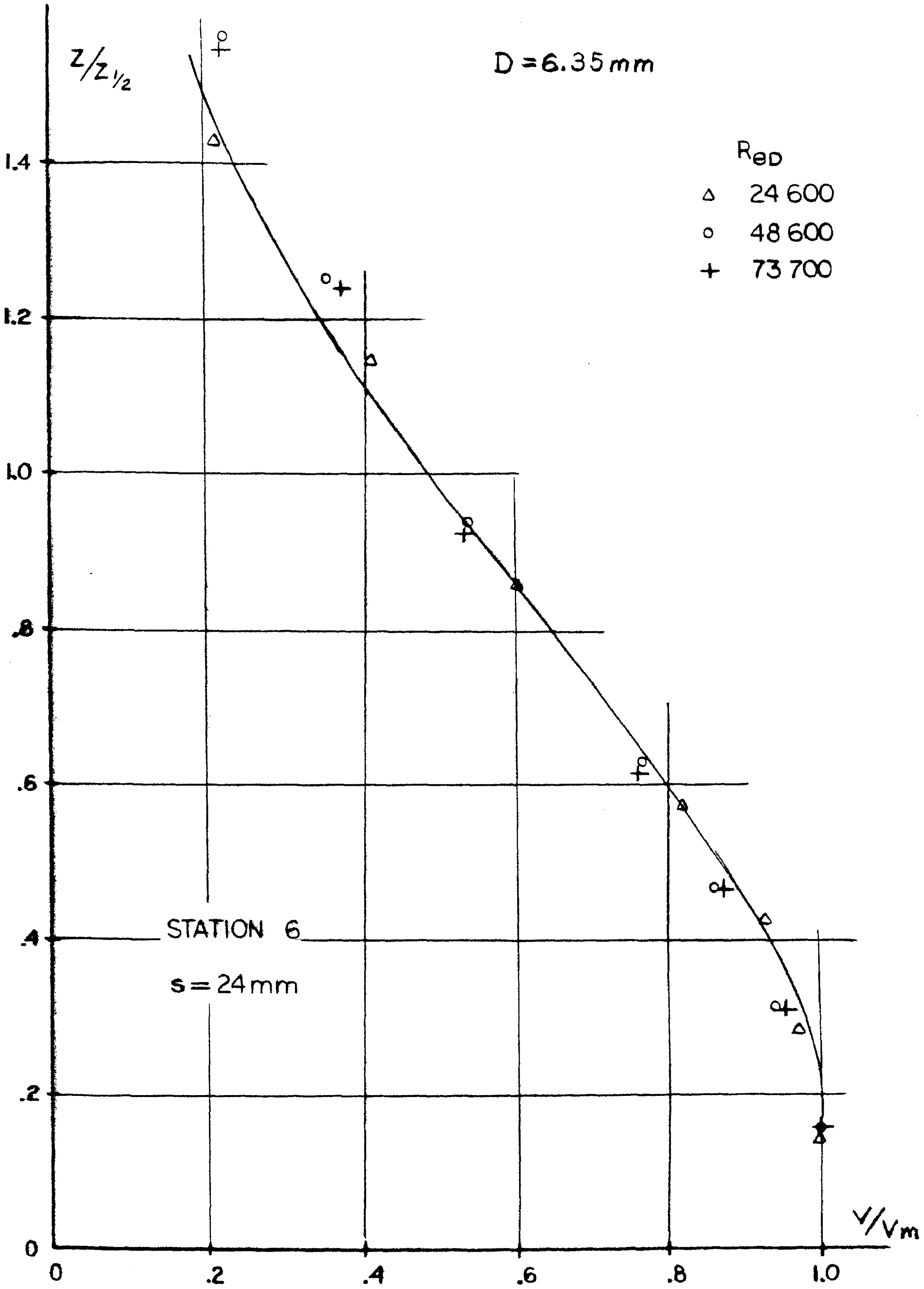

WALL JET VELOCITY PROFILE AT STATION 6, $Z_n/D=7$

FIG. 37a

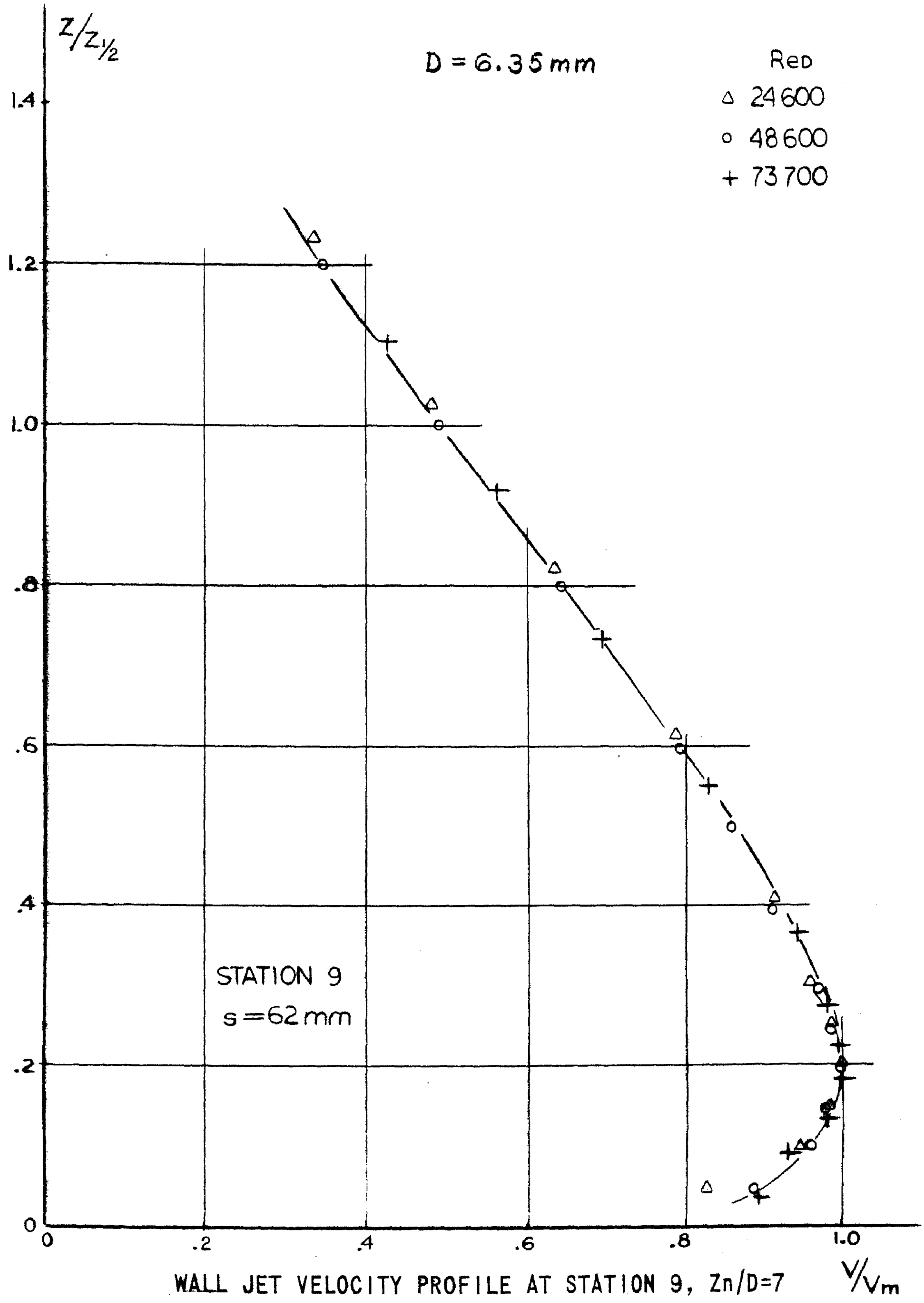

WALL JET VELOCITY PROFILE AT STATION 9, Zn/D=7

FIG. 37b

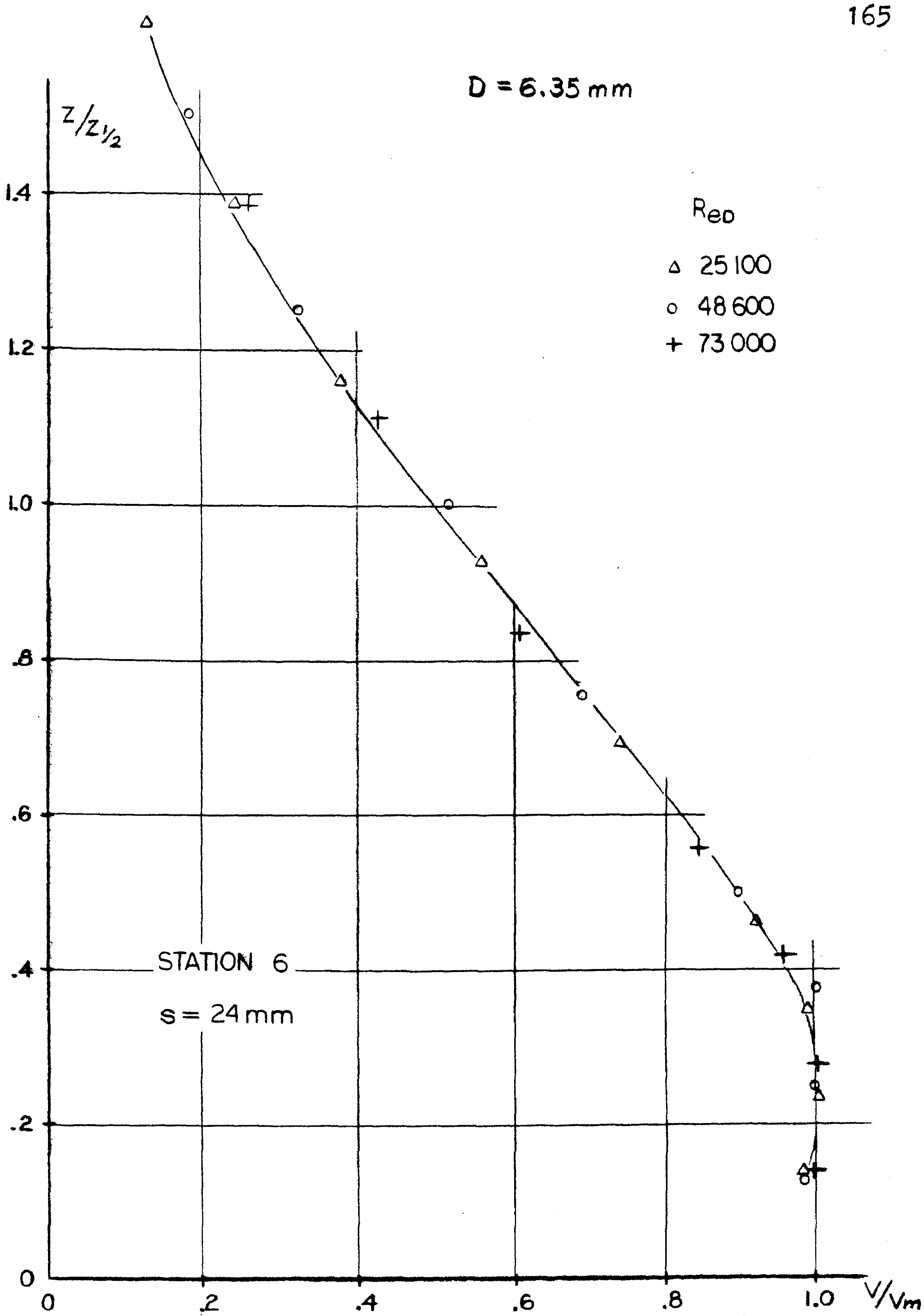

WALL JET VELOCITY PROFILE AT STATION 6, Zn/D=9

FIG. 37c

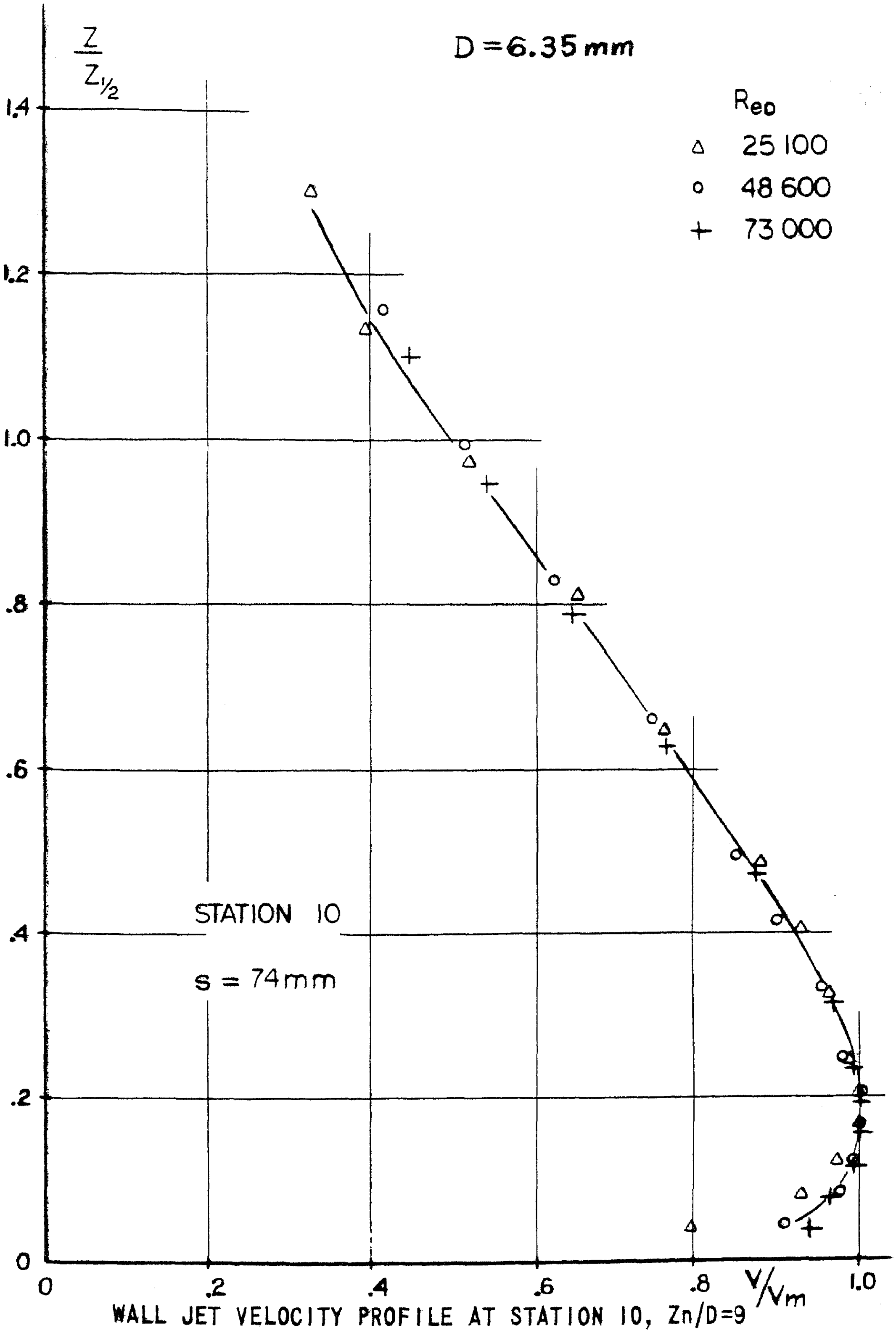

WALL JET VELOCITY PROFILE AT STATION 10, Zn/D=9
FIG. 37d

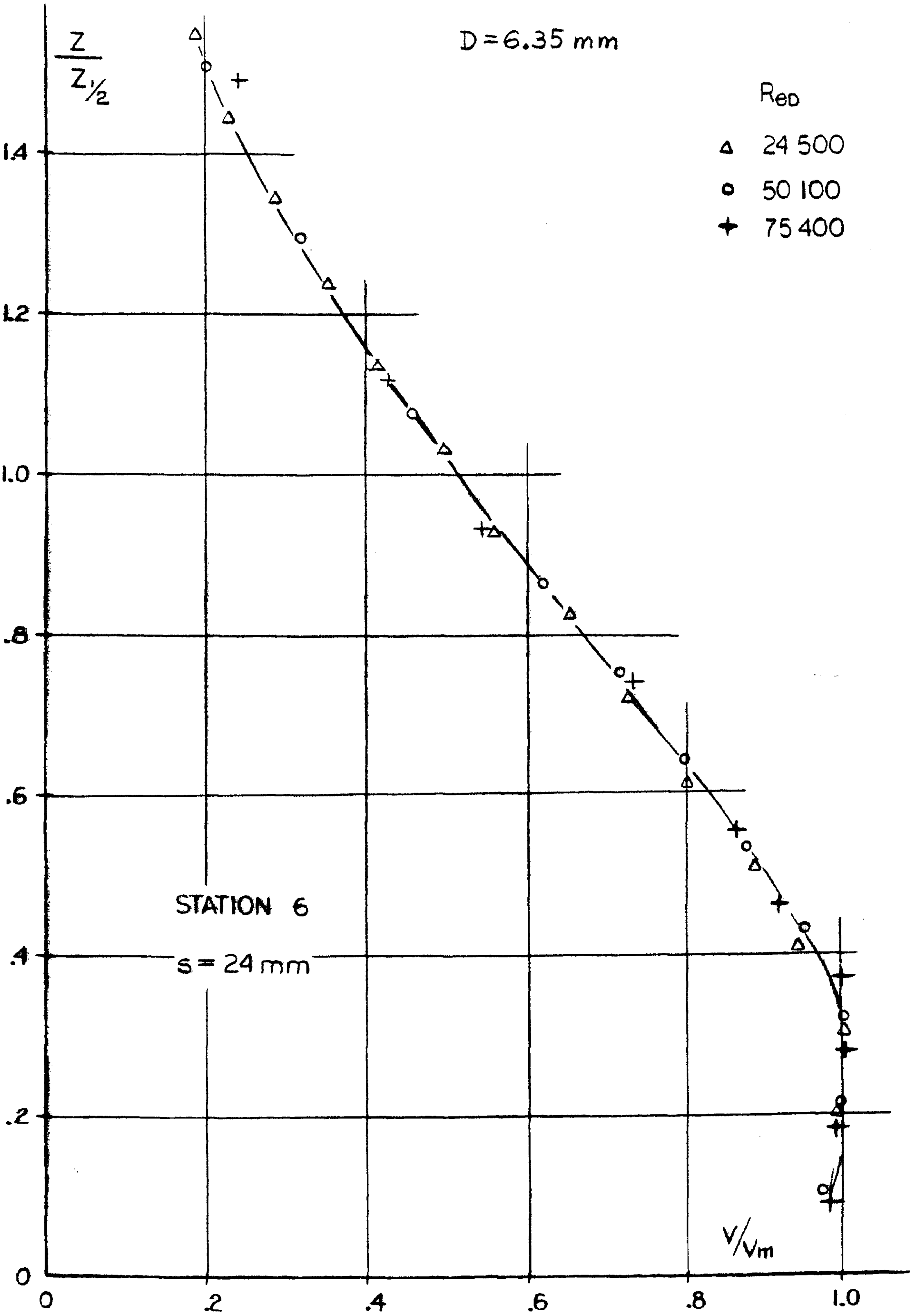

WALL JET VELOCITY PROFILE AT STATION 6, Zn/D=13

FIG. 37e

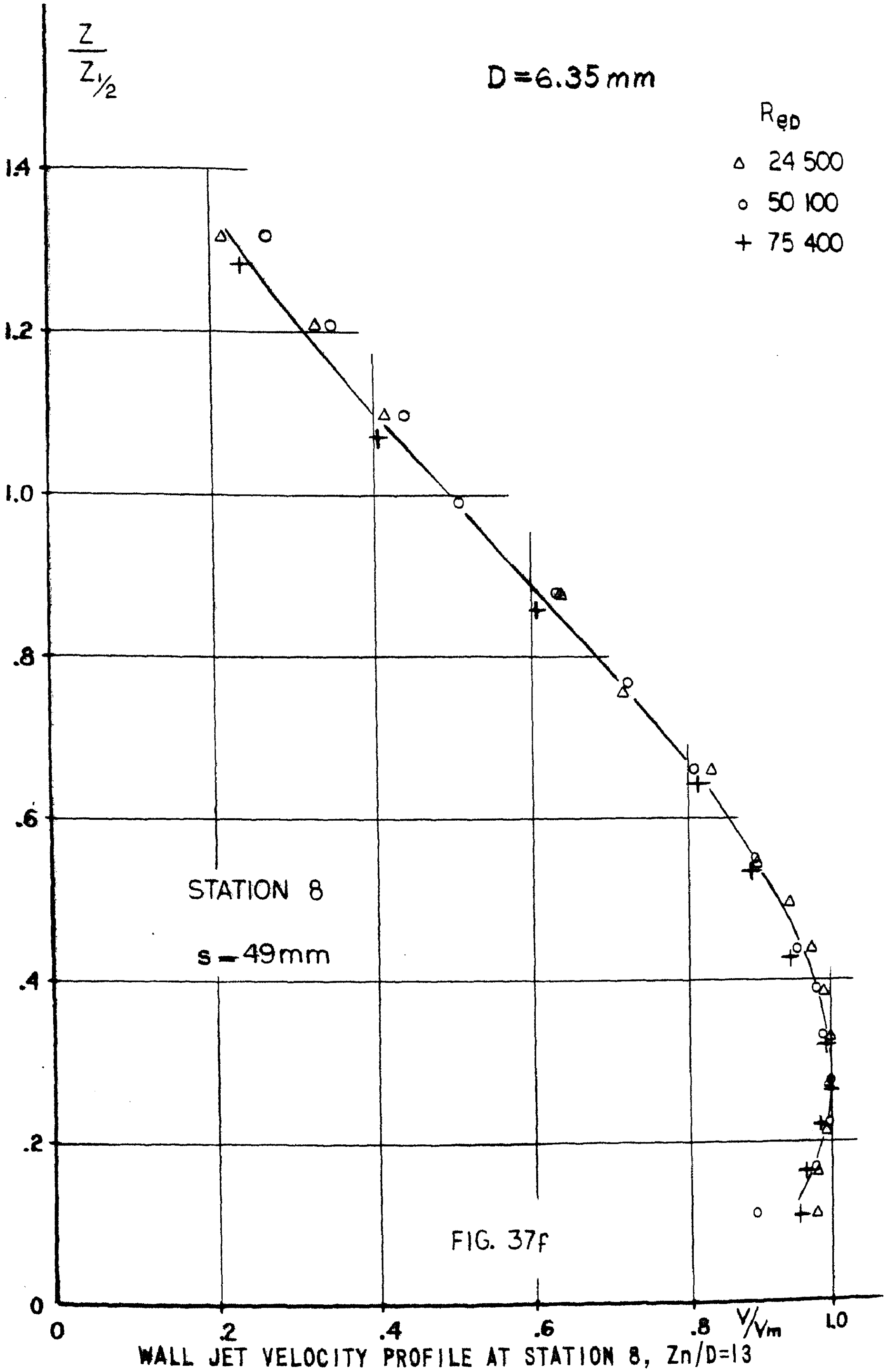

WALL JET VELOCITY PROFILE AT STATION 8, Zn/D=13
FIG. 37f

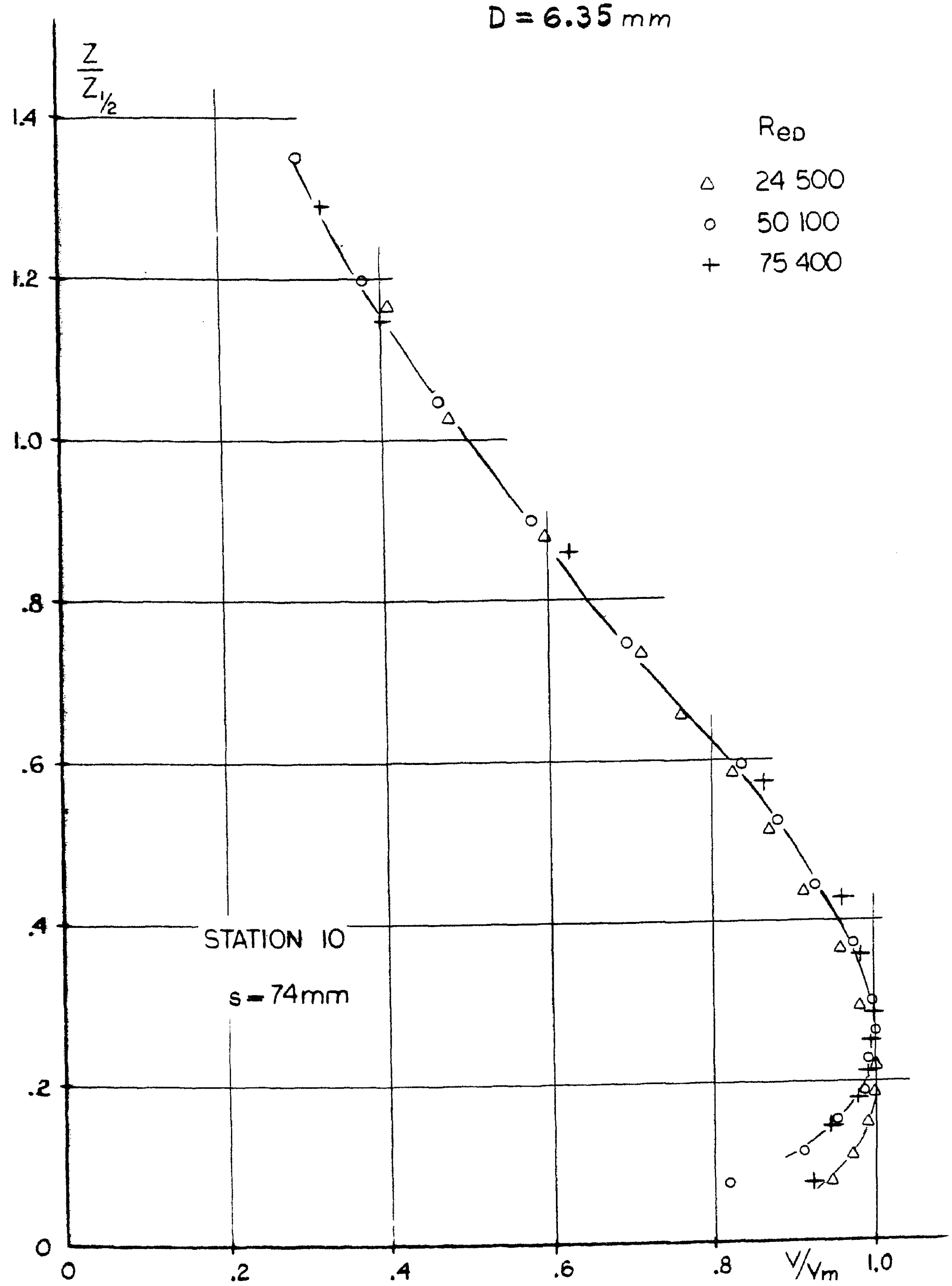

WALL JET VELOCITY PROFILE AT STATION 10, Zn/D=13

FIG. 37g

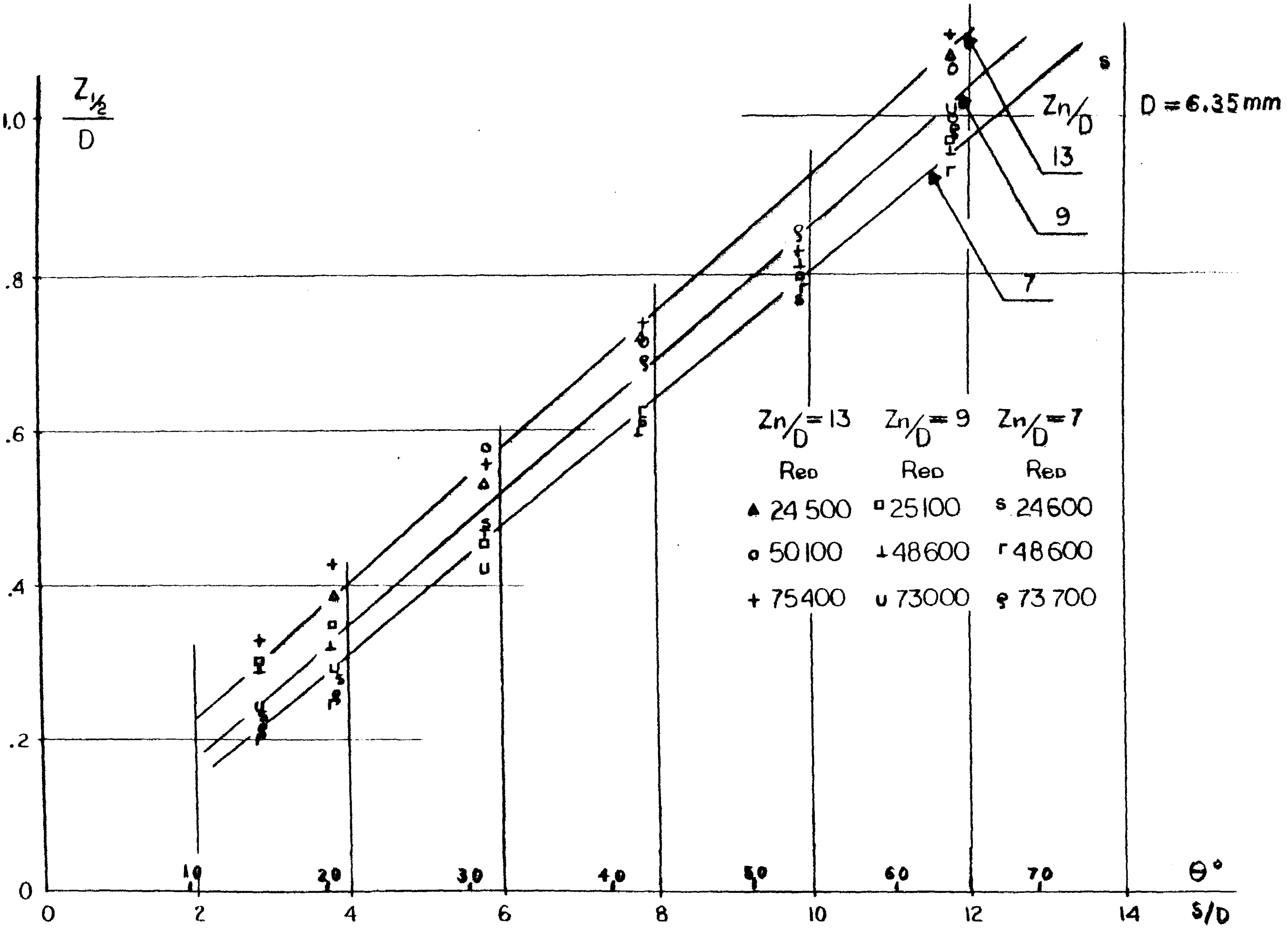

FIG. 38 SPREAD OF THE WALL JET

VITA

Stefan Jachna was born in . He holds B.S. and M.S. degrees in Mechanical Engineering from Polytechnical Institute of Gdansk, Poland, and M.S. in Mechanical Engineering from Stevens Institute of Technology, Hoboken, New Jersey.

He has professional experience in forging, machining, flow machinery testing, centrifugal pump design, plant engineering, mechanical equipment specification writing and bid evaluation.

The research, on which the dissertation is based, was conducted from 1971 to 1976 and includes over four hundred pages of test logs and plots.